

Prostate Segmentation and Regions of Interest Detection in Transrectal Ultrasound Images

by

Joseph Gaber Elias Awad

A thesis
presented to the University of Waterloo
in fulfillment of the
thesis requirement for the degree of
Doctor of Philosophy
in
Electrical and Computer Engineering

Waterloo, Ontario, Canada, 2007

©Joseph Gaber Elias Awad, 2007

I hereby declare that I am the sole author of this thesis. This is a true copy of the thesis, including any required final revisions, as accepted by my examiners.

I understand that my thesis may be made electronically available to the public.

Abstract

The early detection of prostate cancer plays a significant role in the success of treatment and outcome. To detect prostate cancer, imaging modalities such as TransRectal Ultra-Sound (TRUS) and Magnetic Resonance Imaging (MRI) are relied on. MRI images are more comprehensible than TRUS images which are corrupted by noise such as speckles and shadowing. However, MRI screening is costly, often unavailable in many community hospitals, time consuming, and requires more patient preparation time. Therefore, TRUS is more popular for screening and biopsy guidance for prostate cancer. For these reasons, TRUS images are chosen in this research. Radiologists first segment the prostate image from ultrasound image and then identify the hypoechoic regions which are more likely to exhibit cancer and should be considered for biopsy. In this thesis, the focus is on prostate segmentation and on Regions of Interest (ROI) segmentation.

First, the extraneous tissues surrounding the prostate gland are eliminated. Consequently, the process of detecting the cancerous regions is focused on the prostate gland only. Thus, the diagnosing process is significantly shortened. Also, segmentation techniques such as thresholding, region growing, classification, clustering, Markov random field models, artificial neural networks (ANNs), atlas-guided, and deformable models are investigated. In this dissertation, the deformable model technique is selected because it is capable of segmenting difficult images such as ultrasound images. Deformable models are classified as either parametric or geometric deformable models. For the prostate segmentation, one of the parametric deformable models, Gradient Vector Flow (GVF) deformable contour, is adopted because it is capable of segmenting the prostate gland, even if the initial contour is not close to the prostate boundary. The manual segmentation of ultrasound images not only consumes much time and effort, but also leads to operator-dependent results. Therefore, a fully automatic prostate segmentation algorithm is proposed based on knowledge-based rules. The new algorithm results are evaluated with respect to their manual outlining by using distance-based and area-based metrics. Also, the novel technique is compared with two well-known semi-automatic algorithms to illustrate its superiority. With hypothesis testing, the proposed algorithm is statistically superior to the other two algorithms. The newly developed algorithm is operator-independent and capable of accurately segmenting a prostate gland with any shape and orientation from the ultrasound

image.

The focus of the second part of the research is to locate the regions which are more prone to cancer. Although the parametric dynamic contour technique can readily segment a single region, it is not conducive for segmenting multiple regions, as required in the regions of interest (ROI) segmentation part. Since the number of regions is not known beforehand, the problem is stated as 3D one by using level set approach to handle the topology changes such as splitting and merging the contours. For the proposed ROI segmentation algorithm, one of the geometric deformable models, active contours without edges, is used. This technique is capable of segmenting the regions with either weak edges, or even, no edges at all. The results of the proposed ROI segmentation algorithm are compared with those of the two experts' manual marking. The results are also compared with the common regions manually marked by both experts and with the total regions marked by either expert. The proposed ROI segmentation algorithm is also evaluated by using region-based and pixel-based strategies. The evaluation results indicate that the proposed algorithm produces similar results to those of the experts' manual markings, but with the added advantages of being fast and reliable. This novel algorithm also detects some regions that have been missed by one expert but confirmed by the other.

In conclusion, the two newly devised algorithms can assist experts in segmenting the prostate image and detecting the suspicious abnormal regions that should be considered for biopsy. This leads to the reduction the number of biopsies, early detection of the diseased regions, proper management, and possible reduction of death related to prostate cancer.

Acknowledgements

O LORD our Lord, how excellent is thy name in all the earth! who hast set thy glory above the heavens. (Psa 8:1) The LORD is my strength and my shield; my heart trusted in him, and I am helped: therefore my heart greatly rejoiceth; and with my song will I praise him. (Psa 28:7)

I would like to express my sincere gratitude to my supervisors, Professor Magdy Salama and Professor Kamilia Rizkalla for all their patience, invaluable guidance, support, and encouragement throughout this research.

I would like also to thank Professors Mohamed Kamel, Hamid Tizhoosh, George Freeman, Catherine Gebotys, Aaron Fenster, Donal Downey, Nasr Hana, and Otman Basir. It was through their advices and helpful comments that this work has been accomplished.

I am also very grateful to the graduate office staff for all their kind help throughout my graduate studies.

I would like also to express my deep gratitude to my parents, wife, and all family members for their magnificent and continuous support. A special thanks to my son and my daughter who fill my life with joy.

I would like to dedicate this work to all of my family who have supported me throughout my life.

Contents

Abstract	iii
Acknowledgements	v
Contents	vi
List of Tables	xi
List of Figures	xii
1 Introduction	1
1.1 Introduction	1
1.2 Motivation	3
1.3 Objectives	3
1.4 Proposed Algorithm	4
1.5 Outline of the Thesis	9
2 Prostate Cancer	11
2.1 Introduction	11
2.2 Prostate Anatomy	12
2.3 Pathology	14
2.3.1 Development of BPH	14
2.3.2 Cancer Classification	14
2.4 Histological Grading of Prostate Cancer	14

2.5	Early Detection	15
2.6	Prostate Cancer Progress	17
2.7	Prostate Cancer Staging	19
2.8	Summary	20
3	Image Segmentation	23
3.1	Introduction	23
3.2	Background	23
3.2.1	Definition	23
3.2.2	Interaction	24
3.2.3	Validation	24
3.3	Segmentation Techniques	24
3.3.1	Thresholding	25
3.3.2	Region Growing	28
3.3.3	Classification	30
3.3.4	Clustering	31
3.3.4.1	The K-Means or ISODATA Algorithm	31
3.3.4.2	The Fuzzy C-Means Algorithm	33
3.3.4.3	The Expectation-Maximization (EM) Algorithm	34
3.3.5	Markov Random Field Models	35
3.3.6	Artificial Neural Networks (ANNs)	35
3.3.7	Deformable Models	35
3.3.7.1	Parametric Deformable Models	36
3.3.7.2	Geometric Deformable Models	39
3.3.8	Atlas-Guided Technique	44
3.3.9	Other Techniques	44
3.4	Summary	45
4	Prostate Segmentation	47
4.1	Introduction	47
4.2	Related Work	48
4.2.1	Semiautomatic Prostate Segmentation	48

4.2.2	Automatic Prostate Segmentation	50
4.2.3	Analysis of the Existing Algorithms and Research Goals	51
4.3	Algorithm Description	53
4.3.1	Building the Knowledge-Based Rules	55
4.3.2	Enhancing the Image	56
4.3.2.1	Sequential Sticks Technique	56
4.3.2.2	Gaussian Filter	60
4.3.3	Generating the Seed Point	60
4.3.4	Detecting the Prostate Edge	61
4.3.4.1	Applying Canny edge detection	61
4.3.4.2	Eliminating the False Edges	61
4.3.4.3	Initial Boundary Detection by Radial Scanning	62
4.3.4.4	Gradient Vector Flow (GVF) Deformable Contour	62
4.3.4.5	Find the Outer Boundary of the Prostate	63
4.3.5	Extracting the Prostate Image	63
4.3.5.1	Extracting the Prostate Image	63
4.3.5.2	Cropping the Image	64
4.4	Results	64
4.4.1	Initial Contour	64
4.4.2	Final Contour	69
4.5	Evaluation of Prostate Segmentation Algorithm	73
4.5.1	Distance-Based Metrics	73
4.5.2	Area-Based Metrics	75
4.5.3	Testing the Results of the Proposed Algorithm	76
4.6	Summary	78
5	Regions of Interest Segmentation	81
5.1	Introduction	81
5.2	Related Work	81
5.3	Goals of the ROI Segmentation Algorithm	83
5.4	Algorithm Description	84
5.4.1	Building the ROI Knowledge-Based Rules	86

5.4.2	Enhancing the Image	86
5.4.3	Finding the Hypoechoic Regions	86
5.4.3.1	The Initial Contour	87
5.4.3.2	Dynamic Contours Deformation	89
5.4.3.3	Hypoechoic Regions Marking	93
5.4.4	Eliminating the Regions which are not Likely to Exhibit Cancer . .	93
5.4.5	Extracting the ROI	94
5.5	Results	94
5.6	Evaluation	102
5.6.1	Region Evaluation	105
5.6.1.1	Considering the Extra Regions as the FP Regions	110
5.6.1.2	Considering the Extra Regions as the TP Regions	111
5.6.2	Pixel Evaluation	113
5.7	Summary	118
6	Conclusions and Contributions	121
6.1	Conclusions	121
6.2	Contributions	124
6.3	Future Work	126
A	Ultrasound Characteristics	129
A.1	Introduction	129
A.2	Fundamentals of Ultrasound	130
A.2.1	Attenuation of Ultrasound	130
A.2.1.1	Divergence	131
A.2.1.2	Reflection	132
A.2.1.3	Scattering	132
A.2.1.4	Absorption	132
A.2.1.5	Refraction	132
A.2.2	Doppler Effect	133
A.3	Diagnostic Ultrasonic Imaging	133
A.3.1	Transducers	134

A.3.2	A-Mode and B-Mode	135
A.3.3	M-Mode and C-Mode imaging	136
A.3.4	Doppler Methods for Flow Measurement	136
A.3.5	Colour Doppler Flow Imaging	137
A.4	Summary	138
B	One Tailed Hypothesis Testing	139
C	ROI Algorithm Results	143
	Bibliography	153

List of Tables

2.1	Tumour node metastasis staging [2, 7]	19
4.1	Comparison between the proposed algorithm and two other algorithms . .	77
4.2	Hypotheses testing for <i>MAD</i> and <i>MAXD</i> errors	78
4.3	Hypotheses testing for sensitivity and accuracy	78
5.1	Area weighting factor ν	95
5.2	Evaluation table [3]	103
5.3	Number of marked regions	109
5.4	Region evaluation of the first expert (first case)	110
5.5	Region evaluation of the second expert (first case)	110
5.6	Region evaluation of the proposed algorithm (first case)	111
5.7	Region evaluation of the first expert (second case)	112
5.8	Region evaluation of the second expert (second case)	112
5.9	Region evaluation of the proposed algorithm (second case)	113
5.10	Summary of the region evaluation results of both cases	113
5.11	Evaluation using accuracy measure (all values are a percentage)	115
5.12	Evaluation using sensitivity measure (all values are a percentage)	116
5.13	Evaluation using specificity measure (all values are a percentage)	117
5.14	Pixels evaluation summary	118

List of Figures

1.1	Diagnosing scheme for prostate cancer	2
1.2	Transrectal ultrasound image	3
1.3	Prostate image	4
1.4	Suspicious hypoechoic regions	4
1.5	Research overview	5
1.6	Image segmentation chapter overview	6
1.7	Prostate segmentation chapter overview	7
1.8	Regions of interest segmentation chapter overview	8
2.1	Trends in prostate cancer survival	11
2.2	Anatomy section shows prostate, bladder and kidneys [2]	12
2.3	Location of the prostate gland [2]	13
2.4	Anatomical zones of the prostate [2]	13
2.5	Gleason grading [7]	15
2.6	Transrectal ultrasound image	17
2.7	Intraprostatic spread [2]	17
2.8	Seminal vesicle spread [2]	18
2.9	Extracapsular spread [2]	18
2.10	Lymph nodal spread [2]	18
3.1	Histogram showing three apparent classes, using two thresholds T_1 and T_2 .	26
3.2	Thresholding techniques	27
3.3	Example of region growing	29

3.4	2D feature space	30
3.5	Superiority of GVF over the conventional deformable contour	39
3.6	Possible locations of the contour relative to the object [61]	42
3.7	Level set representation	43
4.1	Prostate segmentation flow chart	54
4.2	Different sticks five pixels in length	57
4.3	Effect of changing stick length	58
4.4	Comparison between fixed and sequential sticks	59
4.5	Initial contour results	66
4.6	Initial contour results	67
4.7	Initial contour results	68
4.8	Proposed automatic segmentation versus manual segmentation	70
4.9	Proposed automatic segmentation versus manual segmentation	71
4.10	Proposed automatic segmentation versus manual segmentation	72
4.11	Manual (solid) and automatic (dotted) segmentation	74
4.12	Radial difference between the proposed algorithm and the manual contour	75
4.13	Area-based metrics	76
5.1	Regions segmentation using graph theory [140]	82
5.2	Proposed regions of interest segmentation flow chart	85
5.3	Initial level set function ϕ_o	88
5.4	Zero-level contour (initial contour C_o)	88
5.5	$H_\varepsilon(z)$ versus $H(z)$	90
5.6	Stopping criterion	93
5.7	Level set deformation	96
5.8	ROI results	98
5.9	ROI results	99
5.10	ROI results	100
5.11	ROI results	101
5.12	Proposed ROI algorithm results versus manual marking	104
5.13	Regions counting block diagram	107

5.14	Percentage intersection block diagram	108
A.1	Sinusoidal acoustic wave propagation	131
A.2	Reflection and refraction of ultrasonic waves	132
A.3	Measuring blood flow velocity by ultrasound	133
A.4	(a) A-mode (b) B-mode	134
A.5	Construction of a single-element ultrasonic transducer	135
A.6	Block diagram of an A-mode instrument	135
A.7	Block diagram of a B-mode ultrasonic imaging system	136
A.8	Block diagram of a CW Doppler flow metre	137
A.9	The block diagram of a pulsed Doppler system	137
B.1	<i>t</i> statistic test	141
C.1	Proposed ROI algorithm results versus manual marking	144
C.2	Proposed ROI algorithm results versus manual marking	145
C.3	Proposed ROI algorithm results versus manual marking	146
C.4	Proposed ROI algorithm results versus manual marking	147
C.5	Proposed ROI algorithm results versus manual marking	148
C.6	Proposed ROI algorithm results versus manual marking	149
C.7	Proposed ROI algorithm results versus manual marking	150
C.8	Proposed ROI algorithm results versus manual marking	151

Chapter 1

Introduction

1.1 Introduction

The prostate gland is a part of the male reproductive system and is located just below the bladder. Prostate cancer is a very serious disease that is one of the leading causes of cancerous death in men. According to the National Cancer Institute of Canada (NCIC), prostate adenocarcinoma is the most common disease in middle-aged and elderly men all over the world [1–4]:

- Approximately 20,700 Canadian men were diagnosed with prostate cancer in 2006, and around 20% of them have died as a result of prostate cancer.
- Each week, 398 Canadian men are diagnosed with prostate cancer, and about 81 of them die.
- One of every seven men develops prostate cancer during his lifetime after the age of 60. One every 26 dies of prostate cancer.

The early detection of prostate cancer is pivotal to the success of the treatment. Ultrasound B-mode is the standard means for imaging the prostate [5]. The most common screening modalities for the early detection of prostate cancer are Digital Rectal Examination (DRE), Prostate Specific Antigen (PSA), and TransRectal UltraSound (TRUS). Their

details are discussed in chapter 2. The DRE test is carried out by a skilled physician who manually feels for any abnormalities in the prostate gland through the rectum. The accuracy of this examination is not high. Nevertheless, DRE is inexpensive, easy to perform, and can detect most of the tumours of a sufficient volume. PSA is a reliable test for the early detection of prostate cancer. PSA is an enzyme which is secreted by the prostatic cells. High PSA values suggest problems with the prostate gland. Then TRUS is used to display the prostate gland for a radiologist to diagnose. If any of the previous screening modalities suggest any abnormalities, biopsies should be conducted, and then examined by a pathologist. The chart in Figure 1.1 displays the diagnostic scheme for prostate cancer.

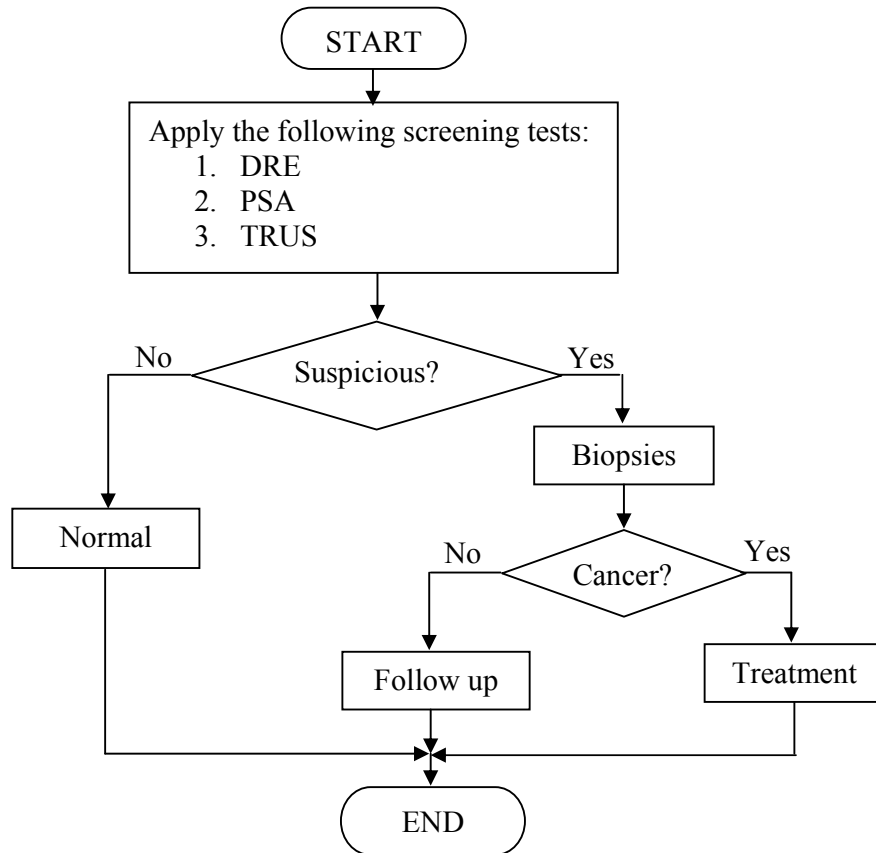


Figure 1.1: Diagnosing scheme for prostate cancer

1.2 Motivation

If prostate cancer is suspected, biopsies are conducted of the prostate gland. Transrectal ultrasound (TRUS) is used to guide the procedure. The sextant approach is the most common biopsy technique for diagnosing prostate cancer. In this technique, six biopsies are taken from the prostate gland, three biopsies from each side, left and right sides, obtained from the apex, centre, and base areas. Eskew et al. [6] have shown that increasing the number of biopsies from six to thirteen increases the prostate cancer detection rate by 35%. Since a biopsy is an invasive procedure, increasing the number of biopsies to cover all the prostate gland is not the best solution. It is advantageous to develop a diagnostic tool for detecting the suspicious regions of the prostate gland and precisely guide the biopsy needles into these regions. Consequently, the detection rate of the prostate cancer is increased, and the number of biopsies is decreased. After all, avoiding unnecessary biopsies saves time, effort, and resources. Moreover, it is more convenient for the patient.

1.3 Objectives

The principal objective of this research is to implement a diagnostic tool for patients with possible prostate cancer by using transrectal ultrasound images as shown in Figure 1.2. The role of the radiologist is pivotal to the diagnostic procedure of prostate cancer. The radiologist first segments the prostate image, Figure 1.3, from the ultrasound image and then finds the hypoechoic regions, Figure 1.4, inside the prostate gland which are more likely to have prostate cancer and should be considered for biopsies. The proposed diagnostic tool can assist radiologists in segmenting the prostate image and identifying the suspicious regions which should be examined by conducting biopsies.

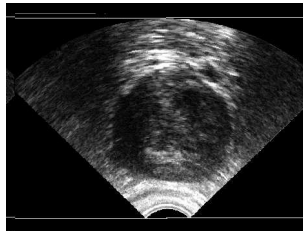


Figure 1.2: Transrectal ultrasound image

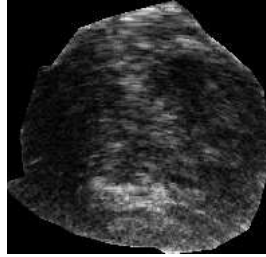


Figure 1.3: Prostate image



Figure 1.4: Suspicious hypoechoic regions

1.4 Proposed Algorithm

The radiologist's role in diagnosing prostate cancer seems straightforward. However, this manual analysis of TRUS images of the prostate is extremely time consuming. Considerable effort is required for the radiologist to repeat this tedious process for each frame of the 3D ultrasound image. Moreover, the results of this manual diagnosing are operator-dependent. As a result, a new algorithm is developed and implemented to automatically analyze the ultrasound images. The proposed diagnostic tool consists of two main parts. The first part is to, automatically, segment the prostate gland from the ultrasound images. The second part is to detect and segment the regions, which might be cancerous, for biopsies. An overview of the research is shown in Figure 1.5.

Since the interest is only in the cancer inside the prostate gland, the rest of the ultrasound image of the tissues surrounding the prostate gland is not required. Therefore, by removing the unnecessary information, the search for cancer is focused on a smaller area, the prostate area, of the ultrasound image. Not only is the diagnosing process speeded

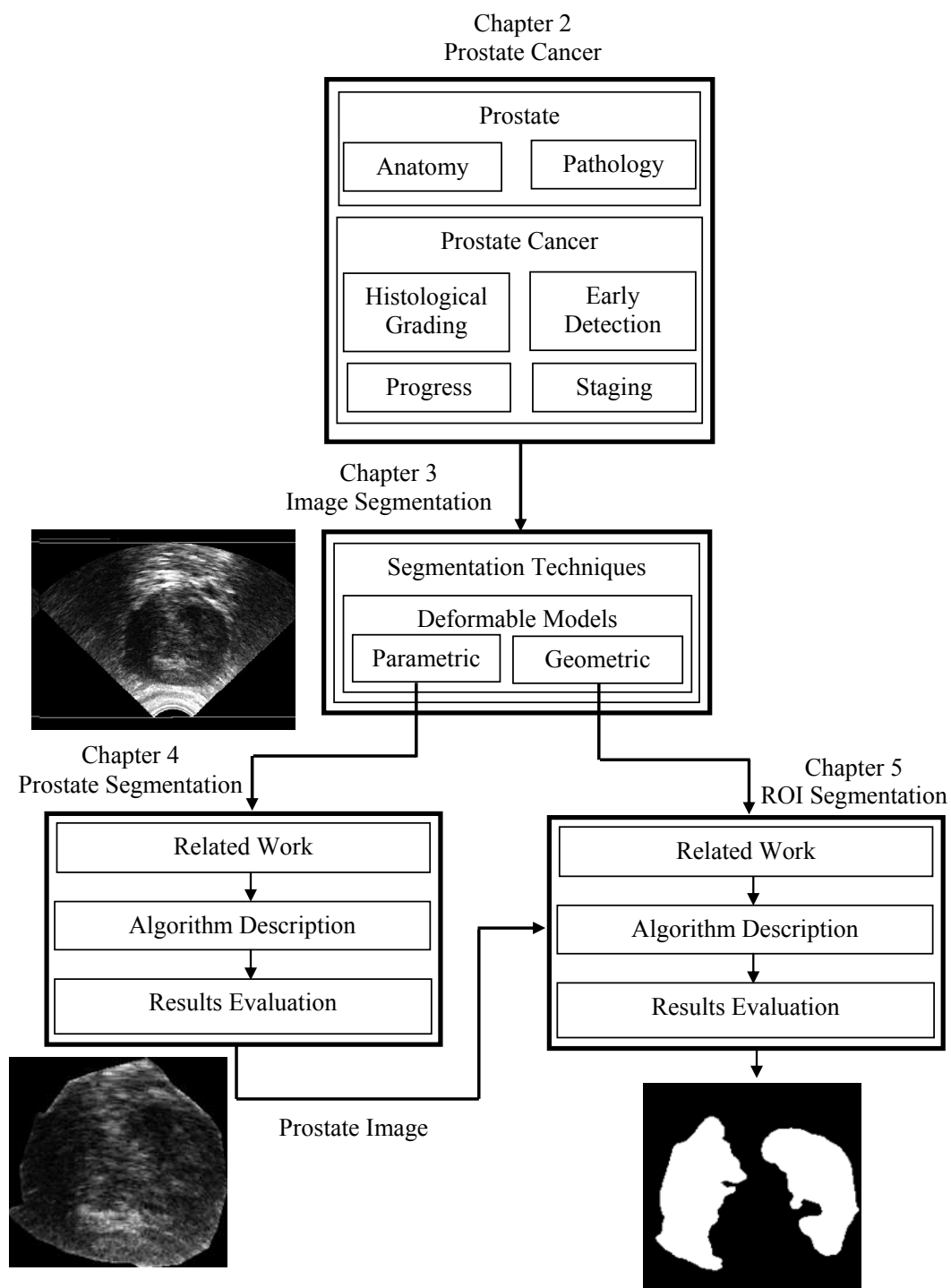


Figure 1.5: Research overview

up, but also memory storage is mitigated. The manual segmentation of the ultrasound images consumes much time and effort, and leads to operator-dependent results. Various segmentation techniques, including thresholding, region growing, classification, clustering, Markov random field models, artificial neural networks, atlas-guided, and deformable models as shown in Figure 1.6 are investigated. Many of these techniques are applied to the TRUS images. It is found that the parametric deformable model proves to be the most appropriate approach for the prostate segmentation part. One of the best techniques of the parametric deformable models is the Gradient Vector Flow (GVF) which is examined and incorporated in the proposed prostate segmentation algorithm.

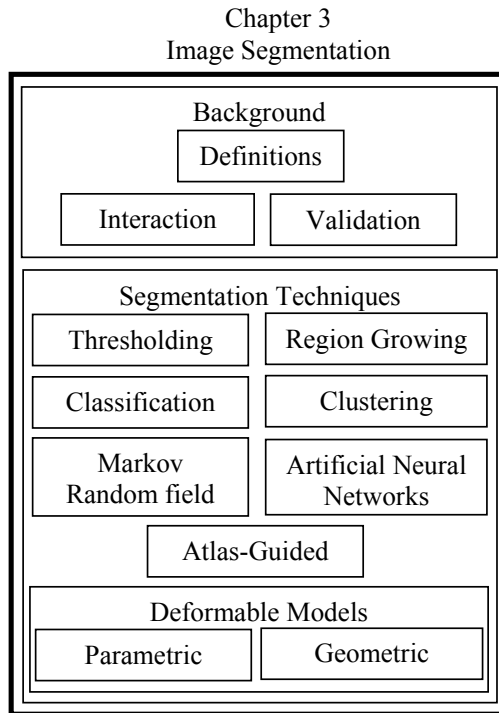


Figure 1.6: Image segmentation chapter overview

A fully automatic prostate segmentation algorithm is proposed, based on knowledge-based rules as shown in Figure 1.7. It is evaluated and compared with manual outlining by using distance-based and area-based metrics. Moreover, the proposed automated algorithm is compared with two well-known semi-automatic algorithms, and statically outperforms either algorithm during hypothesis testing. The novel algorithm is operator-independent

and is capable of accurately segmenting the prostate gland that has any shape and orientation from the ultrasound image. No time is wasted waiting for operator input, or manual editing or re-deforming. Moreover, the newly developed algorithm does not require any training data.

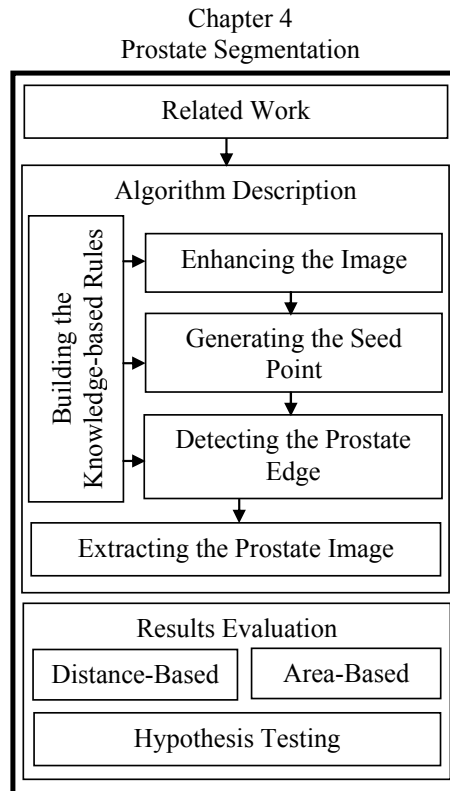


Figure 1.7: Prostate segmentation chapter overview

The second part of the research is to find the regions that are more likely to have a cancer and should be considered for biopsies. The parametric dynamic contour technique, which is used in the prostate segmentation part, can be adopted to segment a single region. However, this technique is too complicated to segment multiple regions, as required for Regions of Interest ROI Segmentation since the number of regions is not known. Consequently, transferring the ROI segmentation process into 3D by adopting the level set approach simplifies the problem because this approach is capable of handling the topology changes by splitting and merging the contours. Thus, the proposed ROI segmentation algorithm uses one of the geometric deformable model techniques, called *active contours*

without edges. This technique is very powerful for segmenting the regions with weak edges or no edges at all.

The proposed ROI segmentation algorithm is derived from knowledge-based rules as illustrated in Figure 1.8. The results of the algorithm proposed for the ROI segmentation are compared with the manual marking of two experts. In addition, the results are compared with the common regions marked by both experts and with the total regions marked by either expert. Region-based and pixel-based strategies are adopted to evaluate the proposed ROI algorithm. From the evaluation results, it is clear that the proposed ROI algorithm produces very similar results to those of the experts' manual marking. Furthermore, the proposed ROI algorithm detects some regions which are missed by one expert but confirmed by the other. Consequently, the proposed algorithms can assist the experts in finding the regions required to be considered for biopsy leading to early detection, proper management, and the decreased incidence of death related to prostate cancer.

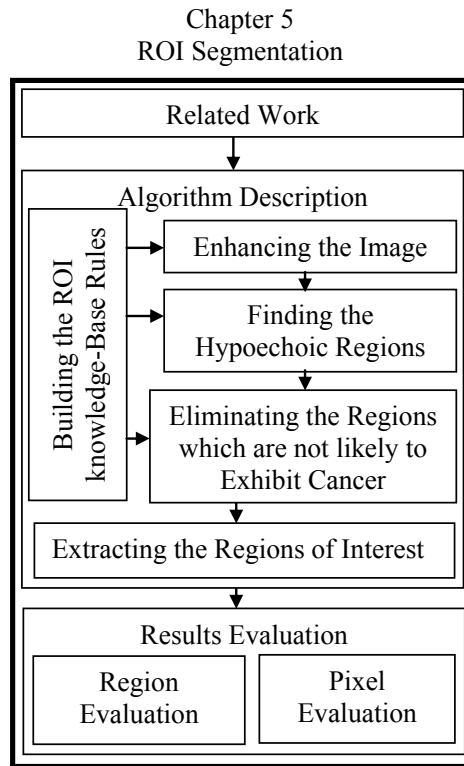


Figure 1.8: Regions of interest segmentation chapter overview

1.5 Outline of the Thesis

The goal of this research is to implement a diagnostic tool for patients with possible prostate cancer by using ultrasound images, leading to early detection, proper management, and a decreased incidence of death related to this disease. This thesis is divided into six chapters:

Following this chapter, Chapter 2 provides the background to adequately understand the anatomy of the prostate, prostate cancer, staging of the prostate cancer, and screening modalities.

Chapter 3 studies existing image segmentation techniques to investigate the most suitable approach for TRUS images. The techniques include thresholding, region growing, classification, clustering, Markov random field models, artificial neural networks, atlas-guided, and deformable models.

In Chapter 4 a fully automated prostate segmentation algorithm based on knowledge-based rules is proposed. The results are then evaluated with respect to manual outlining by using distance-based and area-based metrics, and compared with the results of two well-known semiautomatic algorithms. Also, it is proved, with a statistical confidence, that the proposed algorithm is better than any of the other two algorithms by conducting hypothesis testing.

The proposed ROI segmentation algorithm is presented in Chapter 5. This algorithm is developed to successfully segment and extract the regions which are more likely to have a cancer. The proposed algorithm results are compared with two experts' manual marking. Also, the results are compared with commonly marked regions of both experts, and the total regions marked by either expert. The proposed algorithm is evaluated using region-based and pixel-based strategies.

The conclusions, contributions, and suggestions for future work are presented in Chapter 6.

Chapter 2

Prostate Cancer

2.1 Introduction

Prostate cancer is one of the leading causes of death in men with cancer [1]. The probability of developing prostate cancer is about 14% of men, whereas the probability of death as a result of prostate cancer is about 4%. Recently, the public has become much more aware of prostate cancer, leading to efforts to improve early detection, and in turn, to increase the percentage of survivals annually, as denoted in Figure 2.1 [2].

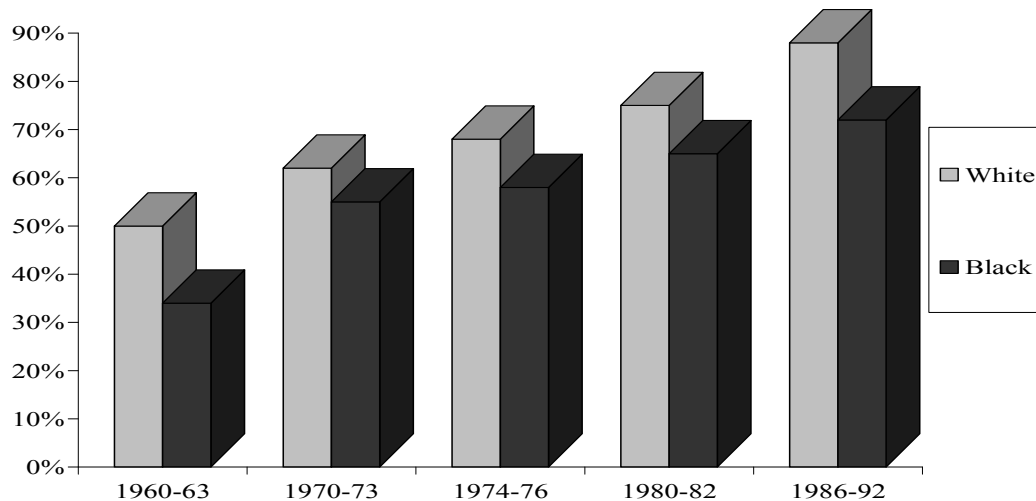


Figure 2.1: Trends in prostate cancer survival

2.2 Prostate Anatomy

The term *prostate* is derived from the Greek *prohistani* which means "to stand in front of". This expression was adopted by Herophilus of Alexandria in 335 B.C. to describe the organ located in front of the urinary bladder. Figure 2.2 is an anatomical view of the human body, including the prostate, kidneys, bladder, lymph nodes and ureters. The prostate's anatomy, physiology and pathology have been described in detail only within the last six decades. The prostate gland location is illustrated in Figure 2.3. The three major prostate diseases are Benign Prostatic Hyperplasia (BPH), carcinoma of prostate, and prostatitis [3].

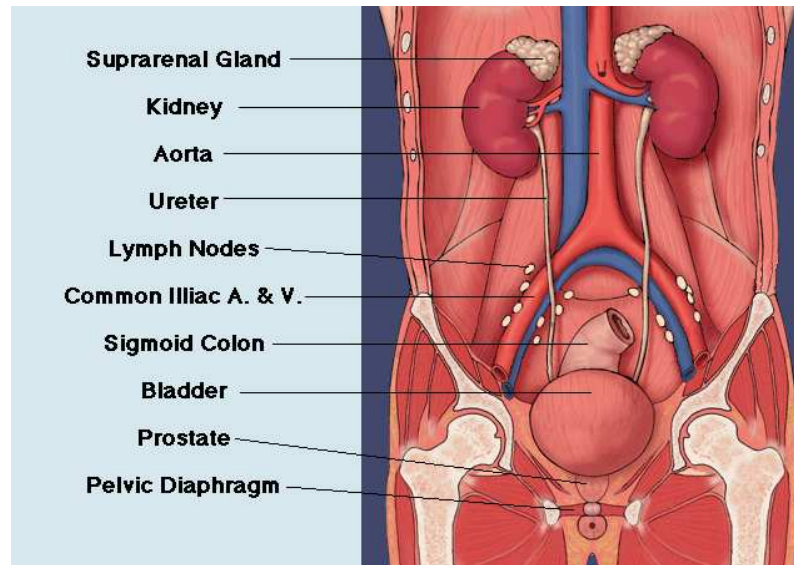


Figure 2.2: Anatomy section shows prostate, bladder and kidneys [2]

McNeal(1968) has identified three anatomical zones: the peripheral zone, transition zone and central zone, in Figure 2.4. The peripheral zone represents approximately 65% of the prostatic volume. This zone extends around the postero-lateral peripheral aspects of the gland from its apex to its base. The second largest part of the prostate is the central zone. It is a cone-shaped region that represents approximately 25% of the prostatic volume. The third zone of the prostate is called the transition zone, which represents only 5% to 10% of a typical prostatic volume.

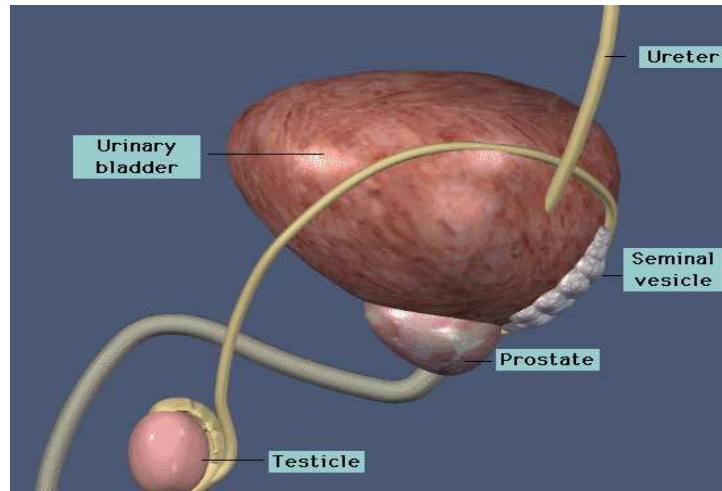


Figure 2.3: Location of the prostate gland [2]

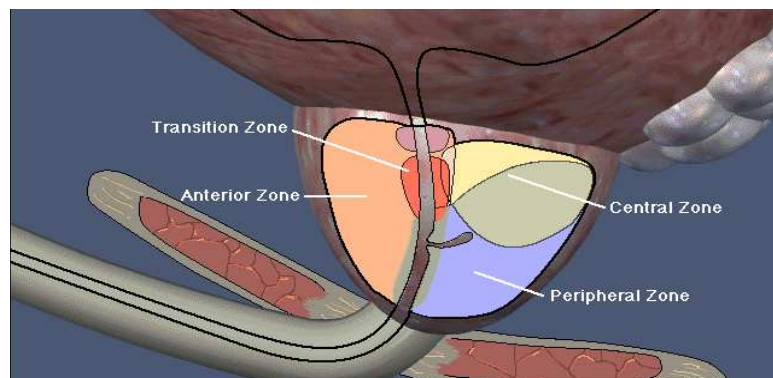


Figure 2.4: Anatomical zones of the prostate [2]

The transition zone is separated from the other two zones by a narrow band of fibromuscular stroma. It extends, in an arc, from the posterior urethra in the mid-prostate to the most anterior aspect of the gland. The clinical significance of zonal anatomy is best observed in BPH. Although it is clear that most nodular hyperplasia occurs in the transition zone, malignancy can affect any or all of the three zones. More than 70% of cases originate in the peripheral zone [3]. The percentage of malignancy in the transition zone is about 10–20%, and in the central zone, about 5–10%. The normal prostate size is 3–4 cm in width, 4–6 cm in length, and 2–3 cm in thickness. Malignancy can cause an increase in the prostate size, and BPH can increase the prostate size 100–200% [2].

2.3 Pathology

2.3.1 Development of BPH

BPH can be identified in the prostate as early as age forty to fifty years of life. BPH is not only due to an increase in the cell population, but is also to changes in the architecture of the ducts and acini. Nodular hyperplasia is a characteristic histological feature of BPH and occurs most commonly in the transition zone near the distal end of the bladder neck smooth muscle. Progressive transition zone enlargement results in a mean decline in the urinary flow rate. Nodular hyperplasia in the periurethral zone leads to a mass of dorsal tissue at the bladder neck [3].

2.3.2 Cancer Classification

The most common histological type is adenocarcinoma representing 98% of all prostatic cancers. Prostate cancer is classified as follows [2]:

- Acinar and proximal duct origin
- Distal duct origin
- Mixed carcinoma

2.4 Histological Grading of Prostate Cancer

The system, proposed by Gleason (1977), is the most widely accepted system. It is based on the architectural arrangement of malignant epithelial cells within the prostatic stroma. First, Gleason described nine reproducibly identifiable patterns of malignancy. In the 1970s, the Veterans Administration Urological Research Group determined the malignant potential of these patterns by their correlation to survival data. The nine patterns are arranged in five grades (1–5) in order of the ascending malignant potential, as exhibited in Figure 2.5 [7]. Gleason chose to adopt the sum of the two most predominant patterns instead of the average. Therefore, the malignant potential ranges from 2 to 10. The higher

the Gleason scores the more cancer that exists. The tumour volume and Gleason grading are closely correlated, as stated by McNeal in 1992 [3].

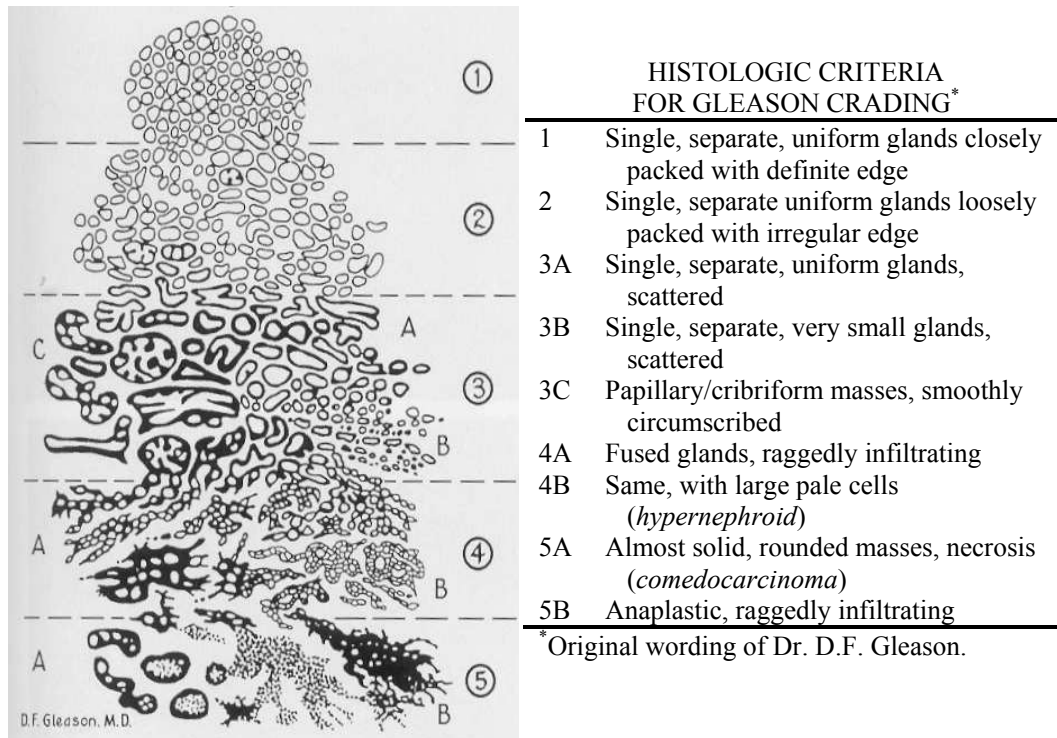


Figure 2.5: Gleason grading [7]

2.5 Early Detection

The early detection of prostate cancer is pivotal for the success of treatment. It is difficult to detect prostate cancer early, since it does not produce any symptoms in most patients. However, in advanced cases of prostate cancer, there are symptoms such as bladder outlet obstruction, acute urinary retention, neurological symptoms of cord compression or pathologic fractures secondary to bony metastases. The currently used screening tests are as follow [2, 7]:

- **Digital Rectal Exam (DRE):** It is easy and inexpensive, and is the most common test for prostate cancer detection. This exam can detect localize advanced cancers

with sufficient volume. However, the accuracy of the DRE exam is relatively low and is operator-dependent. The percentage of DRE positive predictive value is from 21% to 39%. In addition, the sensitivity of DRE is quite low (i.e., high false negative), indicating that DRE alone can not be relied on to detect prostate cancer.

- **Serum PSA:** PSA is considered as the best serum marker in the early detection of prostate cancer. PSA is an enzyme, secreted by prostatic cells. High PSA values (>10 ng/ml) have a positive predictive value equal to 66%. PSA values in the range of 4 to 10 ng/ml have a positive predictive value ranging from 22% to 35%. There is an overlap between prostate cancer and benign hyperplasia.
- **PSA Density:** It is defined as the PSA per unit prostate volume. It is useful to differentiate between prostate cancer and benign hyperplasia. The prostate volume can be found from TRUS screening.
- **PSA Velocity:** It is defined as the rate of change of serum PSA with time. For a normal prostate, PSAV is about 0.04 ng/ml/yr. However, for prostate cancer, PSAV is high (≈ 0.7 ng/ml/yr).
- **Age Specific PSA:** To increase the detection of prostate cancer in younger men and to reduce the biopsies of insignificant cancers in older patients, age should be considered in PSA cut-off values.
- **Free and Total PSA:** Malignant prostate cells produce less free PSA than hyperplasia tissue. Therefore, it is a useful test to differentiate between prostate cancer and benign hyperplasia.
- **TransRectal UltraSound (TRUS) and TRUS Biopsy:** TRUS is used to display the prostate, visualize the cancer, and guide the needles to obtain biopsies from the prostate. A TRUS image is illustrated in Figure 2.6. The most common approach to biopsies is the sextant approach. Biopsies from the basal, mid, and apical zones of the prostate are taken from both sides of the gland. TRUS can detect only the peripheral zone prostate cancer, which represents about 70% of prostate cancer. The accuracy of TRUS in detecting cancer is in the range of 57 to 76%.

- **MRI images:** It is very expensive and hardly used.

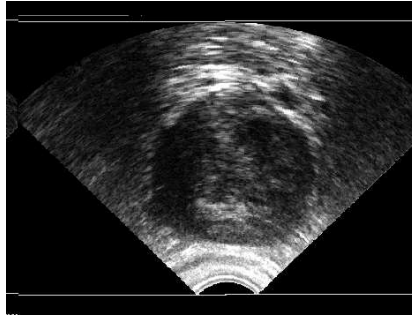


Figure 2.6: Transrectal ultrasound image

2.6 Prostate Cancer Progress

The prostate cancer progress is summarized as follows:

- Intraprostatic spread Figure 2.7
- Seminal vesicle spread Figure 2.8
- Extracapsular spread Figure 2.9
- Lymph node spread Figure 2.10

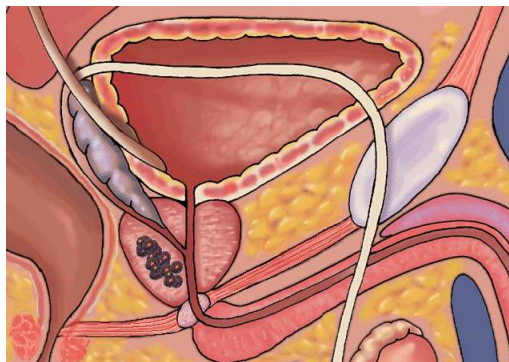


Figure 2.7: Intraprostatic spread [2]

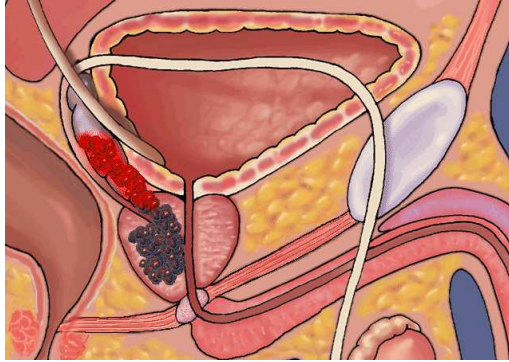


Figure 2.8: Seminal vesicle spread [2]

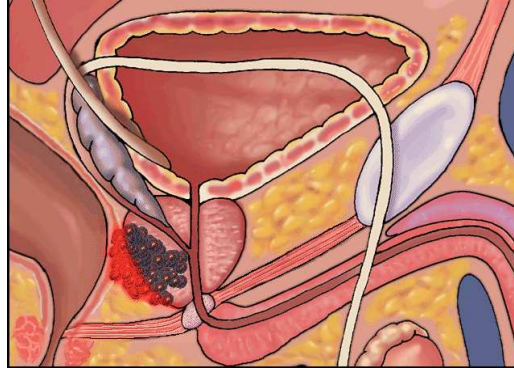


Figure 2.9: Extracapsular spread [2]

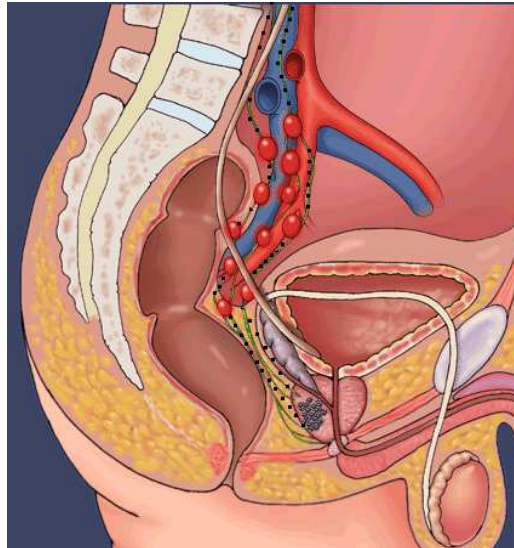








Figure 2.10: Lymph nodal spread [2]

2.7 Prostate Cancer Staging

Prostate cancer staging represents the extent of the cancer. Tumour Node Metastasis (TNM) is used for staging the prostate cancer. The prostate cancer stages are listed in Table 2.1.

Table 2.1: Tumour node metastasis staging [2, 7]

Stage	Description
<p style="text-align: center;">T1</p> 	<p>TX: primary tumour cannot be assessed T0: No evidence of primary tumour T1: The tumour is neither visible in images nor palpable in DRE</p> <p style="padding-left: 20px;">T1a: Incidental histologic finding; <5% of tissue resected during TURP T1b: Incidental histologic finding; >5% of tissue resected during TURP T1c: Tumour identified by needle biopsy due to an elevated PSA</p>
<p style="text-align: center;">T2</p> 	<p>T2: The tumour is palpable, whether or not visible on TRUS.</p> <p style="padding-left: 20px;">T2a: Tumour involves one lobe T2b: Tumour involves both lobes</p>
<p style="text-align: center;">T3</p> 	<p>T3: Tumour extends through the prostatic capsule</p> <p style="padding-left: 20px;">T3a: Extracapsular extension (unilateral or bilateral) T3b: Tumour invades seminal vesicle(s)</p>
<p><i>continued on next page</i></p>	

<i>continued from previous page</i>	
Stage	Description
<p>T4</p> 	<p>T4: Tumour is fixed or invades adjacent structures other than seminal vesicles: bladder neck, external sphincter, rectum, levator muscles, and/or is fixed to pelvic wall</p>
<p>N</p> 	<p>N: Regional lymph nodes NX: Regional lymph nodes cannot be assessed N0: No lymph node metastasis N1: Metastasis in regional lymph node or nodes</p>
<p>M</p> 	<p>M: Distant Metastasis MX: Distant metastasis cannot be assessed M0: No distant metastasis M1: Distant metastasis M1a: Nonregional lymph node(s) M1b: Bone(s) M1c: other sites</p>

2.8 Summary

In this chapter, the anatomy of the prostate, prostate cancer and staging of prostate cancer are introduced. The early detection of prostate cancer plays a crucial role in the success of

the cancer treatment. There are several screening tools to detect prostate cancer, including TRUS and MRI imaging. MRI images are very clear, compared with TRUS images, which contain noise such as speckles, shadowing, and other image artifacts. However, MRI screening is more costly and not available in many community hospitals, is time consuming, and requires more patient preparation time. Therefore, TRUS is more commonly used than MRI for screening and biopsy guidance for prostate cancer. More details of the characteristics of ultrasound are given in Appendix A. In this investigation TRUS images are chosen for this research. The challenge is to use ultrasound images and perform some noise reduction techniques so that an appropriate segmentation technique can be developed to segment the prostate gland and to find the cancerous regions inside the prostate.

Chapter 3

Image Segmentation

3.1 Introduction

Image segmentation plays an important role in medical applications. Such segmentation helps in delineating the anatomy of an organ and its volume. This is crucial in the diagnosis of prostate cancer, where the ratio of the PSA to the volume of the prostate is important to detect cancer and aid in treatment planning [8]. Medical images, in general, are difficult to segment, especially, ultrasound images which suffer from a lack of contrast and are corrupted by speckle noise [9]. In this chapter, a background of image segmentation is given. In addition, the most common image segmentation techniques are examined. The focus in this chapter is on the deformable models which is a superior approach for medical image segmentation.

3.2 Background

3.2.1 Definition

Image segmentation divides an image into regions with no overlapping. Each region possesses different features including colour, intensity, texture or other statistical properties. If the domain of the image is given by Ω , hence the sets $R_k \subset \Omega$ represent the segments of the image. The union of all the segments results in the whole image again. The sets,

which represent the segmentation, must satisfy the following:

$$\Omega = \bigcup_{k=1}^k R_k, \quad (3.1)$$

where $R_k \cap R_j = \emptyset$ for $k \neq j$, and each R_k is connected. If this constraint, which states that the regions are connected, is removed, the segmentation problem becomes a classification problem; then the sets, themselves, are called classes instead of segments. The direct way to segment an image is by applying an edge detection technique, especially if the image consists of clear objects on a different intensity background. However, this technique can fail, if the image contains noise [8].

3.2.2 Interaction

There is a trade-off between manual interaction and automatic segmentation. The advantage of manual interaction is that it depends on the prior knowledge of an operator, but the disadvantage is that the results are operator-dependent and requires much time and effort [8].

3.2.3 Validation

Validation experiments are necessary to quantify the performance of a segmentation technique. They can be conducted by comparing an automatic segmentation with the manual segmentation of an expert. Another common approach is the use of physical phantoms or computational phantoms [8].

3.3 Segmentation Techniques

There are many segmentation techniques. However, there is no standard segmentation technique that works well for all images. This section highlights eight common segmentation techniques summarized as follows.

1. Thresholding

2. Region growing
3. Classification
4. Clustering
5. Markov Random Field (MRF) Models
6. Artificial Neural Networks
7. Deformable Models
8. Atlas-Guided

3.3.1 Thresholding

The thresholding technique is the simplest image segmentation technique. It is based on the assumption that the objects and the background in the image have a bimodal distribution. Typically, this assumption is not valid for most images, especially medical ones. The key point in this segmentation technique is to determine an intensity value, called the threshold, which separates the desired classes. Thresholding segmentation transforms input image Ω to a binary image g by grouping the pixels with intensities, higher than the threshold into one class, and the other pixels into another class.

For any 2D digital image,

$$\{\Omega(i, j) | i \in \{1, 2, \dots, M\}, j \in \{1, 2, \dots, N\}\}, \quad (3.2)$$

the thresholding technique is defined as

$$g(i, j) = \begin{cases} 1, & \text{for } \Omega(i, j) \geq T \\ 0, & \text{for } \Omega(i, j) < T. \end{cases} \quad (3.3)$$

Some images can be segmented by using more than one thresholding point, which is called multi-thresholding, as depicted in Figure 3.1, where T_1 and T_2 are the two thresholds segmenting the image.

The output image, resulting from multi-thresholding, is no longer binary, but consists of a limited number of grey levels as follows:

$$g(i, j) = \begin{cases} 0, & \text{for } \Omega(i, j) < T_1 \\ 1, & \text{for } T_1 \leq \Omega(i, j) < T_2 \\ \vdots & \\ n, & \text{for } T_n \leq \Omega(i, j) < N_g - 1, \end{cases} \quad (3.4)$$

where N_g = the number of grey levels in the image (256).

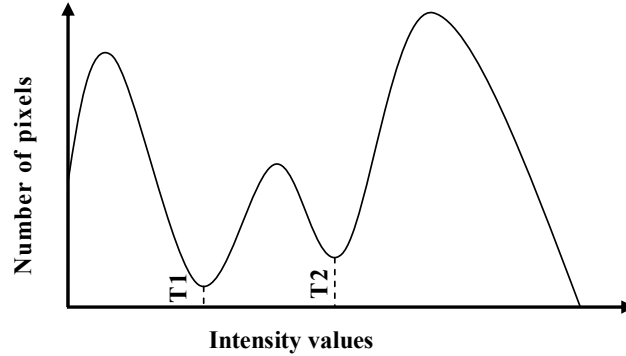


Figure 3.1: Histogram showing three apparent classes, using two thresholds T_1 and T_2

There are two main methods of thresholding segmentation. The simplest and fastest method is called global thresholding, where one threshold value is used for the entire image. The second method is called local thresholding, where a different threshold value is assigned to each sub-image. Although the second method is more accurate than the previous one, the second one is more computationally complex. To determine the threshold value, the histogram of the image is calculated and the minimum value of the histogram is used as the threshold value. The histogram can be mathematically described as follows:[8, 10].

Let the histogram be

$$h(x), x \in G \text{ and } G = \{0, 1, \dots, N_g - 1\}, \quad (3.5)$$

where $h(x)$ represents the density function and is derived from:

$$h(x) = Prob(\Omega(m, n) = x) = \frac{\text{number of pixels with the grey value} = x}{\text{Total number of pixels in the image}}. \quad (3.6)$$

There are many techniques for determining the optimal thresholding value from the histogram, as signified in Figure 3.2. These techniques can then be divided into six main categories [11]:

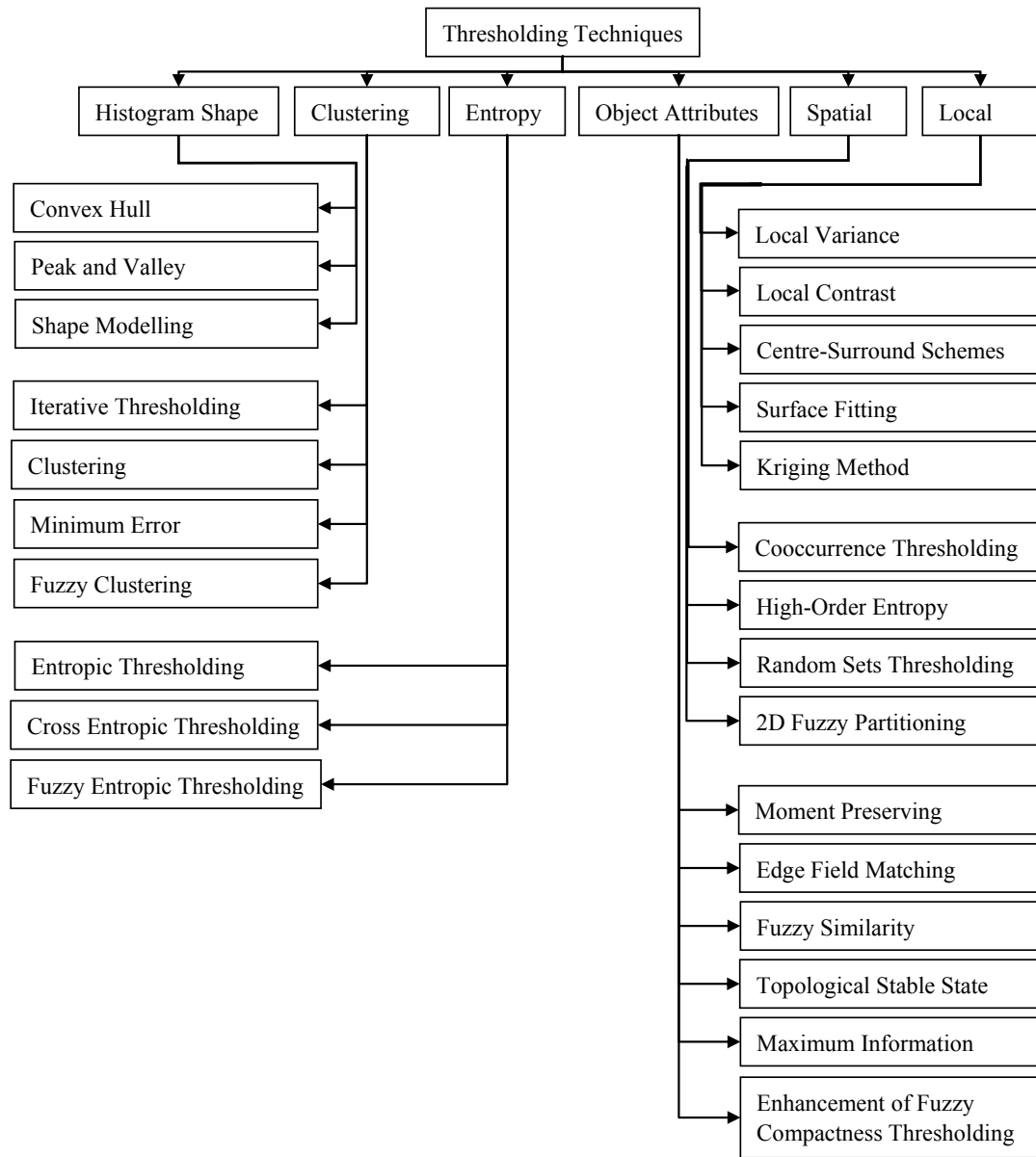


Figure 3.2: Thresholding techniques

1. Histogram shape-based techniques
2. Clustering-based techniques
3. Entropy-based techniques
4. Object attribute-based techniques
5. Spatial techniques
6. Local techniques

Excellent reviews are described in the literature [10–19]. Thresholding is used to detect the pubic arch in TRUS during transperineal prostate brachytherapy [20]. The technique is also used at the initial stage in multi-stage segmentation techniques. It yields coarse estimation of the objects in the image, which can be modified [21–23]. One limitation of the global thresholding technique is that it does not include the spatial information of the image. One solution is the connectivity-based thresholding algorithm, proposed by Chulhee et al. [24]; However, the thresholding technique is not powerful enough for a complicated problem such as prostate segmentation in TRUS.

3.3.2 Region Growing

This segmentation technique depends on extracting a region from the image that has the same characteristics such as intensity level or other statistical information. The straightforward region growing technique requires, first, a seed point to begin from, as portrayed in Figure 3.3. Then, the pixels connected to the seed point that have the same predefined characteristics are found. This seed point can be manually or automatically selected.

The goal of region growing segmentation is to divide the image into its regions, according to image properties such as pixel intensity, spectral values, and textural properties. Assume the entire image region is Ω . The purpose is to divide Ω into R_1, R_2, \dots, R_n such that [25]

$$\bigcup_{i=1}^n R_i = \Omega,$$

R_i is a connected region, $\forall i$,

$$R_i \cap R_j = \emptyset \quad \forall i, j; i \neq j,$$

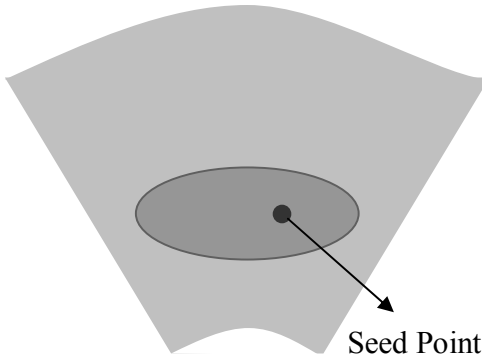


Figure 3.3: Example of region growing

$$P(R_i) = True, \forall i,$$

and

$$P(R_i \cup R_j) = False \forall i, j; i \neq j.$$

where $P(R_i)$ is a logical predicate over the set of pixels in R_i . Region growing is categorized into three classes [25].

1. Merging: The seed points inside the objects, which require to be segmented, are defined. Then, the regions grow from these seed points by adding the neighbouring pixels of the seed points, which have similar properties. The disadvantage of this method is that the segmentation results depend on the order in which each region in the image is processed [26].
2. Splitting: The goal is to divide the image into regions. The algorithm splits until $P(R_i) = True$. The disadvantage is that the final segmentation can contain adjacent regions with the same properties [25].
3. Split and Merge: This technique is a combination of the previous techniques. Maria et al. has summarized this technique as [25].
 - (a) Split any region R_i where $P(R_i) = False$ into four square regions.
 - (b) Merge any adjacent regions R_j and R_k for which $P(R_j \cup R_k) = True$.
 - (c) Stop if there is no further merging or splitting possible, otherwise, repeat steps (a) and (b).

Much research has been carried out in the segmentation field by using region growing [27–30]. Bozidar has developed an automatic region growing segmentation to detect ovarian follicles with a recognition rate of approximately 78%. Also, he has used the thresholding technique for preprocessing to determine the seed points [21]. Region growing is also relied on to calculate the volume of the prostate by a manually identified seed point in the centre of the prostate gland [31]. The critical point in the region growing segmentation technique is how to choose noise insensitive properties for each object to correctly segment the image.

3.3.3 Classification

Classification methods are pattern recognition techniques, where a feature space is partitioned by using data with known labels. The image intensities are the most common features. Histograms are a 1D feature space as shown in Figure 3.1. An example of a two-feature space is shown in Figure 3.4. There are many classification techniques in image

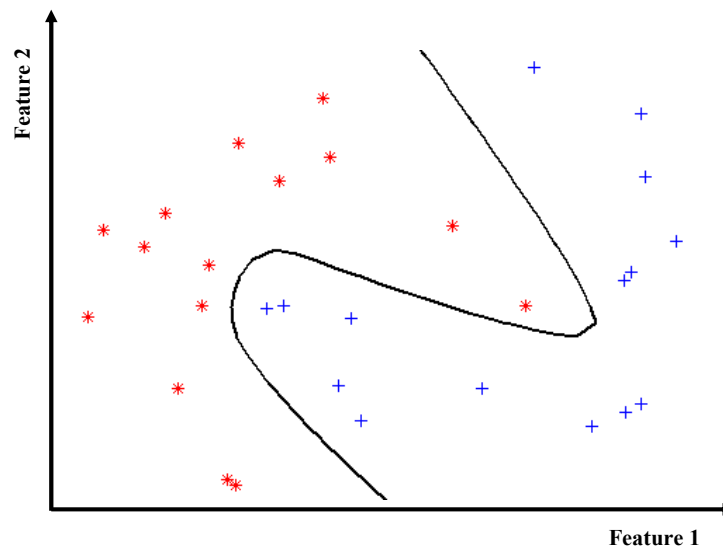


Figure 3.4: 2D feature space

segmentation. The principal drawback of such segmentation approach is that training data

is required. Training data is not always available in medical field. Also, anatomical and physiological variability in the training data decreases the accuracy of the results [8]. The Bayesian classifier is adopted in image segmentation [32, 33]. The disadvantage is that the technique depends on a training data set to estimate the parameters of the assumed probability distribution function, which makes the results biased to the training set. The nearest neighbouring technique is adopted in image segmentation, but it requires a large storage space and a long computation time [34, 35]. There are much research [36–39] is conducted in the segmentation field using classification approach. They include classification techniques such as K-NN [40], neural networks [41–44], and fuzzy logic [45].

3.3.4 Clustering

Clustering techniques are similar to classification ones except that clustering techniques are unsupervised. They iteratively alternate between characterizing the properties of each class and segmenting the image. Researchers usually apply these techniques by using the intensity levels as a feature, which produces results that are sensitive to noise [8]. Therefore, it should take into account the spatial information to produce meaningful results. The accuracy of the clustering techniques is usually less than that of the classification techniques, a primary limitation. The most common clustering algorithms used in medical image segmentation are:

1. The K-Means
2. The Fuzzy C-Means
3. The Expectation-Maximization (EM)

3.3.4.1 The K-Means or ISODATA Algorithm

The k-means is a simple and easy to perform clustering technique. It has been used successfully in functional MRIs to distinguish between large veins and activated grey matter [46]. Yan et al. [47] has employed an adaptive k-means to segment 3D MRIs into grey, white matter, CSF, and other abnormal tissues. The proposed methodology is insensitive to the shading effect. Chen et al. [48] have used adaptive k-means with knowledge-based

morphological operations to segment 3D images. The results are very close to those of manual segmentation. The average percentage difference between the proposed algorithm and the manual segmentation is 6.7% in volume and 1.9% in surface area. Note that the purpose of the k-means technique is to cluster N data points with M -dimensional feature space into k clusters. The classification space F is defined as follows [46]:

$$F_i = [f_{i1}, f_{i2}, \dots, f_{iN}]^T, i = 1, 2, \dots, M. \quad (3.7)$$

The goal of this technique is to minimize the sum of the square distance within the cluster between the pixels and the centre of the cluster by moving pixels from one cluster to another. The objective function for minimizing is [46]:

$$\varepsilon = \sum_{j=1}^N D^2(j, k), \quad (3.8)$$

where $D(j, k)$ is the Euclidian distance of j^{th} pixel from the mean of the k^{th} cluster which is defined by [46]:

$$D^2(j, k) = \sum_{i=1}^M \{ [f_{ij} - \mu(k, i)]^2 \times W(k, i) \} \quad (3.9)$$

where $\mu(k, i)$ is the mean of the i^{th} feature within the k^{th} and $W(k, i)$ is a weighting factor.

The procedure for k-means clustering is summarized as follows [46].

- Normalize the feature vectors by their variance
- Initialize the value of the mean of class 1 " $\mu(1, i)$ " by the value of the furthest pixel in the feature space.
- Initialize the value of the mean of class 2 by the value of the furthest pixel from the mean of class 1.
- Initialize the value of the mean of class 3 by the value of the furthest pixel from both class 1 and class 2. By the same way, the means of all k classes are initialized.
- Minimize the objective function iteratively by moving the pixels form one class to another.

3.3.4.2 The Fuzzy C-Means Algorithm

The Fuzzy c-means algorithm is a generalization of the k-means, allowing for soft segmentation [8]. This algorithm is developed by Dunn in 1973 [49] and is improved by Bezdek in 1981 [50]. Qing et al. [51] have proposed a modification of the fuzzy c-means to reduce the computational time. In this algorithm, the histogram is used to find the centres of the grey levels, enhancing the performance of the algorithm. Fuzzy c-means has also been employed in MRI segmentation [52]. The images are first enhanced by using a wavelet-based de-noising, before applying the fuzzy c-means. It is also combined with the Hopfield neural network to segment multispectral MRI brain images. The proposed algorithm is fully automatic which is desirable [53].

The objective function of this algorithm is [51]

$$J(U, V) = \sum_{k=1}^n \sum_{i=1}^c (U_{ik})^m (d_{ik})^2 \quad (3.10)$$

where,

c = number of classes

m = weighting exponent, for hard clustering, $m = 1$

d_{ik} = the inner product induced norm metric

n = number of data sets

U_{ik} = fuzzy membership values of pixel k in cluster i

V_i = cluster centre of class i

U = Fuzzy c-partition

The goal of this algorithm is to find U and V to minimize the objective function. This is achieved by using an iterative technique, which is described as follows [51].

- Choose the number of clusters $c, 2 < c < n$, weighting exponent $m > 1$
- Initialize the partition matrix $U^{(0)}$
- Repeat for $b = 1, 2, \dots$

1. Compute the cluster prototypes (means) $V_j^{(b)}$ from $U^{(b)}$

$$V = \frac{\sum_{k=1}^n (U_{ik})^m X_k}{\sum_{k=1}^n (U_{ik})^m}. \quad (3.11)$$

2. Update the partition matrix $U^{(b)}$

- (a) Compute I_k and T_k by

$$I_k = \{i | 1 < i < c, d_{ik} = |x_i - v_k| = 0\}. \quad (3.12)$$

$$T_k = \{1, 2, \dots, c\} - I_k. \quad (3.13)$$

- (b) Calculate the new membership values

- i. If $I_k = 0$,

$$U_{ik} = \frac{1}{\sum_{j=1}^c (d_{ik}/d_{jk})^{\frac{2}{m-1}}}. \quad (3.14)$$

- ii. Else, $U_{ik} = 0$, for all $i \in T_k$ such that

$$\sum_{i \in I_k} U_{I_k} = 1. \quad (3.15)$$

3. Until $\|U^{(b)} - U^{(b-1)}\| < \varepsilon$.

3.3.4.3 The Expectation-Maximization (EM) Algorithm

This is a statistical approach. It is adopted for the parameter estimation for retina image segmentation [54], and depth estimating to recover 3D information from images sets [55]. Zhang et al. [56] have employed EM with a hidden Markov random field model to segment MRI images. They show that the proposed framework can segment 3D MRI brain images automatically. The assumption in the EM family is that the image is a mixture of distribution realization and probability distribution, following a Gaussian model. The EM technique does not include spatial information, which is essential for accurate image segmentation, a severe limitation [8, 54].

3.3.5 Markov Random Field Models

A Markov random field is a statistical model that can be used in image segmentation with EM to automatically segment 3D MRI images [56]. Also, the model is used in texture segmentation [57] to model the interactions among neighbouring pixels. The drawback is that it is difficult to select the proper parameters, which control the strength of the spatial interaction [8, 56].

3.3.6 Artificial Neural Networks (ANNs)

Artificial Neural Networks (ANNs), also called Artificial Neural Systems (ANSs), neuro-computers, Parallel Distributed Processors (PDPs) or connectionist models are an attempt to mimic the structure and functions of the brain and nervous system of a living creature. Generally speaking, an ANN is an information or signal processing system composed of a large number of simple processing elements, called artificial neurons, or simply nodes. They are interconnected by direct links called connections that cooperate to perform parallel distributed processing to solve a computational task. One of the attractive features of ANNs is their capability to adapt to special environmental conditions by changing their connection strengths or structures. NNs are used in medical image segmentation [8, 41–44]. The main limitation of this technique is that it requires a large training data set which is not always available.

3.3.7 Deformable Models

The deformable models are used in many applications [58–75] including prostate segmentation. Therefore, this technique is described in more detail in this section. In the early 1970s, an optimization method to find the object boundary in images was reported [76–80], but was not well-known until Kass et al. [58] presented their research in 1987. Following up on this, many deformable models were derived from different optimizing methods [65], including the simulated annealing technique [81], dynamic programming [82], parametrical space method [83], finite element method [84, 85], finite difference method [86], and greedy algorithm [87]. The deformable contour is also called active contour, or snake. Deformable model is a curve or surface that deforms under the influence of internal and external forces.

The internal forces retain the smoothness of the contour during deformation. The external forces are computed from the image itself to drive the contour to the desired object by using edge information [82–87], region information, or both [65]. Various methods have been suggested to drive the contour by the use of region information. For example, the contrast of the grey levels between the inside and outside of the object was adopted as a measure for the region information by O’Sullivan et al. [88]. Storvik [81] has adopted the distribution of grey levels inside and outside the object in his energy function. A region-based model based on the Ward distance has been introduced by Ronfard [89]. Moreover, statistical features such as the mean and standard deviation can represent regional information as in [90, 91]. Edge information is easier to implement than regional information, yet the image noise can affect techniques which use edge information more than regional information. Therefore, the techniques for edge information require that the initial contour be very close to the desired boundary [65]. Also, edge information or regional information depends on the properties of the image. Some researchers [92–95] have developed a more complicated approach by combining both edge and regional information to drive the contour to the desired boundary.

Two techniques of deformable models are parametric deformable models and geometric deformable models. The former models characterize the contour explicitly by parameters, and the latter models characterize the contour implicitly as a level set of a developing scalar function [96]. Both are elaborated on in the following sections.

3.3.7.1 Parametric Deformable Models

The contour in the parametric models is represented as $X(s) = [x(s), y(s)]$, $s \in [0, 1]$. The goal is to minimize the following energy function [96]:

$$E = \int_0^1 \frac{1}{2} \left(\alpha |X'(s)|^2 + \beta |X''(s)|^2 \right) + E_{ext}(X(s)) \quad ds. \quad (3.16)$$

Weighting factors α and β control the tension and the rigidity of the contour respectively, where $X'(s)$ and $X''(s)$ represent the first and the second derivatives of $X(s)$ with respect to s , respectively. E_{ext} represents the external energy which drives the contour to the

object boundary. The straight forward method to calculate the external energy is [96].

$$E_{ext}(x, y) = -|\nabla (G_\sigma(x, y) * \Omega(x, y))|^2, \quad (3.17)$$

where

$\Omega(x, y)$ is a grey level image

$G_\sigma(x, y)$ is a 2D Gaussian function to smooth the image

σ is the standard deviation

∇ is gradient operator

The deformable contour must satisfy the Euler equation as follows:

$$\alpha X''(s) - \beta X''''(s) - \nabla E_{ext} = 0 \quad (3.18)$$

To represents the force balance equation as follows:

$$F_{int} + F_{ext} = 0. \quad (3.19)$$

Since the contour changes with time, X should be manipulated as a function of both t and s . Thus, 3.18 should be reformed as

$$X_t(s, t) = \alpha X''(s) - \beta X''''(s) - \nabla E_{ext}. \quad (3.20)$$

Equation 3.20 should be solved numerically. When the contour achieves the final shape, term $X_t(s, t)$ becomes equal to zero which satisfies the Euler equation 3.18. Two complexities face traditional parametric models. The first is that the initial contour should be very close to the object boundary; Secondly, the active contours have some problems advancing into boundary concavities. Chenyang Xu et al. [62] have developed an impressive technique to overcome these problems called the "Gradient Vector Flow (GVF) Deformable Models". This technique is very promising, and is applied in the research described in this thesis to segment the prostate from ultrasound images.

3.3.7.1.1 Gradient Vector Flow (GVF) Deformable Models

Chenyang Xu et al. [62] have introduced a new static external force $F_{ext} = V(x, y)$ called GVF field. Then they have replaced the potential force ∇E_{ext} with the new force $V(x, y)$ in 3.20 as follows:

$$X_t(s, t) = \alpha X''(s) - \beta x''''(s) + V. \quad (3.21)$$

The GVF is defined by vector $V(x, y) = [u(x, y), v(x, y)]$ which minimizes the following energy functional:

$$\varepsilon = \iint \mu (u_x^2 + u_y^2 + v_x^2 + v_y^2) + |\nabla f|^2 |V - \nabla f|^2 dx dy, \quad (3.22)$$

where μ is a regularization coefficient whose value depends on the amount of noise in the image (more noise increases μ). f is the edge map and is calculated as follows:

$$f(x, y) = -E_{ext}(x, y), \quad (3.23)$$

and E_{ext} is calculated as shown in 3.17.

The GVF field is evaluated by the calculus of variations by solving the following Euler equations:

$$\mu \nabla^2 u - (u - f_x)(f_x^2 + f_y^2) = 0, \quad (3.24)$$

and

$$\mu \nabla^2 v - (v - f_y)(f_x^2 + f_y^2) = 0. \quad (3.25)$$

Figure 3.5 exhibits the superiority of this technique over the conventional deformable contour. Figure 3.5(b) illustrates the wide range of GVF contours, and Figure 3.5(c) demonstrates that the GVF contour can handle concavities easily. A detailed analysis of GVF contour which demonstrates its superiority over the traditional contours and various examples, can be found in the literature [96].

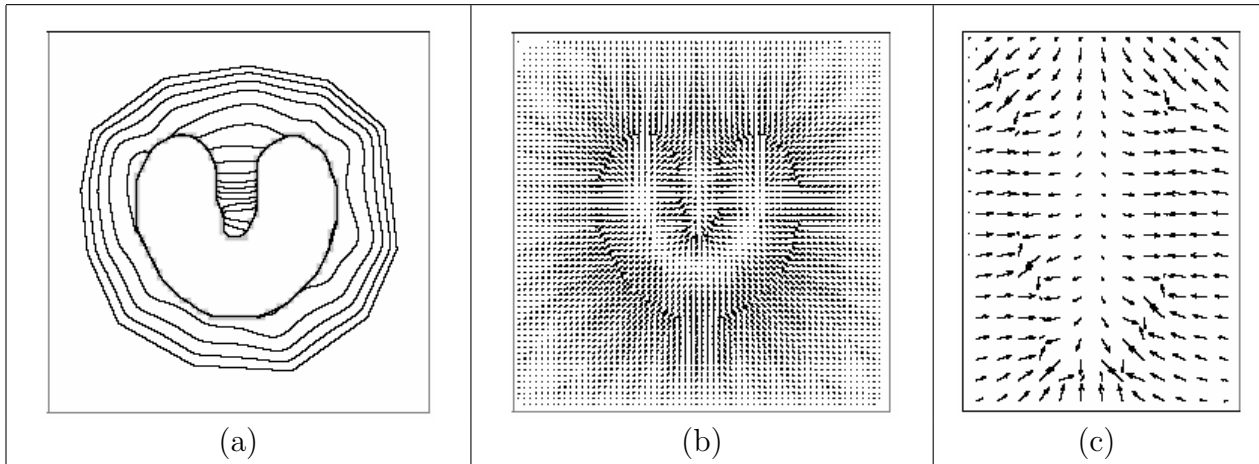


Figure 3.5: (a) Contour convergence, (b) GVF external force and (c) Boundary concavity [96]

3.3.7.2 Geometric Deformable Models

Parametric deformable models have many attractive attributes such as smoothness, connectivity, the capability to integrate knowledge about the object which needs to be segmented. However, the parametric contours do not represent topology changes such as splitting and merging of the contours very well, and the dynamic contour needs to be reparameterized after each step by defining new equal-spaced vertices adding to the complexity of the problem. Geometric models with a level set technique overcome these drawbacks by adding an extra dimension to the problem. It transfers the problem from a moving curve to a moving surface, which seems to be more difficult. However, the topological problem is simplified, which makes the extension from 2D to nD a straight forward process [97, 98].

In 1998, the concept of geometric contours was introduced by Osher and Sethian [99]. There are many applications for level set [100] such as shape detection and recovery [101–104], image enhancement [105, 106], robotic navigation with constraints [107], microchip manufacturing [108–110], optimal design [111], and geometry [112].

To formulate geometric contours mathematically [61, 100], let Ω be a bounded open subset of \mathbb{R}^2 , and $\partial\Omega$ be its boundary. For 2D images, Ω is a fixed rectangular grid. The curve C in Ω is the boundary of a subset ω of Ω . The point of this technique is to add

another dimension to the problem to represent a scalar function ϕ , the level set function. The contour C is represented by the zero level set as follows:

$$C = \{(x, y) \in \Omega : \phi(x, y) = 0\}. \quad (3.26)$$

Initially, the level set function ϕ for any pixel of the image Ω is defined by

$$\phi(x, y, t = 0) = \pm d \quad (3.27)$$

where d is the distance from the current pixel (x, y) to the contour C at $t = 0$. The pixels inside the contour are calculated by using $+d$, whereas the pixels outside the contour are evaluated by using $-d$. The geometric contour deforms according to the following partial differential equation:

$$\frac{\partial \phi}{\partial t} = F |\nabla \phi|, \phi(x, y, 0) = \phi_o(x, y), \quad (3.28)$$

where the initial contour is defined as the set $\{(x, y) \in \Omega : \phi_o(x, y) = 0\}$, and F is the speed function. Various forms for the speed function F are introduced in the literature. Many of them depend on the image gradient as a stopping criterion. For instance, Caselles et al. [113] have used the following form for the evolving contour:

$$\left\{ \begin{array}{l} \frac{\partial \phi}{\partial t} = g(|\nabla \Omega|) |\nabla \phi| (\kappa + \nu), \\ \phi(x, y, 0) = \phi_o(x, y), \\ \kappa = \text{div} \left(\frac{\nabla \phi}{|\nabla \phi|} \right), \\ g(|\nabla \Omega(x, y)|) = \frac{1}{1 + |\nabla G_\sigma(x, y) * \Omega(x, y)|^p}, p \geq 1 \end{array} \right. \quad (3.29)$$

where

$g(|\nabla \Omega|)$ is an edge function with $p = 2$

$\nu \geq 0$ is a constant

ϕ_o is an initial level set function

κ is the curvature function

$G_\sigma(x, y)$ is the 2D Gaussian function used to smooth the image Ω

σ is the standard deviation

∇ is gradient operator

Another form of the speed function has been introduced by Malladi et al. [114] as follows:

$$\begin{cases} \frac{\partial \phi}{\partial t} = |\nabla \phi| \left(-\nu + \frac{\nu}{(M_1 - M_2)} (|\nabla G_\sigma * \Omega| - M_2) \right) \\ \phi(x, y, 0) = \phi_o(x, y), \end{cases} \quad (3.30)$$

where

ν is a constant

M_1 is the maximum of the magnitude of the image gradient $|\nabla G_\sigma * \Omega|$

M_2 is the minimum of the magnitude of the image gradient $|\nabla G_\sigma * \Omega|$

The primary limitation of the geometric deforming contours, which are based on an edge criterion, is that they require a clear edge. A powerful technique which overcomes this limitation was introduced by Chan et al. [61] called the *active contours without edges*, and is capable of segmenting objects with weak or noise edges. This technique is discussed in the next section.

3.3.7.2.1 Active Contours without Edges

This technique is applied to find multi-regions easily. Since, it does not need a clear or complete boundary for the regions, the technique is a good candidate for segmenting the hypoechoic regions inside the prostate. The idea of this technique is to minimize the following function [61]:

$$F(c_1, c_2, C) = F_1(C) + F_2(C) = \int_{inside(C)} |\Omega(x, y) - c_1|^2 dx dy + \int_{outside(C)} |\Omega(x, y) - c_2|^2 dx dy, \quad (3.31)$$

where C is the deformable curve, while c_1 and c_2 are the averages of the intensity levels of the image Ω inside and outside the curve C respectively.

Figure 3.6 demonstrates that minimizing the function 3.31 leads the contour to the boundary of the object. It is also evident that the only case that minimizes the function occurs when the contour is on top of the boundary of the object.

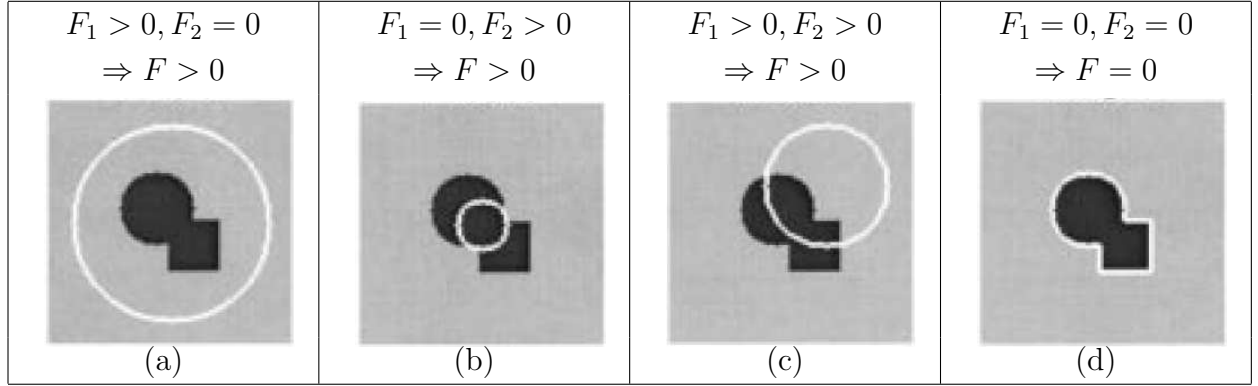


Figure 3.6: Possible locations of the contour relative to the object [61]

The complete energy function that needs to be minimized is [61]:

$$\begin{aligned}
 F(c_1, c_2, C) = & \mu \cdot \text{Length}(C) + \nu \cdot \text{Area}(\text{inside}(C)) \\
 & + \lambda_1 \int_{\text{inside}(C)} |\Omega(x, y) - c_1|^2 dx dy \\
 & + \lambda_2 \int_{\text{outside}(C)} |\Omega(x, y) - c_2|^2 dx dy,
 \end{aligned} \tag{3.32}$$

where $\mu \geq 0, \nu \geq 0, \lambda_1 > 0$ and $\lambda_2 > 0$ are weighting factors. Chan et al. [61] have used the level set technique to minimize the previous energy function. The zero level set of a Lipschitz function ϕ is represented by contour C as indicated in Figure 3.7. The problem is formulated as

$$\begin{aligned}
 C = \partial\omega &= \{(x, y) \in \Omega : \phi(x, y) = 0\}, \\
 \text{inside}(C) = \omega &= \{(x, y) \in \Omega : \phi(x, y) > 0\}, \\
 \text{outside}(C) = \Omega \setminus \bar{\omega} &= \{(x, y) \in \Omega : \phi(x, y) < 0\}.
 \end{aligned} \tag{3.33}$$

Then, the unknown contour C is replaced by the unknown level set function ϕ by using the Heaviside function H and Dirac measure δ_o which are defined as

$$H(z) = \begin{cases} 1, & \text{if } z \geq 0 \\ 0, & \text{if } z < 0 \end{cases} \quad \delta_o(z) = \frac{d}{dz} H(z). \tag{3.34}$$

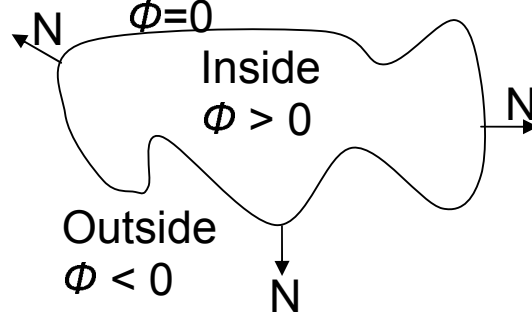


Figure 3.7: Level set representation

Thus, the length term can be reformulated in terms of the level set function ϕ as follows:

$$\begin{aligned} \text{Length} \{ \phi = 0 \} &= \int_{\Omega} |\nabla H(\phi(x, y))| dx dy \\ &= \int_{\Omega} \delta_o(\phi(x, y)) |\nabla \phi(x, y)| dx dy. \end{aligned} \quad (3.35)$$

The area term is represented by using the following level set function ϕ .

$$\text{Area} \{ \phi \geq 0 \} = \int_{\Omega} H(\phi(x, y)) dx dy. \quad (3.36)$$

The last two terms $F_1(C)$ and $F_2(C)$ of the energy function F is reformulated by the level set function ϕ such that:

$$\int_{\phi > 0} |\Omega(x, y) - c_1|^2 dx dy = \int_{\Omega} |\Omega(x, y) - c_1|^2 H(\phi(x, y)) dx dy, \quad (3.37)$$

and

$$\int_{\phi < 0} |\Omega(x, y) - c_2|^2 dx dy = \int_{\Omega} |\Omega(x, y) - c_2|^2 (1 - H(\phi(x, y))) dx dy. \quad (3.38)$$

As a result, the complete energy function is reformulated as

$$\begin{aligned} F(c_1, c_2, \phi) &= \mu \int_{\Omega} \delta(\phi(x, y)) |\nabla \phi(x, y)| dx dy \\ &\quad + \nu \int_{\Omega} H(\phi(x, y)) dx dy \\ &\quad + \lambda_1 \int_{\Omega} |\Omega(x, y) - c_1|^2 H(\phi(x, y)) dx dy \\ &\quad + \lambda_2 \int_{\Omega} |\Omega(x, y) - c_2|^2 (1 - H(\phi(x, y))) dx dy. \end{aligned} \quad (3.39)$$

Also, c_1 and c_2 are represented in terms of ϕ as follows:

$$c_1(\phi) = \frac{\int_{\Omega} \Omega(x, y) H(\phi(x, y)) dx dy}{\int_{\Omega} H(\phi(x, y)) dx dy} \quad (3.40)$$

and

$$c_2(\phi) = \frac{\int_{\Omega} \Omega(x, y) (1 - H(\phi(x, y))) dx dy}{\int_{\Omega} (1 - H(\phi(x, y))) dx dy}. \quad (3.41)$$

Therefore, the energy function is now a function of one scalar function, and can be solved numerically to find the level set function ϕ that minimizes the energy function. The final contour is found easily by finding the pixels which have a zero level set $\phi(x, y) = 0$.

3.3.8 Atlas-Guided Technique

If a standard atlas or template is available, atlas-guided technique is a powerful tool for medical-image segmentation. An atlas is generated from the anatomy information about the image. Such atlas-guided technique performs the same function as that of classifiers except that they are implemented in the spatial domain of the image rather than in the feature space. The limitation in this technique is that it requires a template, which is not available in many situations [8].

3.3.9 Other Techniques

The Model fitting technique fits a simple geometric shape such as an ellipse or parabola to segment the image. The watershed algorithm uses edge detection and mathematical morphology concepts to segment images into homogeneous regions [8].

Human sight is a very complex system and employs gained knowledge to recognize the image. Experts' knowledge enables them to retrieve more information from the image than a normal person. Experts' knowledge can be formulated and incorporated with any other segmentation techniques in medical images [48, 115–117].

3.4 Summary

Many research papers have been published regarding segmentation field. The goal of this chapter is to examine the most common image segmentation techniques to find the most suitable one to use in our research. In this chapter, several segmentation techniques have been examined, including thresholding, region growing, classification, clustering, Markov random field modelling, artificial neural networks, deformable models, and atlas-guided.

Thresholding is straightforward and yields good results for simple images; however it is not capable of handling ultrasound images. The critical requirement of the region growing technique is to choose noise insensitive properties for each object to correctly segment the image. Due to speckle noise in ultrasound images, the region growing technique usually fails to accurately segment ultrasound images. The segmentation problem is also considered as a classification problem, but this requires training data. Training data is not always available in medical field. Also, anatomical and physiological variability in the training data decreases the accuracy of the results. Moreover, it is difficult to create a large training-dataset in the medical field, especially, by an expert. For these reasons, classification technique is not suitable for the research described in this thesis. Clustering is also considered for image segmentation. Clustering technique does not require training data, a definite advantage over the classification approach. However, the accuracy of clustering techniques is usually less than that of the classification techniques, in particular, with high noisy images such as ultrasound images. The Markov random field model technique is applied for image segmentation, but the selection of the proper parameters to control the spatial interaction, especially with ultrasound images, is challenging. Artificial neural networks (ANNs) are also used in medical image segmentation, but requires a large training-data set which is not available for the research point. Moreover, finding the "right" structure of a neural network is not easy. Deformable models are discussed in more details in this chapter. Deformable models consist of parametric deformable models and geometric deformable models. One of the best parametric deformable models, the *Gradient Vector Flow (GVF)*, is studied. For geometric deformable models, the *active contours without edges* technique is presented. The last is the atlas-guided technique, but it requires a template which is not available in many situations.

In conclusion, It is found that the deformable models approach is superior for medi-

cal image segmentation and is adopted in this thesis. The parametric deformable models technique, which is quite capable of segmenting one object in a noise image, has been successfully used for many semi-automatic techniques for prostate segmentation in ultrasound images. Therefore, one of the superior techniques of the parametric deformable models, *Gradient Vector Flow (GVF)*, is used in the proposed automatic prostate segmentation algorithm discussed in Chapter 4. The geometric deformable models can easily handle the topology changes by splitting and merging the contours, a big advantage over the parametric models. Since it is required to segment unknown number of regions in the regions of interest (ROI) part, a geometric deformable model is used. Since some of the suspicious regions, required to be segmented, do not have clear edges, the *active contours without edges* technique is used in the proposed ROI segmentation algorithm discussed in Chapter 5.

Chapter 4

Prostate Segmentation

4.1 Introduction

TRUS imaging has been pivotal in the decrease in the death rate from prostate cancer (Pca) [2, 5]. TRUS enables needle biopsies to be accurately and safely performed, some cancers to be detected, and the prostate volume to be measured with reasonable accuracy. Images are obtained by inserting an ultrasound transducer into the rectum in a manner that allows the imaging transducer to be close to the posterior wall of the prostate. Ultrasound waves are then generated to cross the prostate and its surrounding tissue. A varying percentage of these waves are reflected back from different tissue interfaces. These waves are collected by the transducer and transformed into electrical signals that are displayed as an image on a monitor. Sonography professionals mentally segment these images to detect the edges of the prostate and different tissue textures within the prostate that might represent prostate cancer.

Manual segmentation consumes considerable time and effort. Besides, manual segmentation is not only operator-dependent, but also a tedious and repetitious. In this research, a new multi-stage computer algorithm is introduced for segmenting and extracting the prostate image by using knowledge-based rules. The proposed algorithm is fully automatic and implements experts knowledge. The experimental results confirm that the proposed algorithm is appropriate for efficiently extracting the prostate image from TRUS image. The newly developed algorithm is operator-independent, and supports the segmentation

of the prostate gland of any shape and orientation.

4.2 Related Work

Over the last few years, the prostate segmentation problem has received considerable attention [118–135]. The algorithms in the literature are categorized as semiautomatic and automatic segmentation.

4.2.1 Semiautomatic Prostate Segmentation

Most techniques depend on a human initialization [118–129], which in turn, leads to operator-dependent results. A small number of research papers have reported on prostate segmentation with 3D ultrasound images [118–120]. As a transition from 2D to 3D images segmentation, Wang et al. [121] have segmented 3D images by using 2D ultrasound images. Most semiautomatic prostate segmentation algorithms use 2D ultrasound images [122–129]. A number of them rely on deformable models for prostate segmentation [118–125].

Hu et al. [118, 119] have suggested an algorithm to segment the prostate from 3D ultrasound images by using dynamic surface. This algorithm needs a manual initialization by six points. The initial points should be close to the boundary of the prostate to prevent the contour from attracted to false edges. Some results of this algorithm must be edited and re-deformed a number of times to reach the final result.

Ghanei et al. [120] have developed a prostate segmentation algorithm in 3D ultrasound images with deformable surfaces. Forty percent to 70% of the slices of the 3D ultrasound image need to be initialized by employing four to five points per slice. After the algorithm creates the initial surface from these initial contours, the initial surface deforms under the internal and external forces to reach the final surface.

Wang et al. [121] have devised an algorithm to segment the prostate from 3D images by using 2D slices. The algorithm needs four initial points to be identified manually on the boundary of a selected slice. Next, the algorithm creates an initial contour from the manually identified points. The contour is then deformed under internal and external forces. After the boundary of the prostate is found in the selected slice, the algorithm iteratively propagates the resulting boundary to the adjacent slices. The segmentation

process needs to be paused from time to time to manually edit the contours, which requires much human interaction.

A 2D prostate segmentation algorithm is introduced by Ladak et al. [122] who have employed a Discrete Dynamic Contour (DDC). This algorithm requires four initial points which should represent the prostate shape and be close to the prostate boundary. Also, the first and the third initial points should be positioned approximately on the axis of symmetry. Even with a good initialization, the results of some images need to be edited by moving the vertices which are distant from the boundary to the prostate boundary. The authors have classified the ultrasound images into three categories: easy, moderate, and difficult. For the easy images, no editing is required. Moderate images need to be edited and re-deformed once, whereas the difficult images are required to be edited and re-deformed at least two times. Hence, this algorithm requires a great deal of manual interaction and produces operator-dependent results.

Applying the dyadic wavelet transform and deformable contour, Chiu et al. [123, 124] have developed another semi-automatic method. Four initial points are required, and they should be adjacent to the prostate boundary to prevent the contour from being attracted to false edges due to noise, which leads to operator-dependent results.

Jendoubi et al. [125] have used balloon and GVF deformable contours. Their results are promising, but not accurate, because only a median filter is chosen for enhancing the ultrasound images. Although the median is powerful, it cannot filter out ultrasound image noise. Furthermore, no evaluation is provided to judge the accuracy of this algorithm.

Employing deformable superellipses, Gong et al. [126] have offered a semiautomatic technique for prostate segmentation. The algorithm uses fixed length sticks (15 pixels) to enhance the contrast of the ultrasound images. This technique requires more than two points to determine the scale of the prostate gland. Moreover, the authors have used a large number of manual outlining images as a training set to find the optimal parameters and their distribution. This training data represents most of their data. In addition, the usage of manual segmented images for training makes the results biased to the training data. Since prostate images have many different shapes, it is challenging to find a single mean shape which represents the variability of the prostate shapes.

Another semiautomatic algorithm has been presented by Pathak et al. [127]. It consists

of a weak membrane filter, fixed sticks technique, and basic knowledge to segment the prostate from the ultrasound images. Since the seed point is identified manually, the algorithm is operator-dependant. Also, the selected seed point must be in the mid-gland region of the image. This is essential because the edges which are more than two standard deviations distant from the seed point are removed. Furthermore, this algorithm uses a stick technique with fixed length, 15 pixels, to enhance the image. In this chapter, cascading sticks with lengths ranging from 3 pixels to 17 pixels substantially enhance the image much more than the fixed length proposed in this paper.

Abolmaesumi et al. [128] have reported a semi-automatic algorithm, based on the Interacting Multiple Model (IMM) estimator, along with a Probabilistic Data Association Filter (PDAF). They have used a fixed length sticks filter with 15 pixels in length, to enhance the ultrasound images as a preprocessing stage. Their algorithm requires a seed point inside the prostate to be identified manually. However, their algorithm exhibits some limitations. All the cavity boundary points should be observed from a point inside the cavity to prevent the algorithm from segmenting some practical prostate shapes. Also, this algorithm is very sensitive to the location of the seed point; In fact, any small shift of the seed point location changes the resulting contour. Since, no evaluation exists for this algorithm, it is difficult to determine its accuracy.

Adopting morphologic operators and fuzzy membership functions, Sahba et al. [129] have presented a semiautomatic algorithm for prostate segmentation. The algorithm depends on a minimum level of user interaction by manually identifying some parameters; however, the authors have acknowledged that their technique has introduced many parameters that need to be adjusted.

4.2.2 Automatic Prostate Segmentation

Some researchers have proposed automatic algorithms[130–135] for prostate segmentation in 2D ultrasound images. To avoid manual initialization, manual segmented images are used as a training set to produce the initial shape of the prostate [130–132]. However, this technique has a severe drawback. Since the prostate glands have diverse shapes, the initialization does not work for many images. Moreover, the use of manual segmented images in the training can lead to biased results.

Shen et al. [130] have used the previously mentioned initialization, but acknowledged that such initializations is not possible with different prostate shapes. The authors have used Gabor filter features to segment the prostate gland. The evaluation of this algorithm is calculated for only eight images, which is not good enough to prove the stability of the algorithm.

Betrouni et al. [131] have used 25 out of 30 images as a training set to generate the average shape. In [132], the authors have used 35 images as a training set. Then, they have tested the algorithm with 10 images, 4 of which were used in the training set. The average shape in both papers has a similar shape as the test prostate images.

Another technique for solving the automatically initialization problem is edge detection [133]. To find an initial open contour, Nanayakkara et al. [133] have applied the Canny edge detector. Then, the final contour is found by the discrete dynamic contour, but no evaluation exists.

Richard et al. [134] have employed clustering technique and the texture features, but no evaluation is provided for this technique and the resulting image is not that accurate.

Chiu [135] has used a special initialization method with many thresholding and user-defined parameters, which is not suitable to many practical images. He has evaluated his algorithm with eight images, which is not enough to validate this method.

4.2.3 Analysis of the Existing Algorithms and Research Goals

From the previous survey, the following is noted.

1. Most algorithms for prostate segmentation are semiautomatic [118–129] and require human interaction and produce operator-dependent results. Semiautomatic algorithms are sensitive to manual initialization. Some require more than two initial points [118–126] close to the prostate boundary to prevent the contour from being attracted to false edges due to noise. Other semiautomatic algorithms [127–129] require only one seed point. It is essential for [127] the algorithm to pick the seed point in the mid-gland region. Algorithm [128] is also very sensitive to the location of the seed point, and any small shift in the seed point location changes the resulting contour.

2. Most prostate segmentation algorithms use 2D ultrasound images [122–135], rather than 3D images [118–120]; in fact, the segmentation of the 3D image can be achieved by segmenting the corresponding 2D slices [121].
3. Most algorithms have adopted deformable models [118–125, 133, 135] which exhibit the superiority of this technique over other techniques.
4. Some semiautomatic algorithms require manual editing during the segmentation process [118–122], which implies more effort, more time, and operator-dependent results.
5. For most automatic algorithms manual segmented images are adopted as a training data [130–132] which is not suitable for prostate segmentation for the following reasons. First, due to the variability of prostate gland shapes, it is hard to find a single mean shape which represents all the variability of the prostate shapes. As a result, if the mean shape is not very close to the prostate boundary of the test image, the contour is attracted to false edges due to the noise. Secondly, the training set leads to operator-dependent results. Thirdly, it is hard to create a large training data set in the medical field, especially if it is created by an expert.
6. Using most of the data set as a training data [126, 131, 132] makes the results of the algorithm biased to the training data.

To overcome the limitations of the existing algorithms, some goals require to be achieved.

1. The proposed algorithm requires to be automatic.
 - (a) It should be operator-independent. It should not require any initial points to be defined by an operator or any further manual editing. By doing so, the algorithm can process hundreds of images, saving effort and time for the expert.
 - (b) It should not require any training data to overcome the following limitations.
 - i. It is quite difficult to determine a single mean shape which represents the large variability of the prostate shape
 - ii. Using most of the data set for training may generate biased results, especially, for small data sets.

- iii. It is difficult to create a large training-data set in the medical field ,especially, if it is created by an expert
2. It should be accurate.
3. It should be capable of segmenting various prostate shapes. Therefore, any preset prostate shape should not be assumed.

The proposed prostate segmentation algorithm is developed and described in Section 4.3. The proposed algorithm has achieved the required goals.

4.3 Algorithm Description

To automatically segment and extract the prostate from the ultrasound images, a multi-stage segmentation algorithm is proposed in this chapter. It consists of the five stages as illustrated in Figure 4.1.

1. Building the knowledge-based rules
2. Enhancing the image
3. Generating the seed point
4. Detecting the prostate edge
5. Extracting the prostate image

Building the knowledge-based rules is the first stage of the proposed prostate segmentation algorithm. Two radiologists are asked about the knowledge-based rules that they apply to segment the prostate from the ultrasound images. These rules are summarized in the next section. These rules are integrated in the algorithm as displayed in Figure 4.1.

In the second stage, the proposed algorithm enhances the quality of the image. The enhancement is achieved in two steps: the proposed sequential sticks and a Gaussian filter. Also, a comparison is conducted between the regular sticks and the proposed sequential sticks technique to prove the significantly enhancement, gained by using sequential sticks.

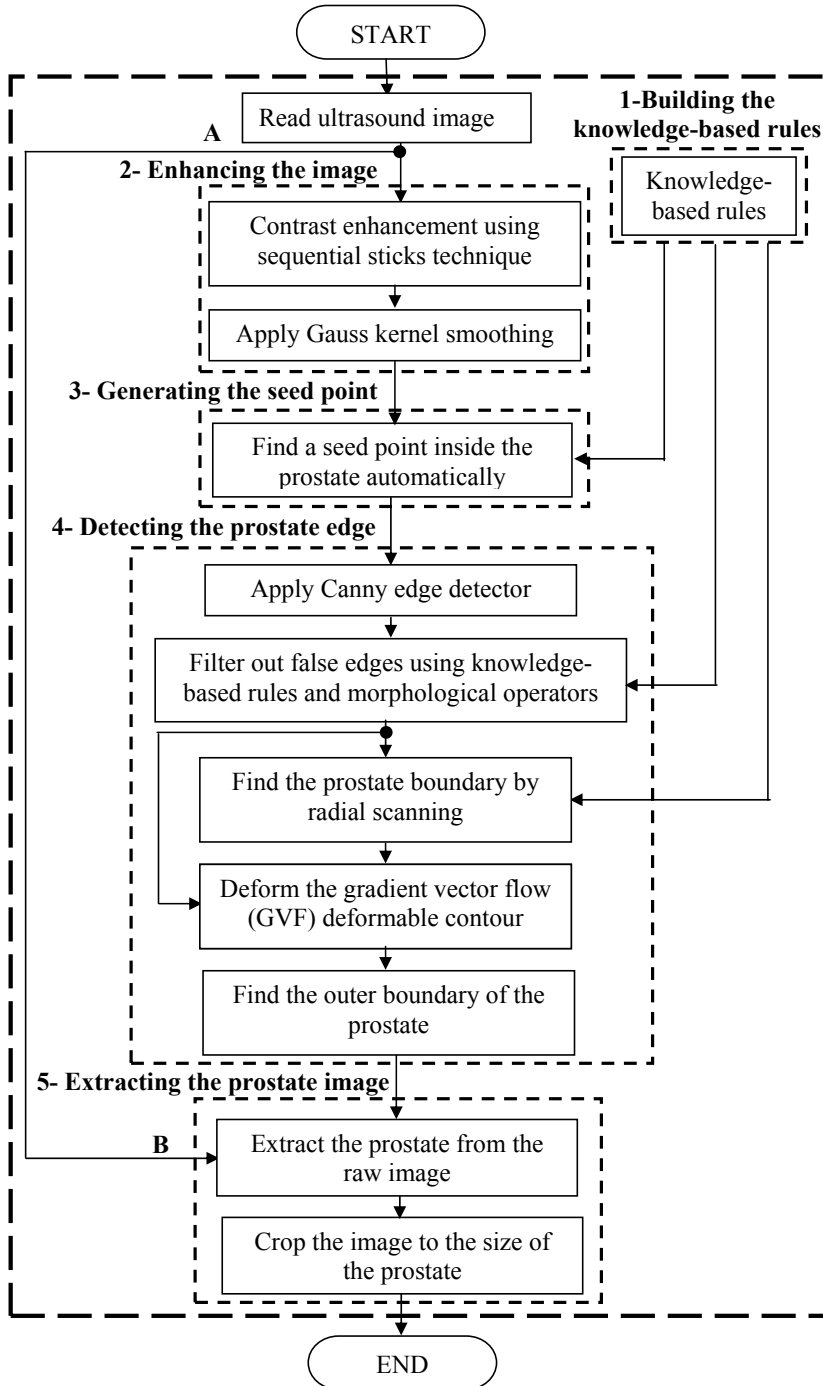


Figure 4.1: Prostate segmentation flow chart

In the third stage, the seed point is identified automatically by the algorithm by using the generated knowledge-based rules. The algorithm is neither sensitive to the position of the seed point inside the prostate nor to the shape of the prostate gland.

Prostate edge detection is the fourth stage in the proposed algorithm. This stage is the principal part of the algorithm and consists of five steps. The goal of the first step is to find a preliminary edge map by a Canny edge detector. Since these edges contain some false edges, they are removed in the second step by applying knowledge-based rules and morphologic operators. In the third step, the algorithm scans the image from the seed point in the radial direction to remove other false edges, to interpolate the missing parts, and to find the initial boundary of the prostate. In the fourth step, the initial boundary is then deformed by using the GVF deformable model to find the prostate's boundary. Since experts always tend to find the outer boundary for the prostate, the inner boundary, found by the previous steps, is expanded by applying a small shift in the last step.

Some results of the algorithm are presented for visual inspection, and evaluated by comparing the new algorithm results with the manual segmentation ones by distance-based and area-based metrics. The results of the evaluation are then compared with the results of the two other algorithms to exhibit the superiority of the proposed algorithm.

4.3.1 Building the Knowledge-Based Rules

The knowledge-based rules for segmenting the prostate from ultrasound images are collected from two medical radiologists from the University of Western Ontario and Grand River Hospital in Kitchener. These rules are summarized by the following five rules which are applied to the proposed algorithm.

1. TRUS images consist of three different regions: the prostate, the tissues around the prostate, and the background.
2. The background of the image is black.
3. The grey level of the prostate is low in respect to the tissues surrounding it.
4. The prostate is not in the periphery of the image, nor necessarily in the middle.
5. The prostate has a smooth curvature shape.

4.3.2 Enhancing the Image

Speckle noise renders the segmentation of ultrasound images challenging. The goal of the pre-processing stage is to eliminate the speckle noise and enhance the edges. First, the contrast of the image is enhanced by using the proposed sequential sticks technique. Secondly, the noise is further reduced by applying a Gaussian filter. These two steps are discussed in more detail in the next two subsections.

4.3.2.1 Sequential Sticks Technique

Most image enhancement techniques blur the edge information in order to filter out the noise in the images. The sticks technique is one of the powerful techniques for removing speckle noise, and at the same time, improving the edges. The sticks technique detects whether a line is passing through each pixel, which is related to line detection techniques. The main idea behind this technique is to apply a set of templates as a filter bank and find the largest filter output at each pixel. For the $N \times N$ neighbourhood in the image, there are $2N - 2$ short lines that pass through the central pixel with N pixels in length. The sum of the pixel values along each line segment is calculated. The largest sum of the segments is put in the centre pixel of $N \times N$ sub-matrix in the image. This step is repeated for the entire image [136, 137]. Then, the intensity level of the image is readjusted to the original level. Figure 4.2 illustrates different sticks whose length is five pixels. Czerwinski et al. [137] have studied the effect of stick length and thickness. They have found that increasing stick length remove more speckle noise, while blurring the details of the tightly curving edges. They have also found that increasing stick thickness enhances the broad edges, while blurring the thin edges. For more information about this technique, the reader can consult the literature [136, 137].

In this research, one pixel stick thickness is adopted to avoid losing any of the thing edges. Some researchers [126–128] have used the sticks technique with a length of 15 pixels to enhance ultrasound images. By conducting some experiments with 50 images, it is found that applying sequential sticks with lengths varying from 3 pixels to 17 pixels, an increment of two improves the details of the tightly curving edges and decreases the speckle noise much better than the fixed sticks technique. Figure 4.3 illustrates the effect of changing a stick length. It shows that increasing the stick length reduces more speckle

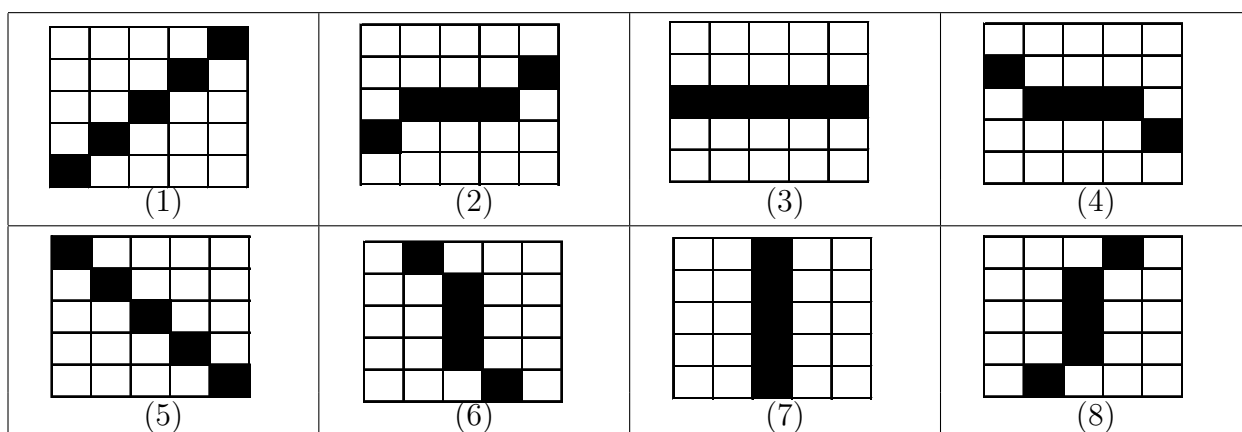


Figure 4.2: Different sticks five pixels in length

noise. Figure 4.3 shows also the dramatical enhancement gained by applying the proposed sequential sticks over the fixed length sticks. The procedure of the proposed sequential sticks technique is as follows. The sticks technique is applied with a length of 3 pixels to enhance the details of the tightly curving edges. Next, the output image from this process is used as an input image to the next sticks which are 5 pixels in length. The output from this is used as an input to the next size of sticks and so on. Sticks with odd lengths between 3 and 17 pixels are used. A small enhancement of the image is gained by increasing the size of the sticks to more than 17 pixels. Further improvement does not justify the processing time. To demonstrate the improvement gained by applying the sequential sticks over the fixed sticks, the edge map is generated twice, as depicted in Figure 4.4. The first edge map is obtained by enhancing the image by using fixed sticks with a length of 15 pixels [126–128], whereas the other one is generated after applying a sequential sticks technique with lengths from 3 pixels to 17 pixels with an increment of 2 pixels.

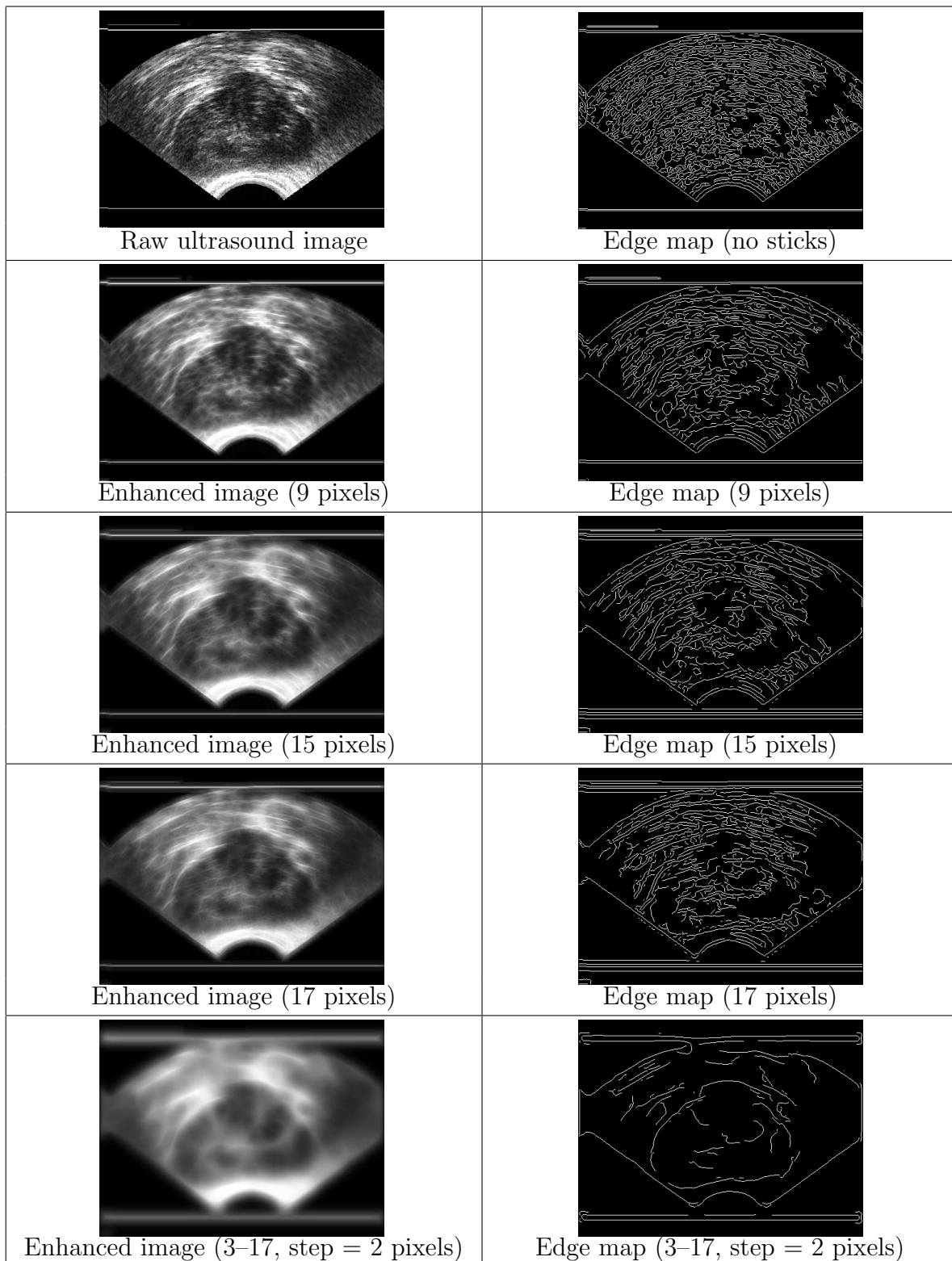


Figure 4.3: Effect of changing stick length

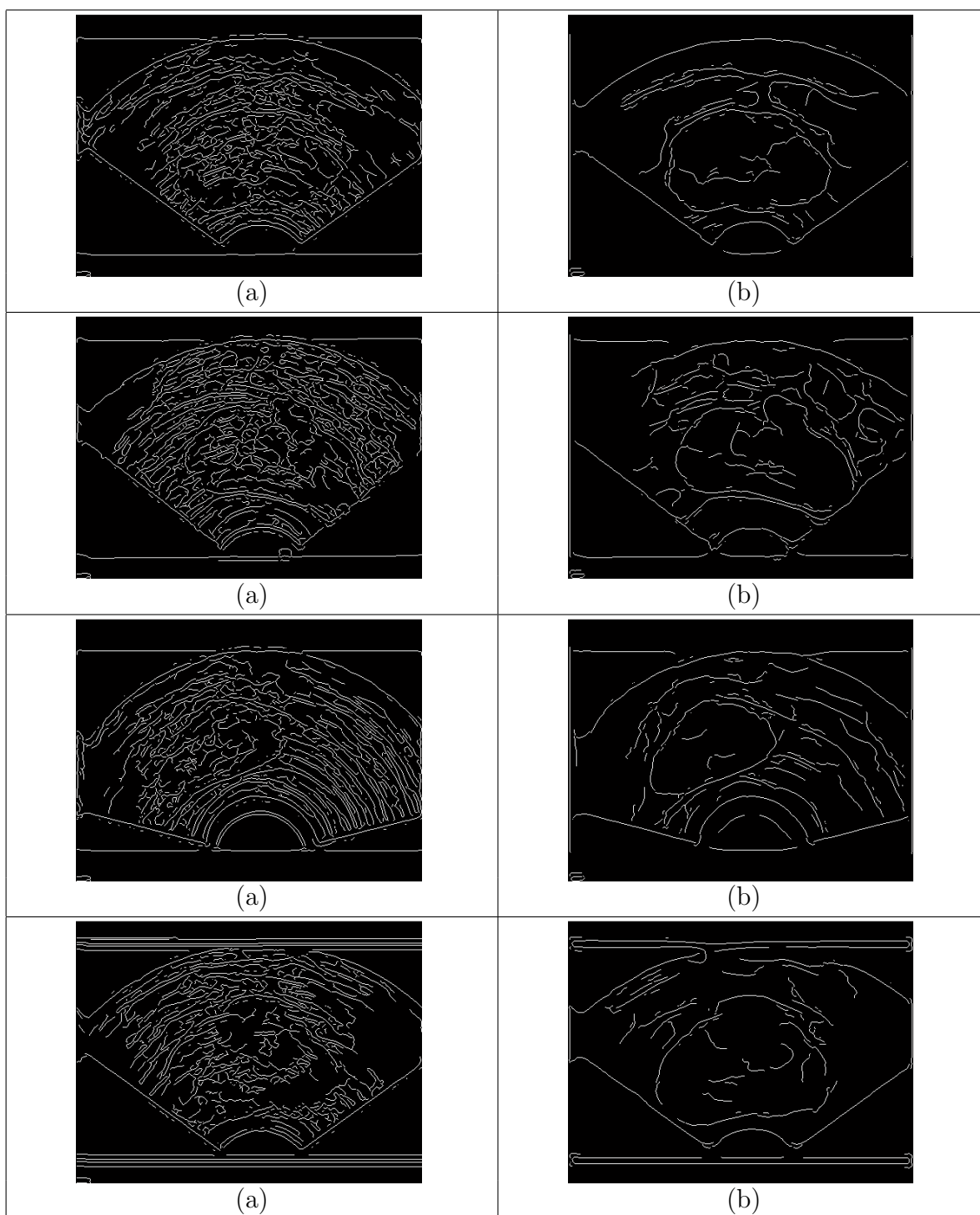


Figure 4.4: Comparison between fixed and sequential sticks. The edge map after applying (a) fixed sticks with 15 pixels in length and (b) sequential sticks with lengths from 3 to 17 with an increment of 2 pixels

4.3.2.2 Gaussian Filter

The goal of the second step of the image enhancement is to further reduce the noise to improve the edge map by applying a 20 x 20 Gaussian kernel, where $\sigma = 5$.

4.3.3 Generating the Seed Point

In order to automate the segmentation process, the proposed algorithm require to locate a seed point in the prostate. The proposed algorithm uses this seed point to filter out the false edges as described in Section 4.3.4.2 and find the initial boundary of the prostate as described in Section 4.3.4.3. The proposed algorithm does not require the seed point to be in the centre of the prostate. Hence, it is not difficult to find a seed point in the prostate. This is achieved by using knowledge-based rules (rule 1 to rule 4), described in Section 4.3.1. The input of this stage is an ultrasound image and the outputs are the x and y coordinates of the seed point. To identify a point inside the prostate gland, the algorithm should look for the low intensity pixels because the grey levels of most of the pixels in the prostate are darker than those surrounding the tissues, rule 3. Because ultrasound manufacturers have arbitrarily designated the background of the ultrasound images as black, rule 2, a factor that affects the algorithm results, the algorithm replaces the background of the image with a white colour before searching for the low intensity pixels. The prostate gland is not in the periphery of the image as stated in rule 4; therefore, the first and the last third of the rows, and the first and the last quarter of the columns, are excluded from the seed point calculations. Even though the excluded parts might include part of the prostate, this operation increases the stability of the seed point localization by eliminating the shadowing and focusing on the part of the image which contains most of the prostate gland. Primarily, the algorithm sorts the rest of the pixels in the image according to their intensities. The number of low intensity pixels that is considered for the seed point localization is defined as ns . The ratio between these ns pixels and the total number of pixels, which are considered in the seed point calculations, is defined as P . For different image sizes, the algorithm picks the same ratio P of pixels to calculate the median coordinates of these pixels and assigns this median to the seed point. The algorithm is not sensitive to the value of P . Nevertheless, some guidelines are proposed for the selection of this value. If the value of

P is high, close to 1, some of the high intensity pixels are considered in the seed point evaluation which can affect the result. However, if the value of P is small, close to 0, the result may be affected by the noise. The reason for choosing the median instead of the mean in the seed point evaluation is to render this stage more robust against noise. This technique is tested by selecting different values of P for 50 TRUS images, where the prostate glands are at different positions in the image, and exhibit different shapes. It is found that the P value should be in the range of (0.2: 0.8) to yield a seed point inside the prostate. A value of 0.5 representing P is adopted.

4.3.4 Detecting the Prostate Edge

At this crucial stage, the algorithm employs the enhanced image, the seed point, and knowledge-based rules to find the prostate boundary. This stage consists of five steps.

1. Applying Canny edge detection
2. Eliminating the false edges
3. Finding the initial prostate boundary
4. Applying the GVF deformable model
5. Finding the outer boundary of the prostate

The details are described in the following subsections.

4.3.4.1 Applying Canny edge detection

In this stage, a preliminary edge map is obtained by using the Canny edge detector to find the weak edges, even if more false edges are generated, because they are removed later by using knowledge-based rules and morphological operators.

4.3.4.2 Eliminating the False Edges

The newly developed algorithm adopts the gained knowledge to recognize images. By using rule 3, described in Section 4.3.1 which states, *The grey level of the prostate is low in*

respect to the tissues surrounding it, most of the false edges are eliminated by scanning the image in a radial direction from the seed point, and removing any false edge that represents a light to dark transition. This step is similar to the method in the literature [127]. The previous step removes most of the false edges and breaks the rest of the false edges into short segments. To filter out these short segments, a morphological opening is applied to remove all the linked pixels with areas less than 50 pixels.

4.3.4.3 Initial Boundary Detection by Radial Scanning

In this stage, the edge map is scanned from the seed point in a radial direction to find the initial boundary of the prostate. Also it is assumed that there are still some false edges in the edge map that have to be eliminated. To achieve this, the algorithm requires rule 5, described in Section 4.3.1, which states *The prostate has a smooth curvature shape*. The algorithm calculates the distance between each edge pixel and the seed point. Because the boundary of the prostate is smooth, this distance should change gradually. Therefore, any sudden change in the radial distance indicates a false edge pixel and it is eliminated. Then, the algorithm uses interpolation to find any missing parts of the contour and consequently, obtains the complete smooth prostate boundary which is considered as the initial contour for the next step.

4.3.4.4 Gradient Vector Flow (GVF) Deformable Contour

The boundary detected in Section 4.3.4.3 is considered as an initialization for the GVF deformable contour, described in Section 3.3.7.1.1. The only modification here is that the filtered edge map, which is generated in Section 4.3.4.2 is employed instead of generating the edge map by a gradient operator. The parameters used in the contour are as follow. Elasticity, $\alpha = 0.25$; the rigidity, $\beta = 0.0$; and the GVF regularization coefficient, $\mu = 0.2$. At each deformation step, the contour is reparameterized to maintain a 5 pixels distance between each successive vertices.

4.3.4.5 Find the Outer Boundary of the Prostate

Experts tend to find the outer boundary of the prostate. Therefore, the inner boundary, found through the previous steps, requires to be expanded by a fixed value. This step is similar to another in the literature [127]. Although the fixed value which is used by Pathak et al. is 20 pixels, in this thesis, expanding the boundary by only 3 pixels is all that is required to attain the outer boundary of the prostate. To prove that this fixed value is good enough to find the outer boundary, the average mean difference MD is calculated for 50 images. It is found that the average MD value is approximately equal to zero which means that the algorithm boundary is exactly on the outer boundary.

4.3.5 Extracting the Prostate Image

This is the final stage of the algorithm. It consists of two steps. The first one is to extract the prostate from the raw ultrasound image by using the prostate boundary found in the previous stage. The second step is to crop the image to the size of the prostate to mitigate the computation time and storage space of the ROI algorithm, described in the Chapter 5.

4.3.5.1 Extracting the Prostate Image

The algorithm, at this stage, extracts the prostate from the image by using the detected boundary and the ultrasound raw image. It is note worth that the prostate segmentation part, the focus of this chapter, is a part of the proposed complete algorithm for prostate cancer diagnoses. It is also noteworthy that the complete diagnosis proposed algorithm is divided into parts to decrease the complexity of the problem. To design each part separately, any side effects of the different parts should be prevented. For instance, the scope of this chapter is the segmentation and extraction of the prostate image, whereas the scope in the next chapter is to find the regions inside the prostate which are more likely to exhibit cancer. Each of these two parts involves a different image enhancement technique. Moreover, image enhancement used in the first part does not affect that in the second part. In other words, the *side effects* of the two parts are prevented. The only connection between the two parts is a clearly defined set of input and output. For instance, the input of the first part, prostate segmentation part, is the raw ultrasound image. The output of

the prostate segmentation is the raw prostate image. It is important to emphasize that the raw image is used instead of the processed image, as indicated by line A-B in Figure 4.1, to avoid any side effects of the image enhancement that might affect the diagnosing algorithm at a later stage.

4.3.5.2 Cropping the Image

This is the final stage of the algorithm. Here, the ultrasound image is cropped to the size of the prostate. This stage is required for the next part of the prostate cancer-diagnosing algorithm, the Regions of Interest ROI segmentation. Since the goal is to diagnose cancer inside the prostate, the rest of the image is discarded. Therefore, cropping the image to the size of the prostate saves computational time and storage space during the classification of the cancerous regions in the image.

4.4 Results

The proposed segmentation algorithm is applied to 50 ultrasound images with various prostate shapes. The algorithm detects the boundary of the prostate, successfully, in all 50 images. Matlab 6.1 is used to implement the algorithm with an average execution time of about 3 minutes, running on a 1.3 GHz computer, to automatically detect the boundary of the prostate. The key point that makes the algorithm fully automatic is finding the initial contour, as described in the next subsection.

4.4.1 Initial Contour

The principal problem in many prostate segmentation algorithms is how to find the initial contour. As discussed in Section 4.2, some research papers use a manual initial contour to guarantee that the initial contour is close to the prostate boundary. Other papers describe the use of manual segmented images to find an initial contour of the prostate gland, which does not work with some images due to the diversity of the prostate shapes. The characteristics of the proposed initial contour are as follow:

1. The proposed initial contour is found automatically.

2. The proposed initial contour is very close to the prostate boundary.
3. The technique for finding the initial contour is able to handle the diversity of the prostate shapes.

Figure 4.5, Figure 4.6, and Figure 4.7 offer some results of the initial contour part of the algorithm. Since the slices of the same prostate have similar shapes and produce similar results, different prostate shapes are examined.

In each figure, the raw TRUS images are shown in row (a); the locations of the seed points are shown on the raw images as small white solid circles. The results of the image enhancement stage are shown in row (b), whereas row (c) shows the edge map images resulted from applying the Canny edge detector on the enhanced version of the TRUS images. The edge map images contain the prostate boundary, as well as other false edges. Most of the false edges are removed by applying the knowledge-based rules and morphological operators, as shown in row (d). Then, the initial boundary of the prostate is detected by radial scanning, as shown in row (e), which is considered as the initialization of the GVF dynamic contour.

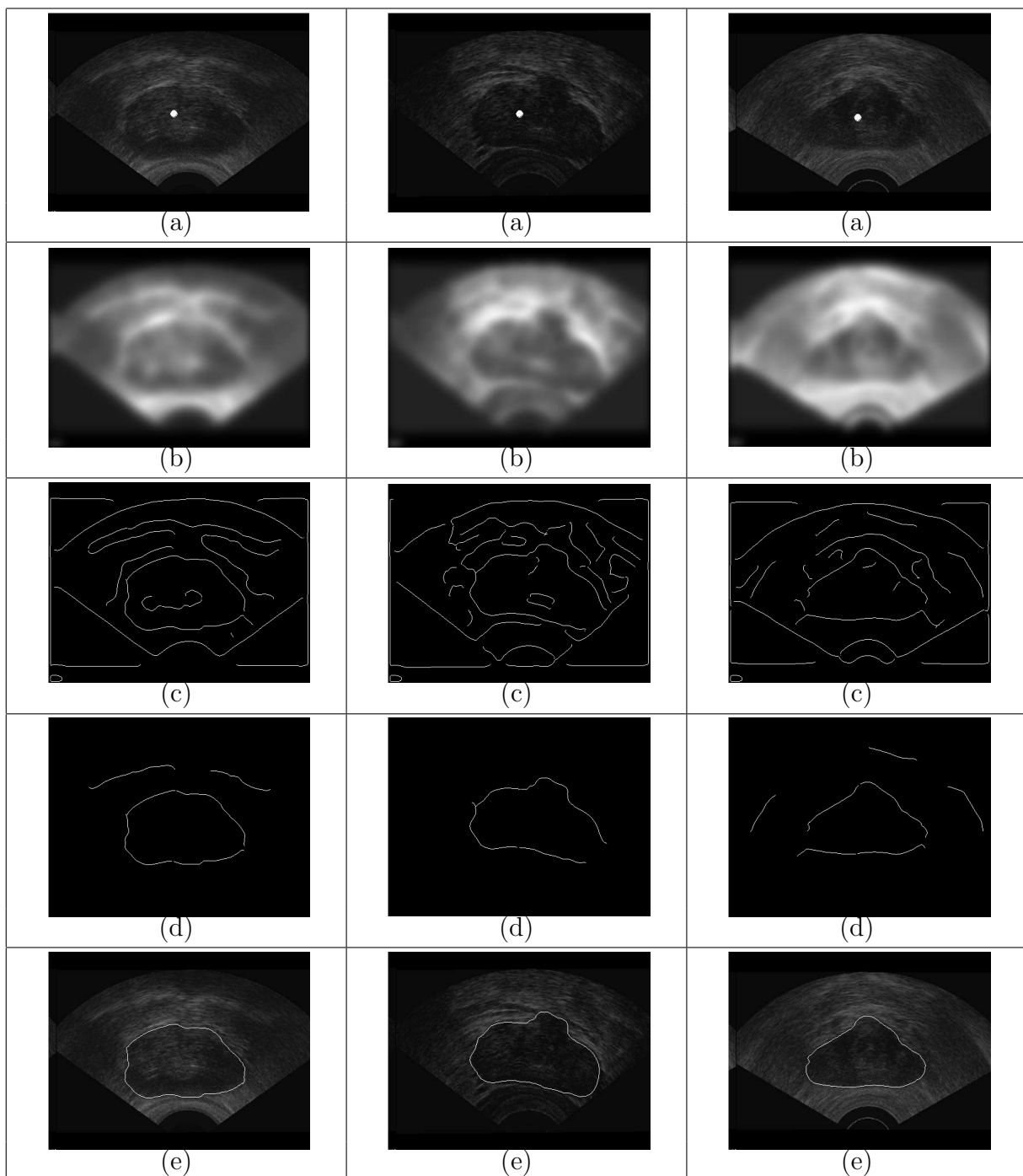


Figure 4.5: (a) The original image with the location of the seed point, (b) image after image enhancement, (c) edge detection by Canny, (d) knowledge-based and morphological opening, and (e) prostate initial boundary superimposed on the image

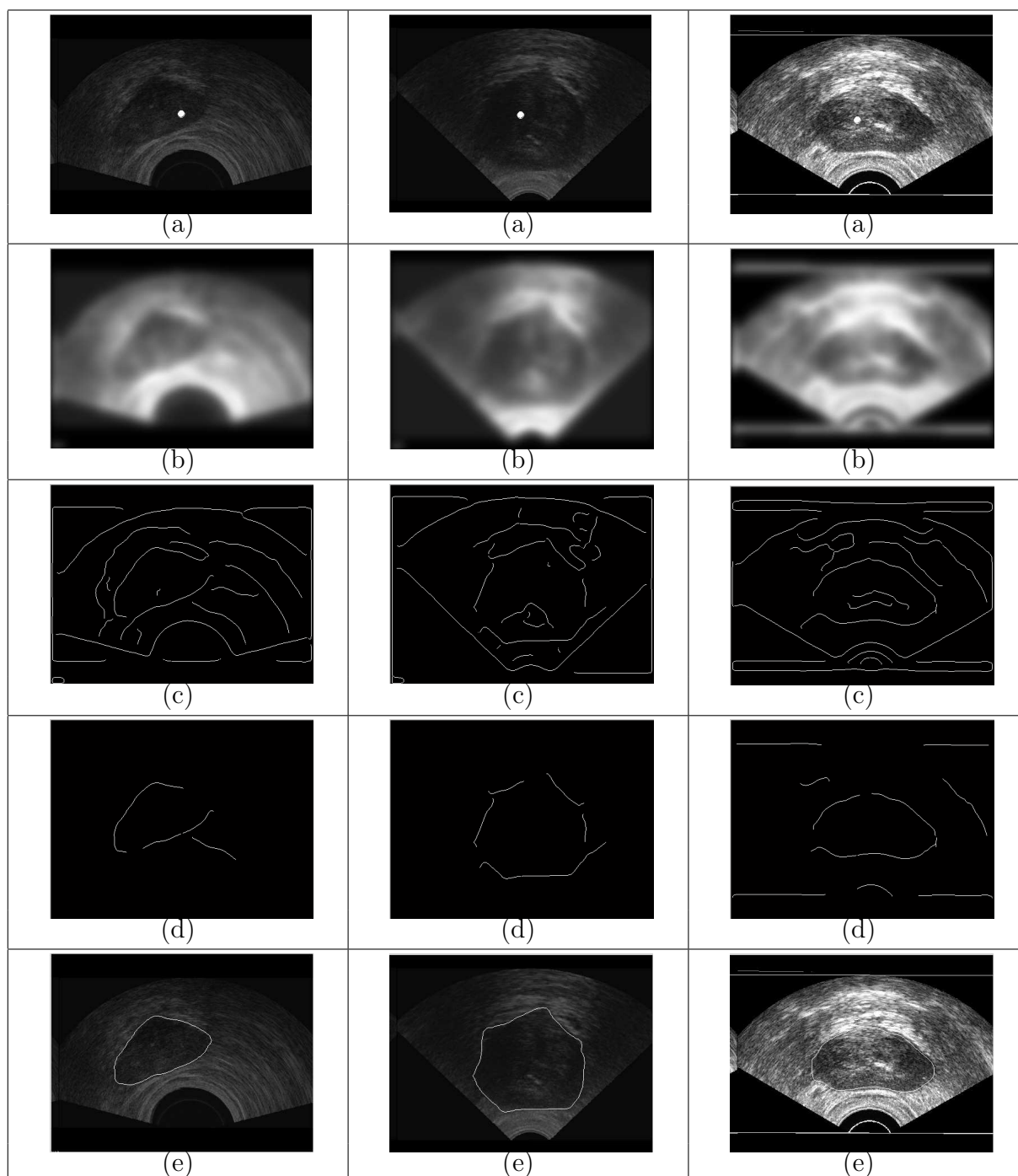


Figure 4.6: (a) The original image with the location of the seed point, (b) image after image enhancement, (c) edge detection by Canny, (d) knowledge-based and morphological opening, and (e) prostate initial boundary superimposed on the image

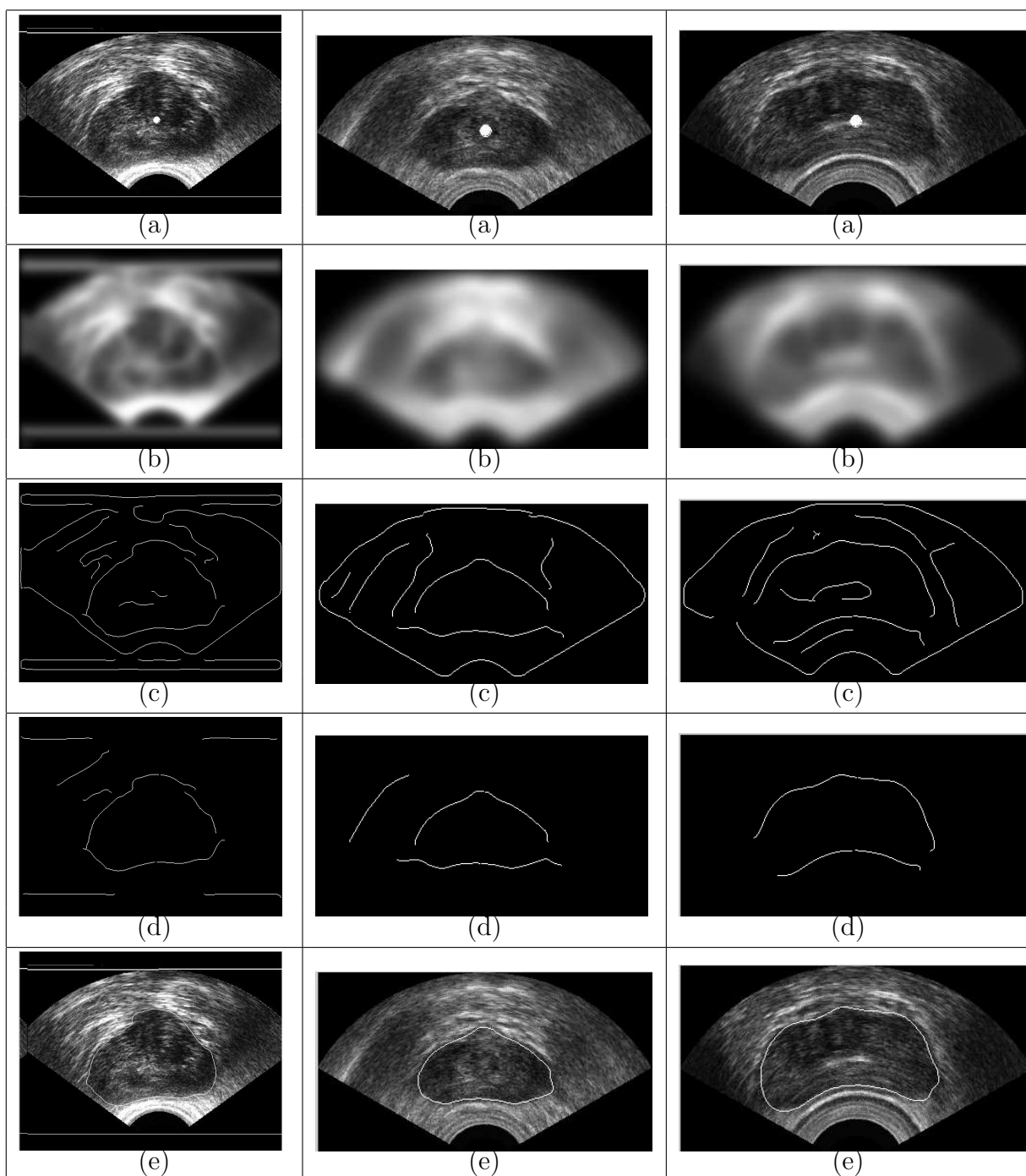


Figure 4.7: (a) The original image with the location of the seed point, (b) image after image enhancement, (c) edge detection by Canny, (d) knowledge-based and morphological opening, and (e) prostate initial boundary superimposed on the image

4.4.2 Final Contour

For the visual inspection of the results of the proposed prostate segmentation algorithm, Figure 4.8, Figure 4.9, and Figure 4.10 summarize final contours of the proposed algorithm versus the manual outline. The results of the novel algorithm is fully automatic and do not need any further editing as required in the literature [122]. From these figures, it is clear that the proposed algorithm results are very close to the manual contours. A detailed evaluation of the proposed algorithm results is discussed in the next section. It is worth noting that the algorithm code is not optimized from the execution time perspective. Thus, the computational time can be decreased significantly by avoiding the unnecessary loops (loops consume considerable time in Matlab). The calculation time can be further decreased by coding the loops in MEX-files. In this way, the execution of the loops are much quicker. Moreover, the execution time can be drastically decreased by implementing the algorithm in C language.

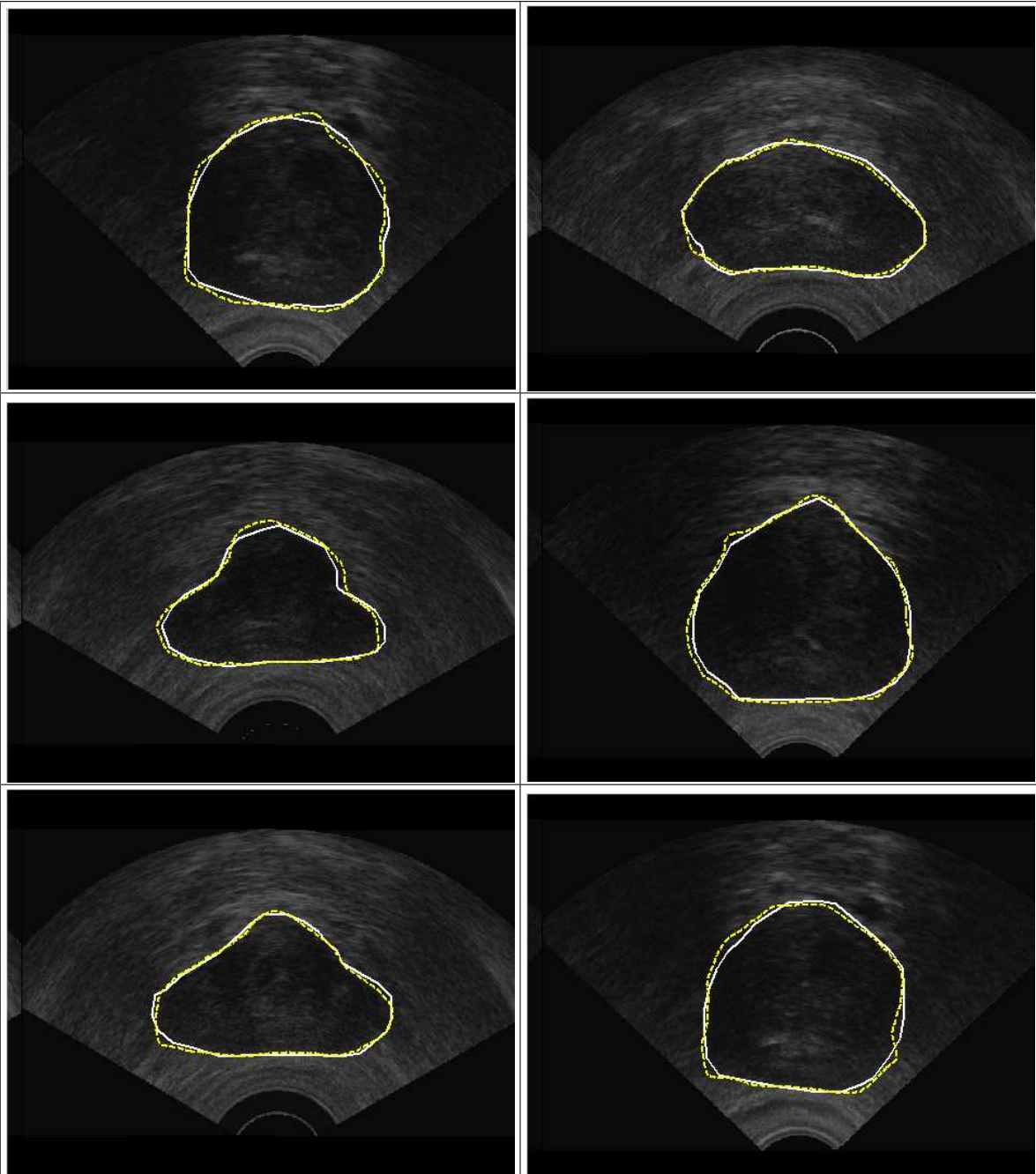


Figure 4.8: Proposed automatic segmentation (dash line) versus manual segmentation (solid line)

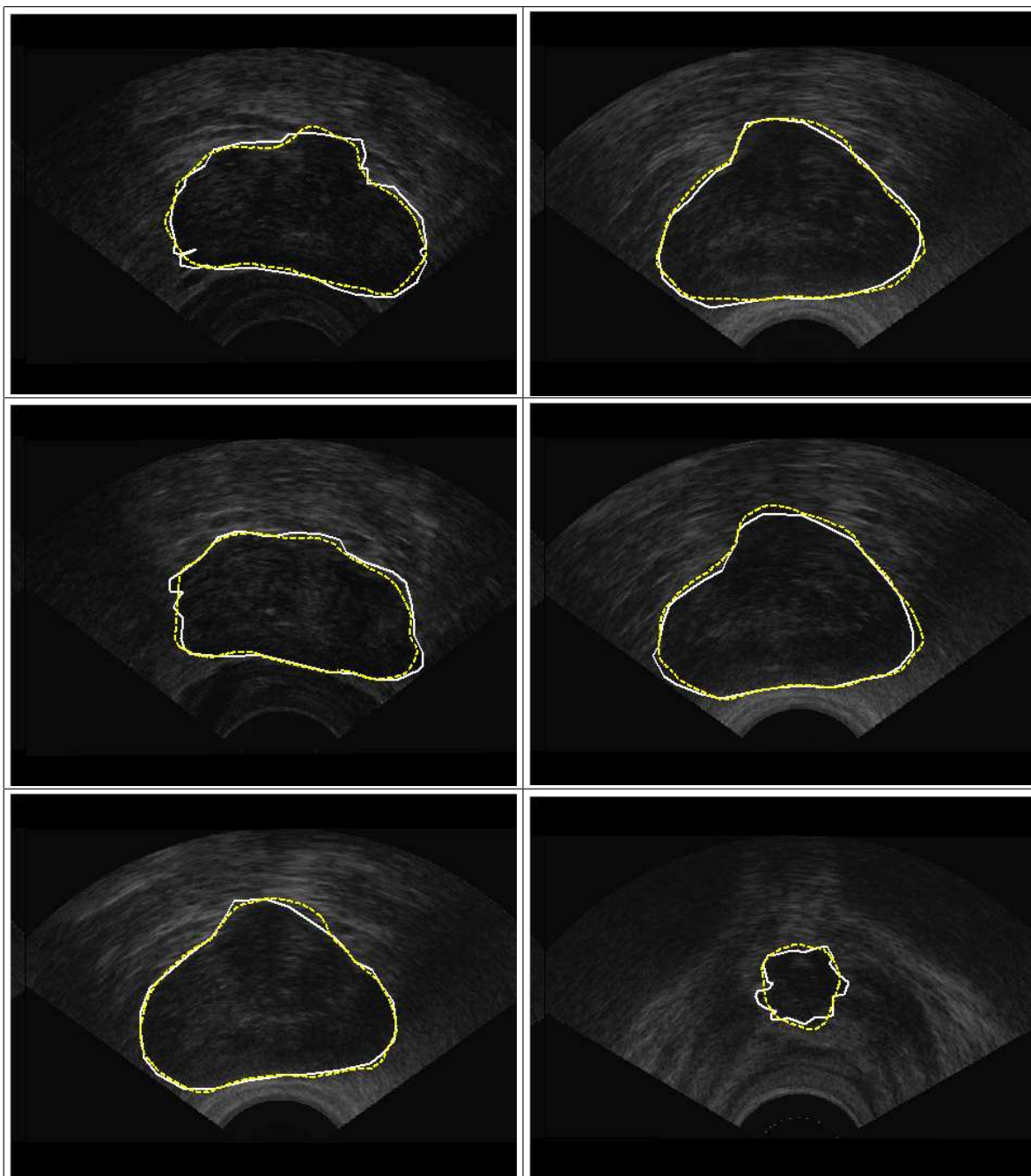


Figure 4.9: Proposed automatic segmentation (dash line) versus manual segmentation (solid line)

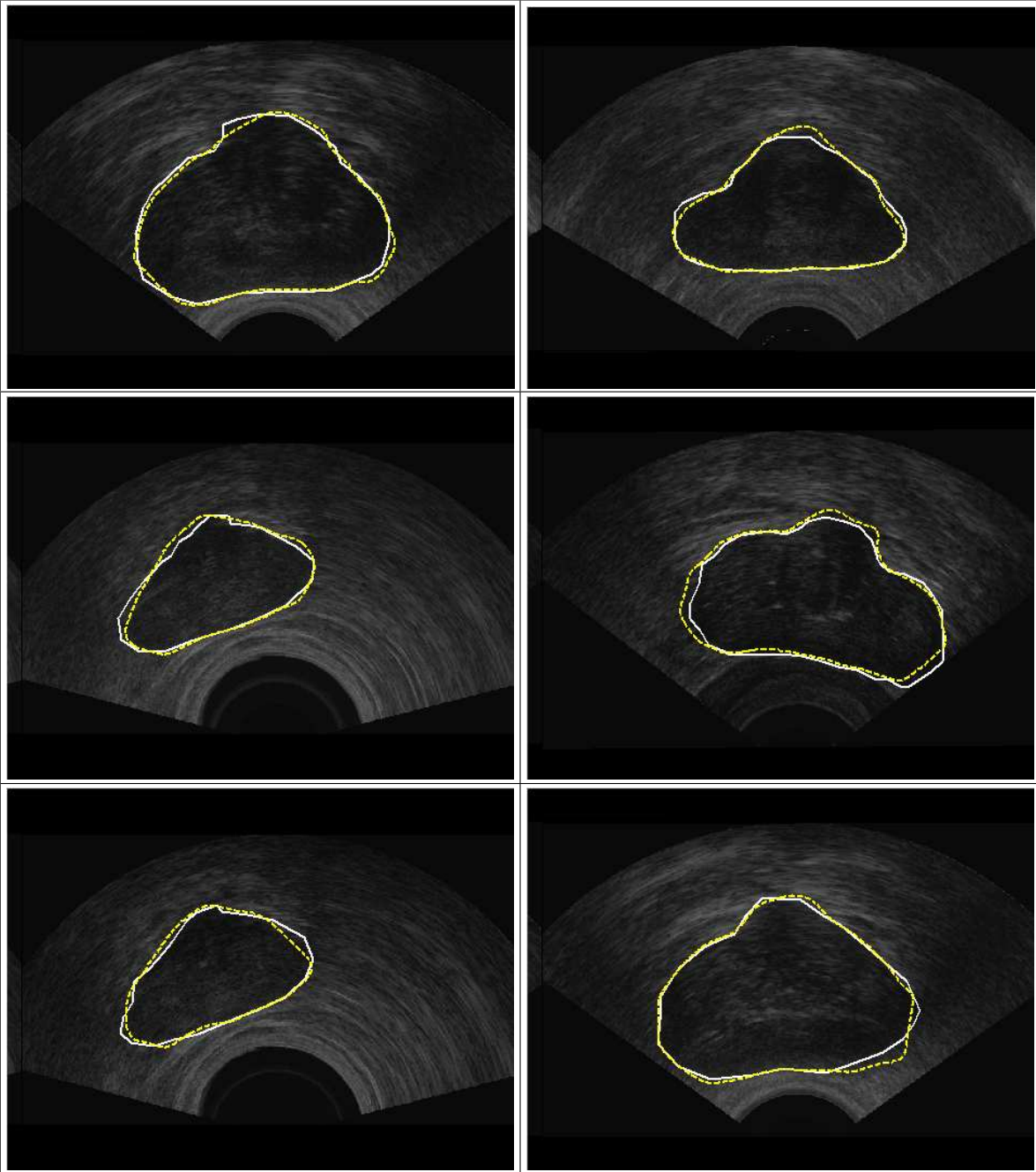


Figure 4.10: Proposed automatic segmentation (dash line) versus manual segmentation (solid line)

4.5 Evaluation of Prostate Segmentation Algorithm

The proposed algorithm is evaluated by using distance-base and area-based metrics, adopted in the literature [122]. The procedures of these metrics are described in the next two sections.

4.5.1 Distance-Based Metrics

The procedure of the distance-based metrics is summarized [122].

1. Find the centre of gravity of the manually identified boundary C_m .
2. Calculate the radial distances of both the manual contour and the proposed algorithm contour from the centre point, C_m , as indicated in Figure 4.11.
3. Evaluate the differences in the distances as a function of the angle as denoted in Figure 4.12, and expressed as

$$d(\theta_i) = d_a(\theta_i) - d_m(\theta_i), \quad (4.1)$$

where

$$i = 1, 2, \dots, N$$

N = the total number of radial angles

$d_a(\theta_i)$ = the radial distances of the proposed algorithm contour from the centre point C_m

$d_m(\theta_i)$ = The radial distances of the manual contour from the centre point C_m .

4. Calculate the Mean Difference MD which indicates the average error in the segmentation by

$$MD = \sum_{i=1}^N d(\theta_i)/N. \quad (4.2)$$

5. Compute the Mean Absolute Difference MAD which shows the average absolute error in the proposed algorithm with respect to the manual segmentation by

$$MAD = \sum_{i=1}^N |d(\theta_i)| / N. \quad (4.3)$$

6. Determine the MAXimum Difference $MAXD$ which presents the max absolute error in the segmentation by

$$MAXD = \max(|d(\theta_i)|). \quad (4.4)$$

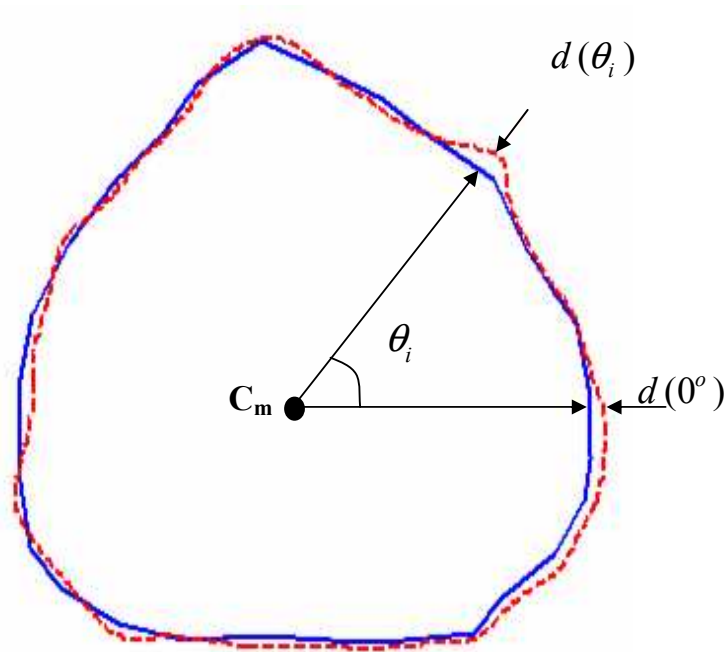


Figure 4.11: Manual (solid) and automatic (dotted) segmentation

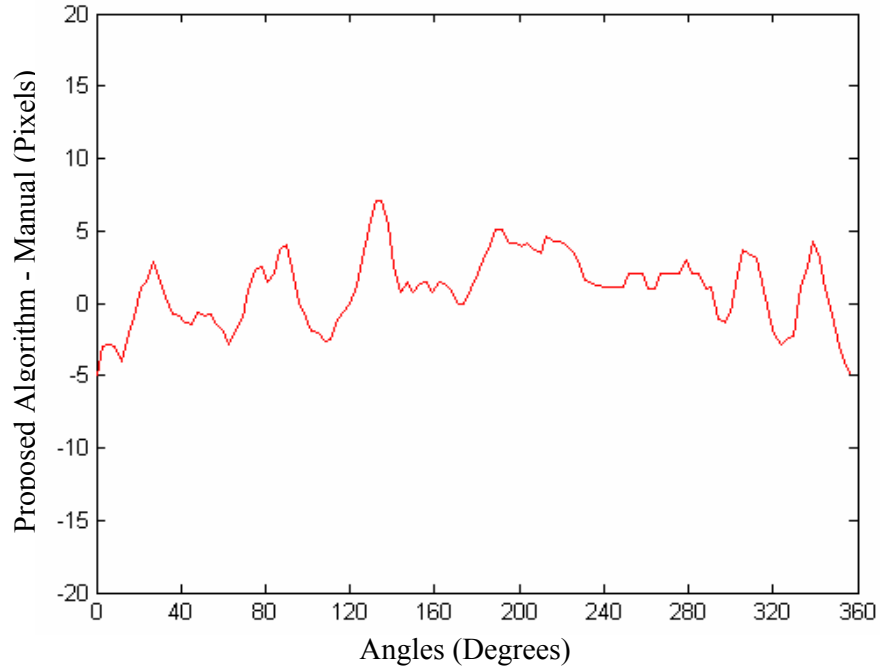


Figure 4.12: Radial difference between the proposed algorithm and the manual contour as a function of the angle

4.5.2 Area-Based Metrics

The area-based metrics procedure is also summarized [122].

1. Calculate the true positive area TP which is defined by the common area between both the manual and the proposed algorithm contours, as displayed in Figure 4.13.
2. Compute the false positive area FP which is equal to the area inside the proposed algorithm contour but outside the manual contour, as indicated in Figure 4.13.
3. Evaluate the false negative area FN which is represented by the area inside the manual contour but outside the proposed algorithm contour, as depicted in Figure 4.13.
4. Calculate the area inside the manual contour A_m .

5. Compute the sensitivity from the following:

$$\text{Sensitivity} = C_s = TP/A_m. \quad (4.5)$$

6. Then compute the accuracy by the following formula.

$$\text{Accuracy} = C_a = 1 - (FP + FN)/A_m \quad (4.6)$$

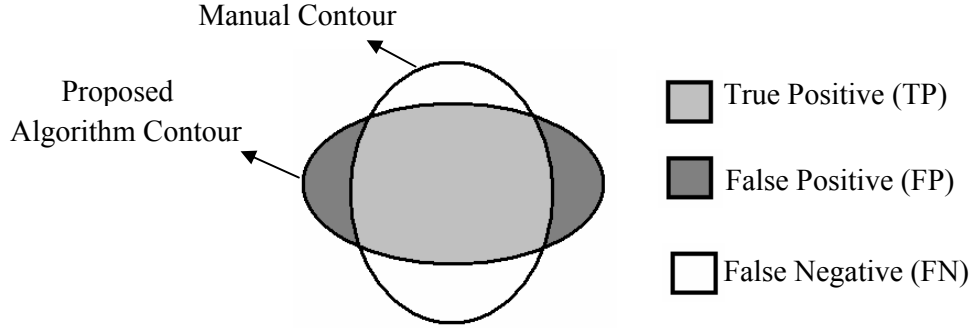


Figure 4.13: Area-based metrics

4.5.3 Testing the Results of the Proposed Algorithm

The distance-base and area-base metrics are adopted to evaluate the proposed algorithm contour with respect to the manual contour. The performance of the new algorithm is compared with the performance of the algorithms, proposed by Ladak et al. [122] and Pathak et al. [127]. The proposed algorithm performance and that of the others are summarized in Table 4.1.

Table 4.1 shows that the proposed algorithm is more accurate than Pathak's algorithm. However, there is not enough information to evaluate Pathak's algorithm. Therefore, the proposed algorithm is compared only with Ladak's algorithm. The hypotheses, in this thesis, are that the proposed algorithm has smaller *MAD* and *MAXD* errors, and higher sensitivity and accuracy than those of Ladak's. Although the *MD* error of the novel algorithm is much less than that of Ladak's algorithm, it is not evaluated by hypothesis testing. A smaller *MD* does not mean that the errors are insignificant, yet the summations

Table 4.1: Comparison between the proposed algorithm and two other algorithms proposed by Ladak et al. [122] and Pathak et al. [127]

Measures	Proposed algorithm		Ladak et al. [122]		Pathak et al. [127]	
	Average	Standard deviation	Average	Standard deviation	Average	Standard deviation
MD (pixels)	-0.009	1.609	-0.5	2.3	–	–
MAD (pixels)	3.384	0.754	4.4	1.8	7.9	–
$MAXD$ (pixels)	14.167	4.886	19.5	7.8	21.1	–
Sensitivity (%)	95.607	2.508	94.5	2.7	–	–
Accuracy (%)	91.271	2.640	90.1	3.2	–	–

of the positive errors and of the negative errors are close to each other. Therefore, an MD error measure is not a powerful measure to compare the contours. However, the average value of MD in the proposed algorithm is, approximately, equal to zero, which indicates that this error behaves like that of a random noise. In other words, the proposed algorithm is not biased either positively or negatively. There are two principal types of hypothesis testing: directional (one-tailed) and nondirectional (two-tailed) hypotheses. The former is used, when one direction change (an increase or a decrease) is specified beforehand, whereas, the latter is used when the hypothesized change can be either an increase or a decrease [138].

To investigate if a one-tailed hypothesis such as the MAD or $MAXD$ error of Ladak's algorithm is greater than that of the proposed algorithm, the procedure given in Appendix B is conducted. During the analysis, Ladak's algorithm is represented by the subscript 1 and the proposed algorithm is represented by the subscript 2.

To investigate if a one-tailed hypothesis such as the sensitivity or accuracy of the proposed algorithm is greater than that of the Ladak's algorithm, the same procedure given in Appendix B is applied, but the subscripts are exchanged. Thus, Ladak's algorithm is assigned subscript 2 whereas the proposed algorithm is assigned subscript 1.

The number of images used in the proposed algorithm and Ladak's algorithm are 50 and 117, respectively. Therefore, the degree of freedom df is equal to 165. The critical value t_{cv} is equal to 1.654 with a 0.05 level of significance, $\alpha = 0.05$. This value is obtained from the t statistical tables [138]. Table 4.2 and Table 4.3 indicate the hypotheses testing for MAD , $MAXD$, sensitivity and accuracy. The decision of all these hypotheses is to reject the null and support the alternative hypotheses, proving with a statistical confidence that the new algorithm is better than the one obtained by Ladak et al.

Table 4.2: Hypotheses testing for MAD and $MAXD$ errors

Measures	Ladak \bar{x}_1	Proposed \bar{x}_2	Ladak s_1	Proposed s_2	s_p^2	$s_{\bar{x}_1 - \bar{x}_2}$	t_{obs}	t_{cv}	Decision
MAD	4.4	3.384	1.8	0.754	2.447	0.264	3.843	1.654	Reject
$MAXD$	19.5	14.167	7.8	4.886	49.862	1.193	4.470	1.654	Reject

Table 4.3: Hypotheses testing for sensitivity and accuracy

Measures	Proposed \bar{x}_1	Ladak \bar{x}_2	Proposed s_1	Ladak s_2	s_p^2	$s_{\bar{x}_1 - \bar{x}_2}$	t_{obs}	t_{cv}	Decision
Sensitivity	95.607	94.5	2.508	2.7	6.993	0.447	2.477	1.654	Reject
Accuracy	91.271	90.1	2.640	3.2	9.269	0.514	2.276	1.654	Reject

4.6 Summary

In this chapter, a multi-stage computerized technique is proposed to automatically detect the boundary of the prostate in TRUS images. The new algorithm consists of five stages. In the first stage, the knowledge-based rules are built off-line. In the image enhancement stage,

the algorithm enhances the edges, and at the same time, filters out the noise in the image by the proposed sequential sticks technique and Gaussian kernel smoothing as described in the second stage. Then, a seed point is found automatically inside the prostate by using knowledge-based rules in the third stage. In the fourth stage, the edge map is found using a Canny edge detector. The false edges are then removed by applying knowledge-based rules collected from experts and morphological operators. After the prostate boundary is found by radial scanning the image from the seed point, the resultant boundary is adopted as an initial contour for the GVF deformable model. Afterwards, the algorithm finds the outer boundary of the prostate. In the last stage, the prostate is extracted from the raw ultrasound image by using the previously found boundary. Then, the algorithm crops the image to the size of the prostate to save computational time and storage space for the regions of interest segmentation which is described in the following chapter. The newly devised prostate segmentation algorithm is fully automated and does not require any input from the operator. Consequently, the results of the algorithm are operator-independent. Moreover, the program can be applied for twenty-four hours a day to segment hundreds of images. The proposed algorithm is evaluated with respect to manual outlining by using distance-based and area-based metrics. The automated algorithm is compared with two well-known semi-automatic algorithms to show that it is superior. With hypothesis testing, the superiority of the proposed algorithm is also proven. The presented results show that the proposed algorithm is capable of efficiently extracting prostate images with any shape and orientation from ultrasound images for further analysis.

Chapter 5

Regions of Interest Segmentation

5.1 Introduction

The purpose of this part of the research is to select the regions, which are more likely to develop cancer. In this chapter, a novel approach by using a level set is proposed to accurately identify the hypoechoic regions which are more likely to show cancer. The proposed algorithm can assist the radiologist in identifying the regions which require to be medically examined by biopsies. Also, the proposed technique saves considerable time and effort.

5.2 Related Work

Some researchers have introduced various techniques for ROI segmentations. Felzenszwalb et al. [139] have proposed a graph-theoretic approach to segment different regions in the image. Although this approach indicates promising results for some images, it is not suitable for ultrasound images. Hui [140] has tried the graph-theoretic approach to segment different regions in ultrasound images. However, the results are poor because it produces concentric ring-shaped regions, as portrayed in Figure 5.1. Therefore, Hui [140] has abandoned this approach and adopted a simple thresholding technique. However, it too has its own limitations, since it assumes the availability of the boundary of the transition

zone which is usually not available.

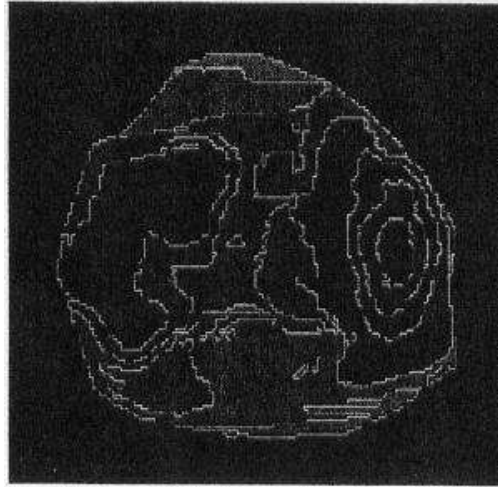


Figure 5.1: Regions segmentation using graph theory [140]

Another technique has been suggested by Mohamed et al. [141, 142] to segment the ROI by using Gabor filter. However, this technique also generates concentric regions, defeating the purpose of ROI segmentation and degrading the performance [140]. Concentric regions cause classification confusion, as described in Section 5.3. Besides, this technique misses some regions which are marked by the expert radiologist. Moreover, using most of the data set as a training data can lead to over fitting or biasing problems. To avoid any biased results, it is better to utilize unsupervised technique. Potocnik et al. [143] have chosen region growing to detect the ovarian follicle in ultrasound images. They have based their algorithm on their knowledge that the follicles appear as homogeneous regions. However, the produced edges were jagged. Fukushima et al. [144] have used Neural Networks NN to diagnose diffuse liver diseases. They have chosen five ROI (32x 32 pixels). They consist of a centre one and four overlapped ROIs. Each of the overlapped ROI contains half of the centre ROI. Then, the authors have calculated some features for these ROIs and use a NN as a classifier. A large training set is required which is not available in this thesis. Zayed et al. [145] have used fuzzy c-means to segment the fetal ultrasound images, presenting some preliminary, yet promising, results.

5.3 Goals of the ROI Segmentation Algorithm

The main purpose of the ROI segmentation is to find the regions in the prostate which are more likely to exhibit prostate cancer. The goals considered during implementing the proposed ROI algorithm are:

1. The algorithm should not require any training data so as to avoid any over-fitting or biasing results. It is challenging to create a decent training-data-set in the medical field, especially if it is created by an expert.
2. The resultant regions should not overlap; $R_i \cap R_j = \phi$ for $i \neq j$. If this condition is not fulfilled, this leads to a confusion situation in the classification. For instance, if $R_i \cap R_j = R_c$, and the classifier labels R_i , and R_j with different classes, the class of the intersection region R_c is unavailable.
3. The obtained ROI should contain the regions which are marked by the experts to ensure that the proposed algorithms do not miss any cancerous regions.
4. The novel algorithm should be able to segment multiple regions with any shape.
5. The proposed algorithm should be able to segment the hypoechoic regions which have weak edges or even no edges.

As discussed in Sections 3.3.7 and 4.2, the deformable models are quite powerful approach for image segmentation. One of the parametric deformable models is successful in segmenting the prostate image in Chapter 4. Although the parametric dynamic contour technique can segment a single region quite well, it is very difficult to segment multiple regions, as required in this chapter. It is easier to transfer the problem into a 3D one by using a level set approach to handle the topology changes such as splitting and the merging of the contours. The algorithm proposed in this chapter requires one of the geometric deformable models called "active contours without edges," discussed previously in Section 3.3.7.2.1. The details of the proposed algorithm are described in the next section.

5.4 Algorithm Description

The proposed algorithm for ROI segmentation consists of the five main stages in Figure 5.2.

1. Building the ROI knowledge-based rules
2. Enhancing the image
3. Finding the hypoechoic regions
4. Eliminating the regions which are not likely to exhibit cancer
5. Extracting the ROI

In the first stage of the proposed ROI algorithm, the ROI knowledge-based rules are built offline. These rules are built by using the knowledge of the two medical radiologists, as discussed in Section 4.3.1.

In the second stage, the proposed algorithm replaces the background of prostate image by a bright colour to force the contours to select the hypoechoic regions, and enhances the contrast of the prostate image using the proposed sequential sticks technique, discussed in Section 4.3.2.1.

The third stage, finding the hypoechoic regions, is the principal stage in the algorithm. In this stage, the newly developed algorithm starts by drawing an initial contour which does not require any points to be entered by an operator. Then, this initial contour deforms under the inside and outside forces. This initial contour can be split into multiple contours. These contours can be split or merged to minimize the energy function, until the minimum value of the energy function is achieved. In each iteration, the background colour is dynamically changed to prevent the contours from selecting the prostate and focus on the regions in the prostate. The last step is to mark the different regions inside the final contours.

In the fourth stage, the proposed algorithm eliminates the regions which are not likely to be cancerous. First, the algorithm eliminates the small regions which represent the urethra and the clustered noise regions. Then, the proposed algorithm eliminates the central zone because it is not likely to have cancer, as discussed in Section 2.2.

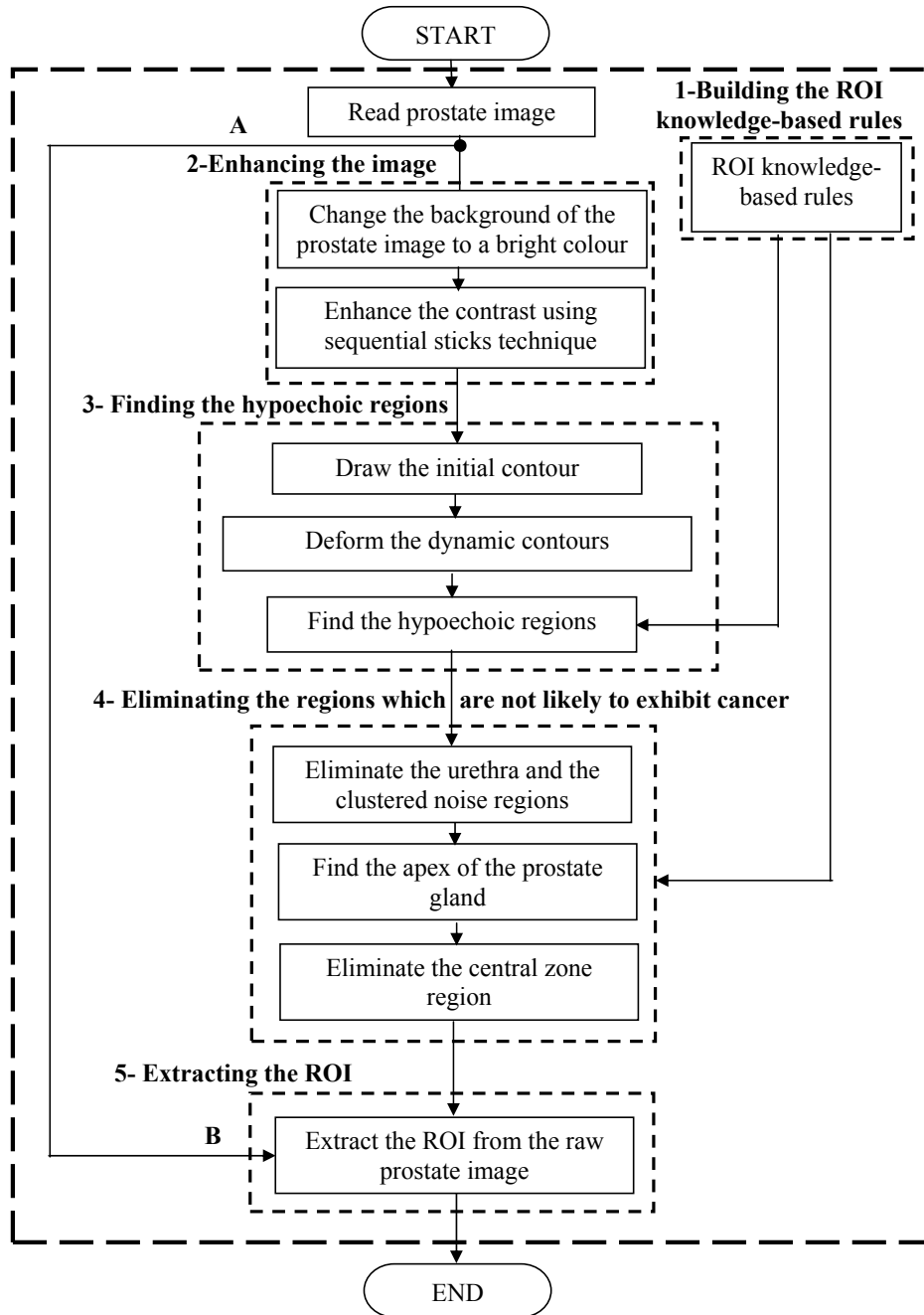


Figure 5.2: Proposed regions of interest segmentation flow chart

In the last stage, the algorithm extracts the regions of interest from the raw prostate image and not from the processed image to be ready for further analysis.

5.4.1 Building the ROI Knowledge-Based Rules

The main knowledge-based rules for the ROI segmentation are now summarized.

1. The hypoechoic regions are more likely to exhibit cancer
2. The peripheral zone is more likely to show cancer.
3. The central zone is unlikely to have cancer.
4. It is less likely to have many scattered small regions of cancer that can be recognized radiologically.

5.4.2 Enhancing the Image

This stage consists of two steps. In the first step, the proposed algorithm replaces the background of prostate image by a bright colour to ensure that the regions inside the contours are the hypoechoic regions, not hyperechoic regions. It is found that replacing the intensity level of the background of the prostate image by 0.7 or more for the first iteration ensures that the algorithm selects the hypoechoic regions. It is worth noting that the background colour of the prostate image changes dynamically during the contour deformation.

The goal of the second step of this stage is to enhance the contrast of the different regions of the prostate image. The proposed sequential sticks technique is adopted which is successful for enhancing the ultrasound image, as illustrated in Section 4.3.2.1. In this step, sequential sticks with different lengths from 3 pixels to 11 pixels with an increment of 2 are applied to enhance the various regions inside the prostate.

5.4.3 Finding the Hypoechoic Regions

The goal of this primary stage is to find the hypoechoic regions inside the prostate by using geometric deformable models. This stage consists of the following.

1. Draw the initial contour
2. Deform the dynamic contours
3. Find the hypoechoic regions

In the first step of this stage the proposed algorithm draws an initial contour. This initial contour does not require any initial points to be defined manually.

In the second step the proposed algorithm deforms the initial contour constructed in the previous step. Then, this contour is splitted into multiple contours. Some of these contours may be merged later. Then, the proposed algorithm keeps deforming, splitting, and merging the contours until the energy function is minimized.

The last step of this stage, *find the hypoechoic regions*, is straightforward. In this step, the algorithm marks the hypoechoic regions which have positive level set values as illustrated in Figure 3.7.

The details of these steps are given in the following subsections.

5.4.3.1 The Initial Contour

The goal of the first step is to draw an initial contour. It does not require any points to be entered manually. The initial level set function ϕ_o represents a part of a right cone centred in the image such that the zero-level contour is a circle inside the image as illustrated in Figure 5.3 and Figure 5.4.

The initial level set function is to achieve the required shape displayed in Figure 5.3 is given by the following equation:

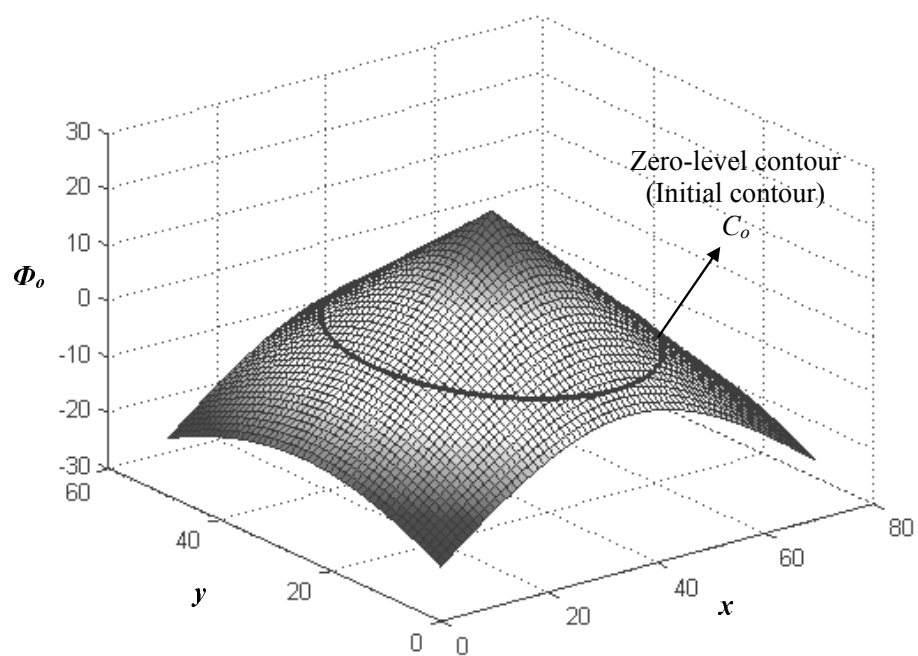
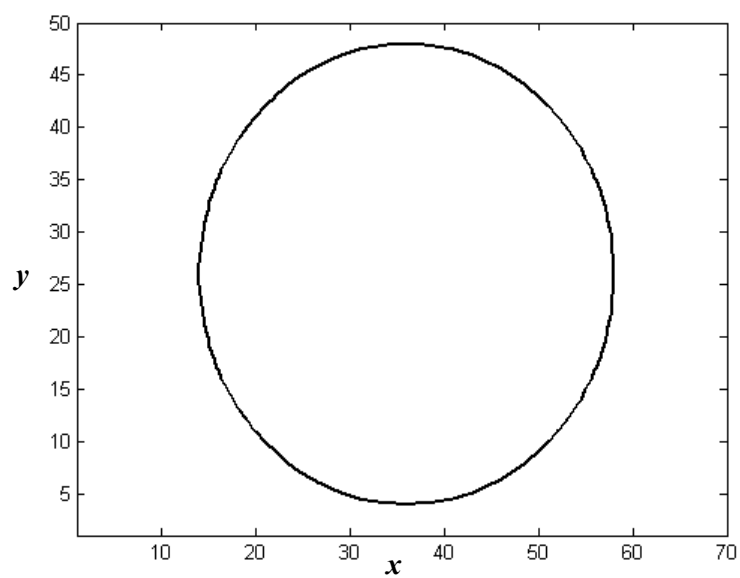
$$\phi_o(x, y) = \phi(t = 0, x, y) = h - \sqrt{(x - x_c)^2 + (y - y_c)^2}, \quad (5.1)$$

where

ϕ_o is the initial level set function.

x_c is the centre of the image in the x direction.

y_c is the centre of the image in the y direction.

Figure 5.3: Initial level set function ϕ_0 Figure 5.4: Zero-level contour (initial contour C_0)

h is a shift given by the following equation.

$$h = \frac{\min(r, c)}{2} - b, \quad (5.2)$$

where

r is the number of rows of the prostate image.

c is the number of columns of the prostate image.

b is a constant ≥ 0 to attain a closed contour. $b = 3$ is chosen in the proposed algorithm.

The value of the initial level set function inside the initial contour is positive, and outside the initial contour is negative, as illustrated in Figure 3.7. The initial contour C_o , initial zero level set, is found as follows:

$$C_o = \{(x, y) \in \Omega : \phi_o(x, y) = 0\}, \quad (5.3)$$

where

ϕ_o is the initial level set function.

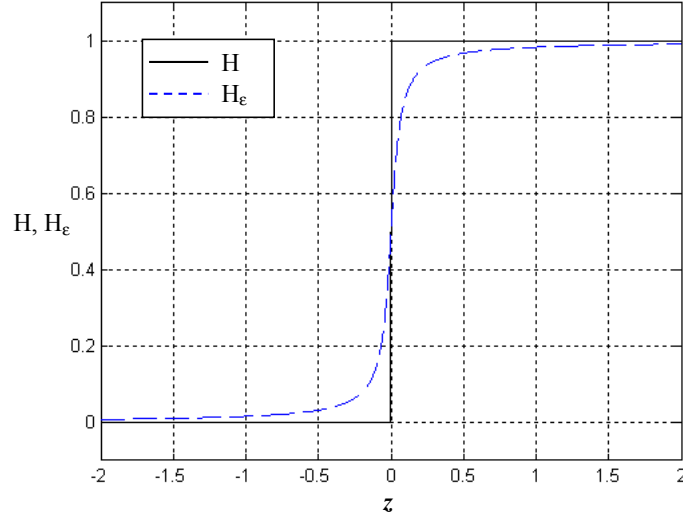
Ω The set of the prostate image.

5.4.3.2 Dynamic Contours Deformation

The active contours without edges technique, described in Section 3.3.7.2.1 is adopted. The energy function which required to be minimized is given in 3.39. A regularized version of Heaviside H and Dirac δ_o functions is also required to be able to evaluate the Euler-Lagrange equation for the unknown function ϕ . The regularized version of H , δ_o functions, given in 3.34, are denoted by H_ε , and δ_ε , respectively. H_ε , is formulated as follows [61]:

$$H_\varepsilon(z) = \frac{1}{2} \left(1 + \frac{2}{\pi} \arctan \left(\frac{z}{\varepsilon} \right) \right) \quad (5.4)$$

H_ε converges to H as ε approaches zero. Figure 5.5 shows $H_\varepsilon(z)$ versus $H(z)$. Thus, δ_ε is

Figure 5.5: $H_\varepsilon(z)$ versus $H(z)$

computed as follows:

$$\delta_\varepsilon = \frac{d}{dz} H_\varepsilon(z) = \frac{1}{\pi} \left(\frac{\varepsilon}{z^2 + \varepsilon^2} \right). \quad (5.5)$$

and the energy function in 3.39 is written as

$$\begin{aligned} F_\varepsilon(c_1, c_2, \phi) = & \mu \int_{\Omega} \delta_\varepsilon(\phi(x, y)) |\nabla \phi(x, y)| dx dy \\ & + \nu \int_{\Omega} H_\varepsilon(\phi(x, y)) dx dy \\ & + \lambda_1 \int_{\Omega} |\mu_o(x, y) - c_1|^2 H_\varepsilon(\phi(x, y)) dx dy \\ & + \lambda_2 \int_{\Omega} |\mu_o(x, y) - c_2|^2 (1 - H_\varepsilon(\phi(x, y))) dx dy. \end{aligned} \quad (5.6)$$

The equation in $\phi(t, x, y)$ becomes

$$\frac{\partial \phi}{\partial t} = \delta_\varepsilon(\phi) \left[\mu \operatorname{div} \left(\frac{\nabla \phi}{|\nabla \phi|} \right) - \nu - \lambda_1 (u_o - c_1)^2 + \lambda_2 (u_o - c_2)^2 \right] = 0. \quad (5.7)$$

The initial condition is shown in 5.1 and 5.2, whereas the initial contour is found by using 5.3. Let Δt be the time step, and h be the space step. As a result, any pixel in the image can be represented by using the space step h as follows. $(x_i, y_i) = (ih, jh)$. Consequently, the level set function at any time is expressed by

$$\phi_{i,j}^n = \phi(n\Delta t, ih, jh), n \geq 0, \phi^o = \phi_o. \quad (5.8)$$

The equation in ϕ can be discretized by using the following finite differences:

$$\begin{aligned}\Delta_-^x \phi_{i,j} &= \phi_{i,j} - \phi_{i-1,j}, & \Delta_+^x \phi_{i,j} &= \phi_{i+1,j} - \phi_{i,j}, \\ \Delta_-^y \phi_{i,j} &= \phi_{i,j} - \phi_{i,j-1}, & \Delta_+^y \phi_{i,j} &= \phi_{i,j+1} - \phi_{i,j}.\end{aligned}\quad (5.9)$$

Consequently, 5.7 is discretized as follows [61]:

$$\begin{aligned}\frac{\phi_{i,j}^{n+1} - \phi_{i,j}^n}{\Delta t} &= \delta_h(\phi_{i,j}^n) \left[\frac{\mu}{h^2} \Delta_-^x \cdot \left(\frac{\Delta_+^x \phi_{i,j}^{n+1}}{\sqrt{(\Delta_+^x \phi_{i,j}^n)^2 / (h^2) + (\phi_{i,j+1}^n - \phi_{i,j-1}^n)^2 / (2h)^2}} \right) \right. \\ &+ \frac{\mu}{h^2} \Delta_-^y \cdot \left(\frac{\Delta_+^y \phi_{i,j}^{n+1}}{\sqrt{(\phi_{i+1,j}^n - \phi_{i-1,j}^n)^2 / (2h)^2 + (\Delta_+^y \phi_{i,j}^n)^2 / (h^2)}} \right) \\ &\left. - \nu - \lambda_1 (u_{o,i,j} - c_1(\phi^n))^2 + \lambda_2 (u_{o,i,j} - c_2(\phi^n))^2 \right]\end{aligned}\quad (5.10)$$

ϕ^{n+1} is obtained by solving 5.10 iteratively.

The algorithm used in this step is summarized as follows.

1. Use the initial level set function $\phi^o(\phi^n, n = 0)$, generated in the previous step 5.1.
2. Calculate $c_1(\phi^n)$ and $c_2(\phi^n)$ by using 3.40 and 3.41. For convenience, these equations are rewritten as

$$c_1(\phi^n) = \frac{\int_{\Omega} u_o(x, y) H(\phi^n(x, y)) dx dy}{\int_{\Omega} H(\phi^n(x, y)) dx dy} \quad (5.11)$$

and

$$c_2(\phi^n) = \frac{\int_{\Omega} u_o(x, y) (1 - H(\phi^n(x, y))) dx dy}{\int_{\Omega} (1 - H(\phi^n(x, y))) dx dy} \quad (5.12)$$

3. Replace the background of the prostate image by $c_2(\phi^n)$ to prevent the contours from selecting the prostate and focus on the regions inside the prostate.
4. Obtain ϕ^{n+1} by solving the 5.10.
5. If the stationary solution is achieved, stop the program; otherwise increment the counter ($n = n + 1$) and go to step 2.

The stopping criterion, developed in this research is computed as

$$\begin{aligned} & \int_{\Omega} H(\phi^{n+1}(x, y)) dx dy + \int_{\Omega} H(\phi^n(x, y)) dx dy \\ & - 2 \int_{\Omega} (H(\phi^{n+1}(x, y)) H(\phi^n(x, y))) dx dy \leq \zeta. \end{aligned} \quad (5.13)$$

To explain the proposed stopping criterion, consider an image with only one region, as shown in Figure 5.6. The first term of the proposed criterion, $\int_{\Omega} H(\phi^{n+1}(x, y)) dx dy$, is the area of the left ellipse which represents the marked region in the iteration number $(n + 1)$. The second term of the stopping criterion, $\int_{\Omega} H(\phi^n(x, y)) dx dy$, is the area of the right ellipse which represents the marked region in the previous iteration (n) . The area of the region number 2 in Figure 5.6 represents the area of the marked region which is not changed from iteration (n) to iteration $(n + 1)$ and is computed from $\int_{\Omega} (H(\phi^{n+1}(x, y)) H(\phi^n(x, y))) dx dy$. Twice this area is subtracted in the third term, because the area is added twice in the first two terms. The left side of the stopping criterion represents the total number of pixels added to, region 1 in Figure 5.6, or removed, region 3 in Figure 5.6, from the marked regions. The stopping factor ζ on the right side is used to insure the conversion of the solution. A fixed value of 15 pixels is assigned for the stopping factor ζ of all the images.

There are some parameters for adjusting: $\lambda_1, \lambda_2, h, \Delta t, \varepsilon, \mu$, and ν . The parameter λ_1 represent the weighting factor for the regions inside the contours, whereas λ_2 is the weighting factor for the regions outside the contour. Both weighting factors λ_1 , and λ_2 are set to one to make sure that contours are neither biased to the inside nor to the outside regions ($\lambda_1 = \lambda_2 = 1$). The space step h is set to one ($h = 1$) to obtain a fine grid, which in turn enables the contours to capture the fine details. The time step Δt is chosen to be 0.5. The regularization factor ε is set to 1. Chan et al. [61] have used various values for the length parameter μ for different images ranging from 0.0000033×255^2 to 2×255^2 . In the proposed algorithm, a fixed value for the length parameter $\mu = 0.01 \times 255^2$ is used. The parameter ν does not have a fixed value to enable the operator to obtain various cases. After all, the goal is to provide the radiologists with tools to facilitate the analysis of the images, not to replace the radiologists. The values of ν are included with the results.

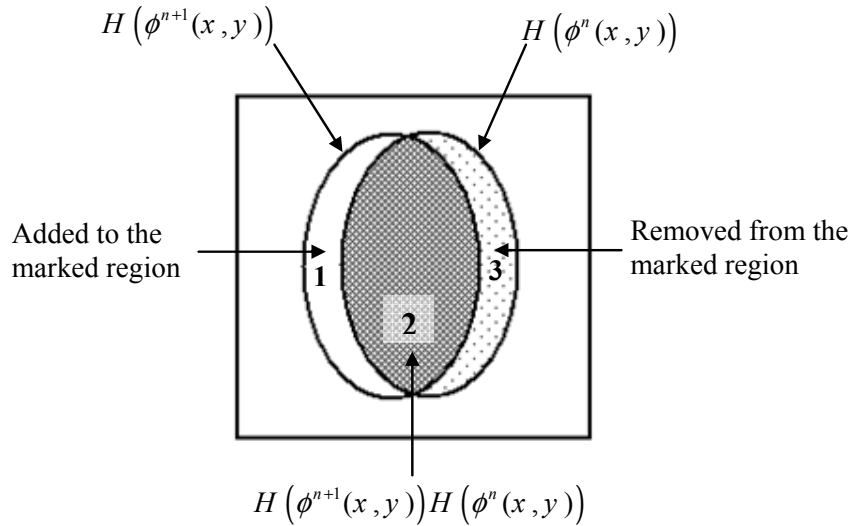


Figure 5.6: Stopping criterion

5.4.3.3 Hypoechoic Regions Marking

The goal of this step is to find and mark the hypoechoic regions, because they are more likely to exhibit cancer as stated in the first rule of the ROI knowledge-based rules (Section 5.4.1). This step is straight forward. After the final level set function ϕ^{n+1} is found, as described in the previous step, the hypoechoic regions are captured inside the contours. The hypoechoic regions are marked as shown in Figure 3.7 by applying the following equation:

$$ROI = \{(x, y) \in \Omega : \phi^{n+1}(x, y) > 0\}. \quad (5.14)$$

5.4.4 Eliminating the Regions which are not Likely to Exhibit Cancer

This stage consists of three steps as displayed in Figure 5.2.

1. Eliminate the urethra and the clustered noise regions.
2. Find the apex of the prostate gland.
3. Eliminate the central zone region.

Usually, the urethra appears in the ultrasound images as a small hypoechoic region near the centre of the prostate. Due to the noise of ultrasound images, some clustered noise regions appear as very small hypoechoic regions, scattered in the prostate gland. From the fourth rule of ROI knowledge-based rules (Section 5.4.1), *"It is less likely to have many scattered small regions of cancer that can be recognized radiologically."* Consequently, the goal of the first step of this stage is to eliminate these regions from the marked regions by removing all the regions with areas smaller than 0.025 of the prostate gland area. This factor is obtained experimentally.

In the second step, the apex of the prostate gland is obtained to find the central zone. This step consists of three substeps. First, find the centre of the transducer by finding the centre of the black circle in the middle bottom of the image. Secondly, find the centroid of the prostate gland. Thirdly, extend the line connecting between the previous two points to obtain the apex of the prostate gland.

It is stated in the third rule of the ROI knowledge-based rules (Section 5.4.1) that *"The central zone is unlikely to have cancer."* Therefore, the goal of the third step is to remove from the marked regions the central zone which is found by using the apex of the prostate, identified in the second step.

5.4.5 Extracting the ROI

This is the last stage of the proposed algorithm. Here, the remaining of the marked regions are used to extract the ROI from the raw prostate image as illustrated by the line AB in Figure 5.2.

5.5 Results

The proposed ROI segmentation algorithm is applied to 26 prostate images. It detects the hypoechoic regions inside the prostate, successfully, in all 26 images. Matlab 6.1 is used to implement the algorithm. The average execution time is about half a minute, running on a 1.3 GHz computer, to detect and extract the regions of interest from the prostate image.

The primary part in the proposed algorithm is the deformation part. The deformation technique is capable of handling multiple regions easily. Since the number of regions is

not known beforehand, the deformation technique is also capable of splitting and merging the contours as denoted in Figure 5.7. In this figure, the top row "a" shows the enhanced images resulting from the image enhancement stage of the proposed algorithm illustrated in Figure 5.2 superimposed with the initial contour computed in the first step, *draw the initial contour*, of the third stage, *finding the hypoechoic regions*, of the algorithm. Rows "b", "c", and "d" of Figure 5.7 indicate the dynamic deformation of the contours. The final contours results from the second step, *deform the dynamic contours*, of the third stage, *finding the hypoechoic regions*, of the proposed algorithm in Figure 5.2 are displayed in row "e" of Figure 5.7.

The parametric deformable model, used in Chapter 4 is not suitable in this chapter because it is difficult to split and merge the contours. The parametric deformable contours are more appropriate to segment one object. Therefore, the proposed algorithm uses a geometric deformable contour by using level set approach for segmenting multiple regions by splitting and merging.

The area weighting factor ν enables the operator to try different cases. It is worth noting that the obtained results are not sensitive to the change in the area weighting factor. In other words, a large change in the area weighting factor is necessary to obtain any noticeable effect on the resulted image. We have noticed that increasing the value for ν decreases the total regions area. As a result, it marks the darker regions which have a higher probability to exhibit prostate cancer. It might be related to the Gleason grading displayed in Figure 2.5; However, the required data to confirm or rule out the finding is not available. The area weighting factor ν , applied for each image of the 26 images is listed in Table 5.1.

Table 5.1: Area weighting factor ν

Image	1	2	3	4	5	6	7	8	9	10	11	12	13
$\nu/1000$	1.50	2.80	3.00	4.60	0.20	2.40	1.40	1.20	1.70	3.00	3.40	5.50	2.50
Image	14	15	16	17	18	19	20	21	22	23	24	25	26
$\nu/1000$	2.50	5.60	6.90	5.00	3.50	6.00	2.50	3.60	2.50	3.00	2.50	0.80	3.00

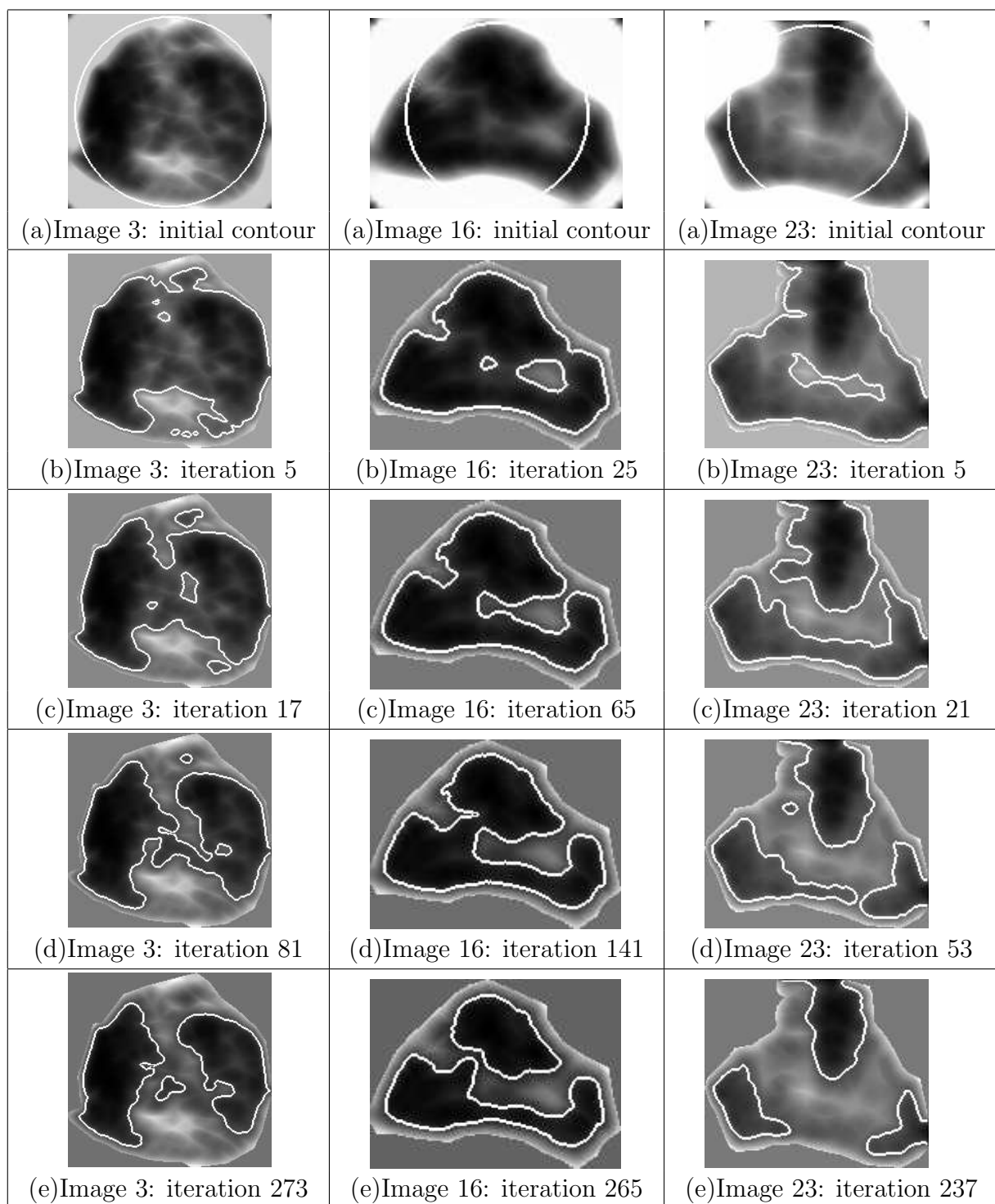


Figure 5.7: Level set deformation: (a) the initial contour, (b, c, d) intermediate contours, and (e) final contours

By using the proposed ROI algorithm, it is possible to segment the hypoechoic regions with weak or no edges. Figure 5.8 – Figure 5.11 show intermediate results of the proposed algorithm. The top row (a) of each figure portrays raw prostate images which are the inputs of the proposed ROI segmentation algorithm. Row (b) reflects the enhanced images, resulting from the second stage, *enhancing the image*, of the proposed algorithm, superimposed with the initial contours. These initial contours are computed in the first step, *draw the initial contour*, of the third stage of the proposed algorithm. The final contours after deformation resulted from the second step, *deform the dynamic contours*, of the third stage are displayed in row (c). The hypoechoic regions resulted from the last step of the third stage, *find the hypoechoic regions*, are displayed in row (d). The final marked regions resulted from the fourth stage, *eliminating the regions which are not likely to exhibit cancer*, of the proposed algorithm are presented in row (e) in Figure 5.8 – Figure 5.11.

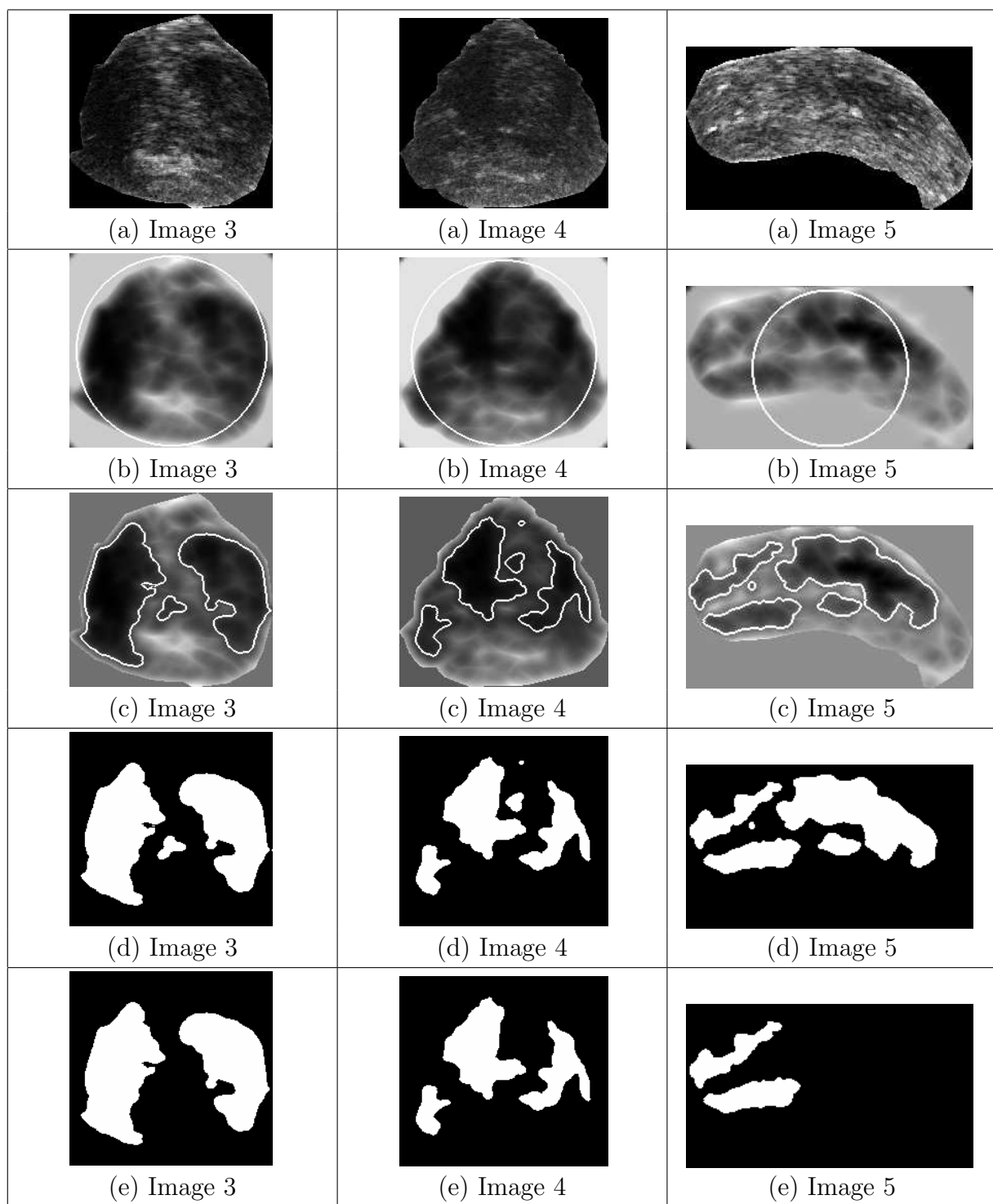


Figure 5.8: (a) Raw prostate image, (b) the initial contour superimposed on the enhanced prostate image, (c) final contours, (d) regions inside the contours, and (e) final regions of interest

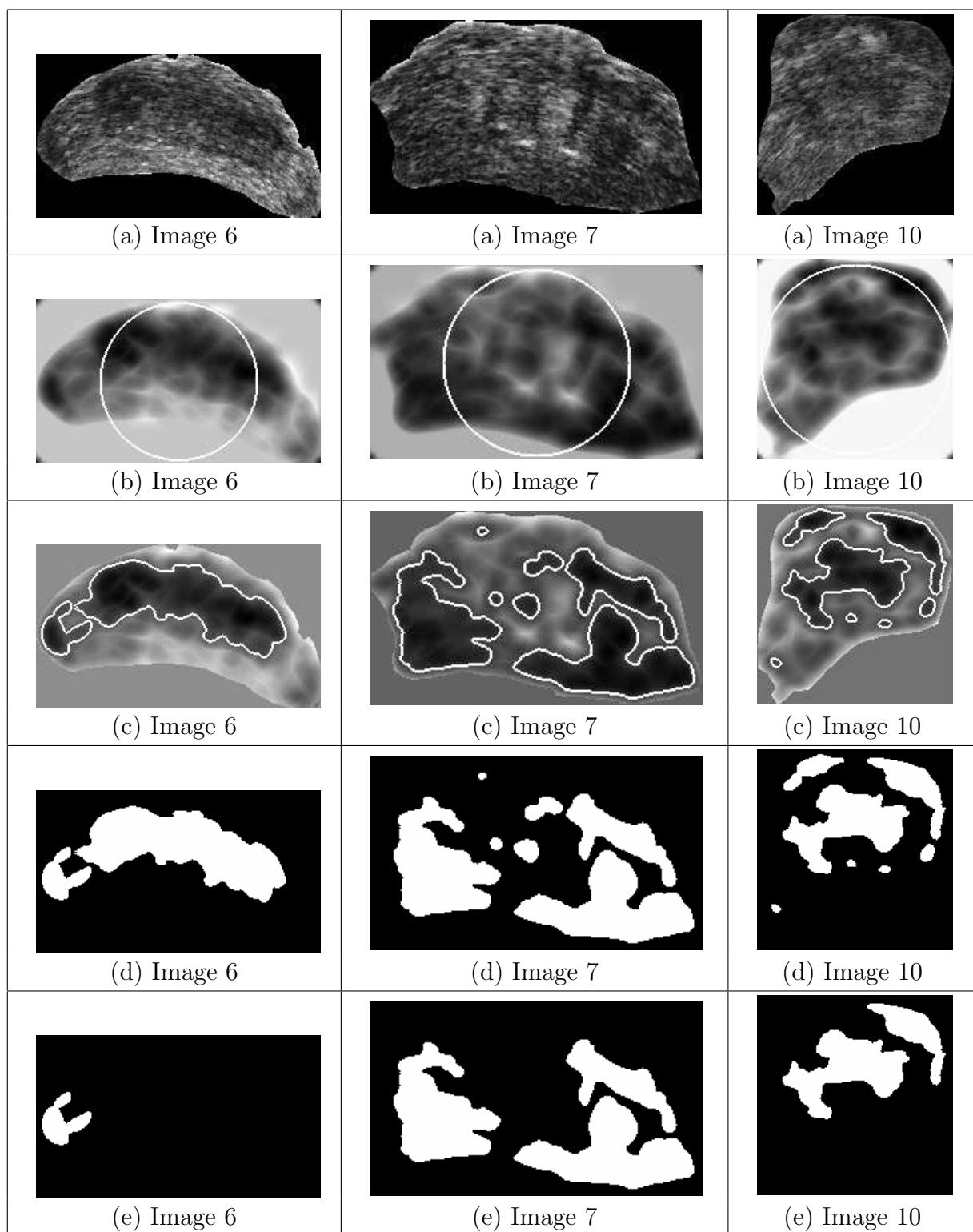


Figure 5.9: (a) Raw prostate image, (b) the initial contour superimposed on the enhanced prostate image, (c) final contours, (d) regions inside the contours, and (e) final regions of interest

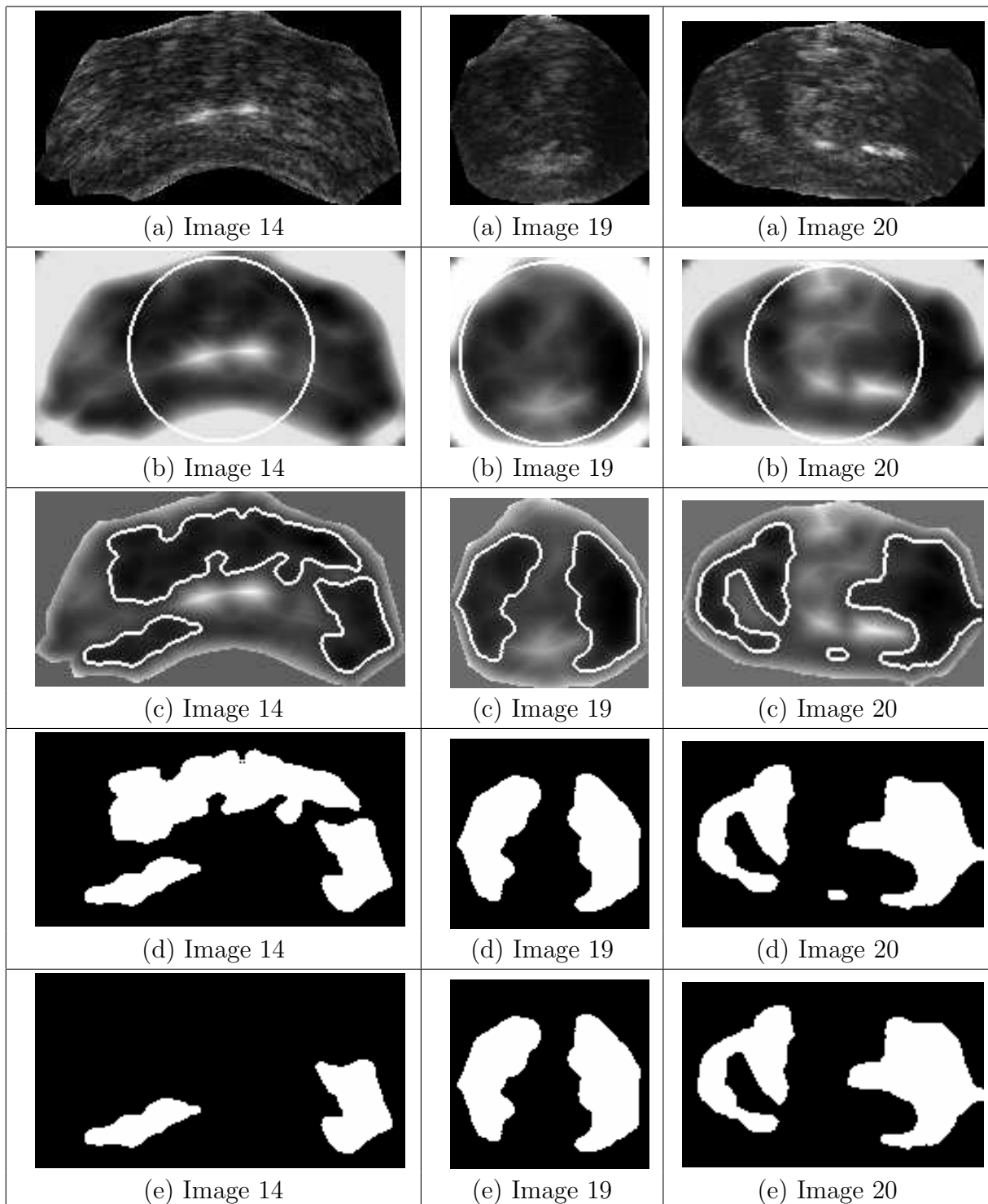


Figure 5.10: (a) Raw prostate image, (b) the initial contour superimposed on the enhanced prostate image, (c) final contours, (d) regions inside the contours, and (e) final regions of interest

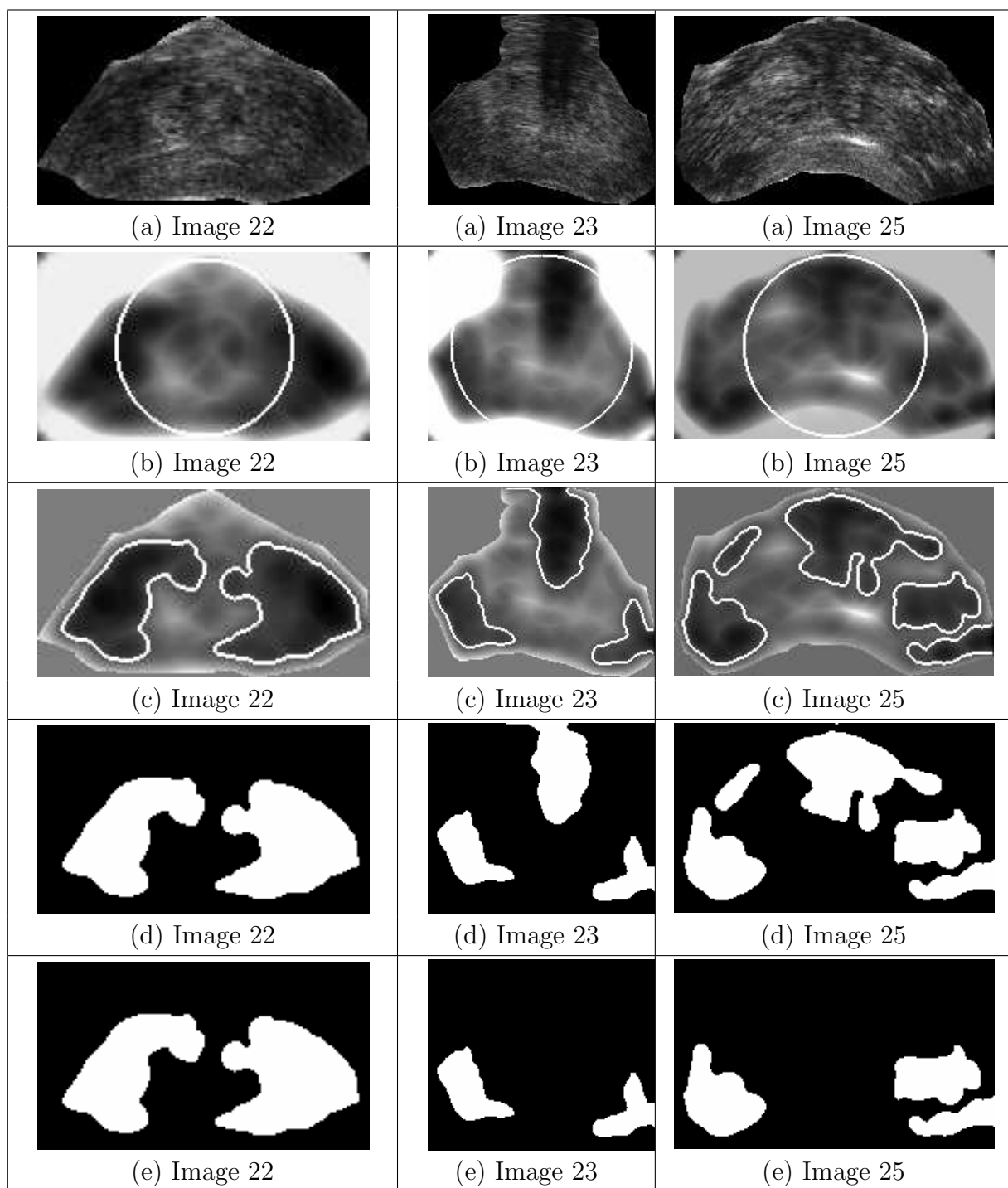


Figure 5.11: (a) Raw prostate image, (b) the initial contour superimposed on the enhanced prostate image, (c) final contours, (d) regions inside the contours, and (e) final regions of interest

5.6 Evaluation

To evaluate the results of the proposed algorithm, two radiologists are invited to mark the regions, on the same set of images, which are more likely to exhibit prostate cancer. One expert is from the University of Western Ontario in London, and the other one is from the Grand River Hospital in Kitchener. Then, the regions marked by both experts using AND operator are computed. The total regions marked by either of the two experts are calculated by using the OR operator.

Figure 5.12 reflects some results of the ROI proposed algorithm. The rest of the results are shown in Appendix C, Figure C.1 – Figure C.8. In these figures, the results of the proposed ROI algorithm are displayed in row (a). Rows (b) and (c) show the manual marking of the two experts. The common regions of the two experts "AND" are displayed in row (d), and the total marked regions by the two experts "OR" are shown in row (e). From these figures, it is clear that the proposed algorithm results are very close to those of the manual marking. In the next two sections, the proposed algorithm is evaluated using both region and pixel frameworks. The evaluation measures which are used in both frameworks follow [3].

- Accuracy: It measures the ratio between the pixels/regions which are correctly identified to the total number of pixels/regions.
- Sensitivity: It measures the accuracy of a marking method to identify all marked pixels/regions
- Specificity: It measures the accuracy of a marking method to identify all unmarked pixels/regions

To illustrate the previously mentioned evaluation measures, let us consider Table 5.2.

Table 5.2: Evaluation table [3]

Evaluated Marking	Reference	
	Marked	Unmarked
Marked	TP	FP
Unmarked	FN	TN

Where

TP is True Positive

FP is False Positive

TN is True Negative

FN is False Negative

The evaluation measures are calculated as follows:

$$Accuracy = \frac{TP + TN}{TP + FP + TN + FN} * 100\%, \quad (5.15)$$

$$Sensitivity = \frac{TP}{TP + FN} * 100\%, \quad (5.16)$$

and

$$Specificity = \frac{TN}{TN + FP} * 100\%. \quad (5.17)$$

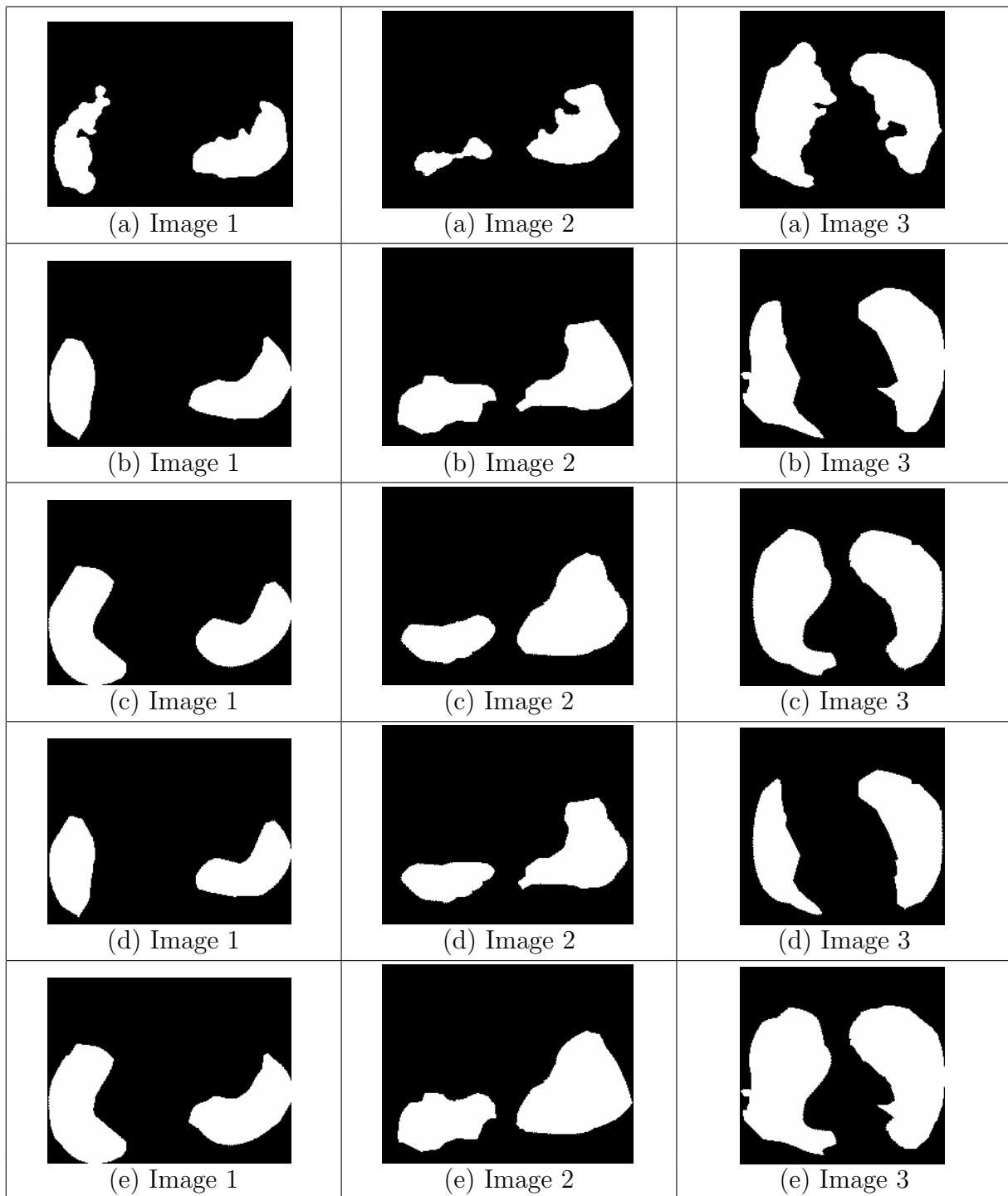


Figure 5.12: (a) ROI algorithm results, (b) manual marking of the first expert (c) manual marking of the second expert, (d) shared regions marked by both experts (AND), and (e) the total regions marked by both experts (OR)

5.6.1 Region Evaluation

To evaluate the regions wisely, it is required to calculate for each image: the total number of marked regions selected by any of the two experts, the number of those regions selected by the first expert " E_1 ", the number of those regions selected by the second expert " E_2 ", the number of those regions selected by the proposed algorithm " ROI ", and the number of the extra regions "Extra" marked by the newly devised algorithm but not marked by the experts. Counting the regions is complex. Consider image number 22 in Figure C.7 in Appendix C for instance, where the first expert marks the right region but misses the left one. However, the second expert has marked both the right and left regions, but he combines them in one region. Computing the number of regions for this image is also problematic. If the number of regions is considered one for both experts and two for the proposed algorithm, inaccuracy results for two reasons. First, counting the regions this way does not show that the first expert misses the left region, marked by the second expert. Secondly, this method of counting assumes that the proposed algorithm has marked an extra region. Of course, this is not correct because the right and the left regions are marked by one of the experts. The region counting problem can be considered as a prime decomposition problem. Consequently, the region of the second expert is decomposed into its prime regions left and right. As a result, the number of regions for the second expert is two. Thus, the total number of the marked regions is two; one of which is marked by the first expert. The use of the novel algorithm results in marking both regions with no extra regions. To generalize this technique to enable the computer to count all regions directly by the prime decomposition method, a block diagram in Figure 5.13 is designed for a maximum of three regions, but it can be extended easily to any number of regions. The logic is straight forward. If any region is intersected by two or three other regions, it is counted as two or three regions, prime regions, respectively. ROI_{ri} , in this figure, represents the number of pixels of the i^{th} region in the proposed algorithm result image. Similarly, $E1_{ri}$ and $E2_{ri}$ represent the number of pixels of the i^{th} region in the first and the second expert images, respectively. The details of the percentage intersection " $\cap\%$ " block are conveyed in Figure 5.14. Inside this block, the number of the intersected pixels " I " between regions r_1 and r_2 is first calculated by the intersection " \cap " block. The minimum area " M " of the two regions is then calculated. The intersected pixels " I " are then divided

by the minimum region area " M " and multiplied by 100 to calculate the percentage of the intersection of the two regions r_1 and r_2 . There are two reasons for using the minimum area of the two regions. First, this method ensures that $r_1 \cap \% r_2 = r_2 \cap \% r_1$, which simplifies the analysis considerably. Secondly, if one region is intersected by two or three other regions, and the percentage intersection between this large region and one of the other regions, is then calculated by dividing by the large region area, the result is small, perhaps be less than the thresholding value. As a result, the computer assumes there is no intersection which is not true. The reason for using a thresholding value is to avoid the regions which share a very small number of pixels, to be considered as intersected. Therefore, two regions are considered intersected if the percentage intersection is at least 40%. The result of the thresholding block is one if there is intersection, and zero otherwise. The extra regions are calculated by counting the regions of the proposed algorithm which are not intersected with any of the experts' regions. The rest of the block diagram is straight forward. The results of the regions counting block diagram, depicted in Figure 5.13 are summarized in Table 5.3.

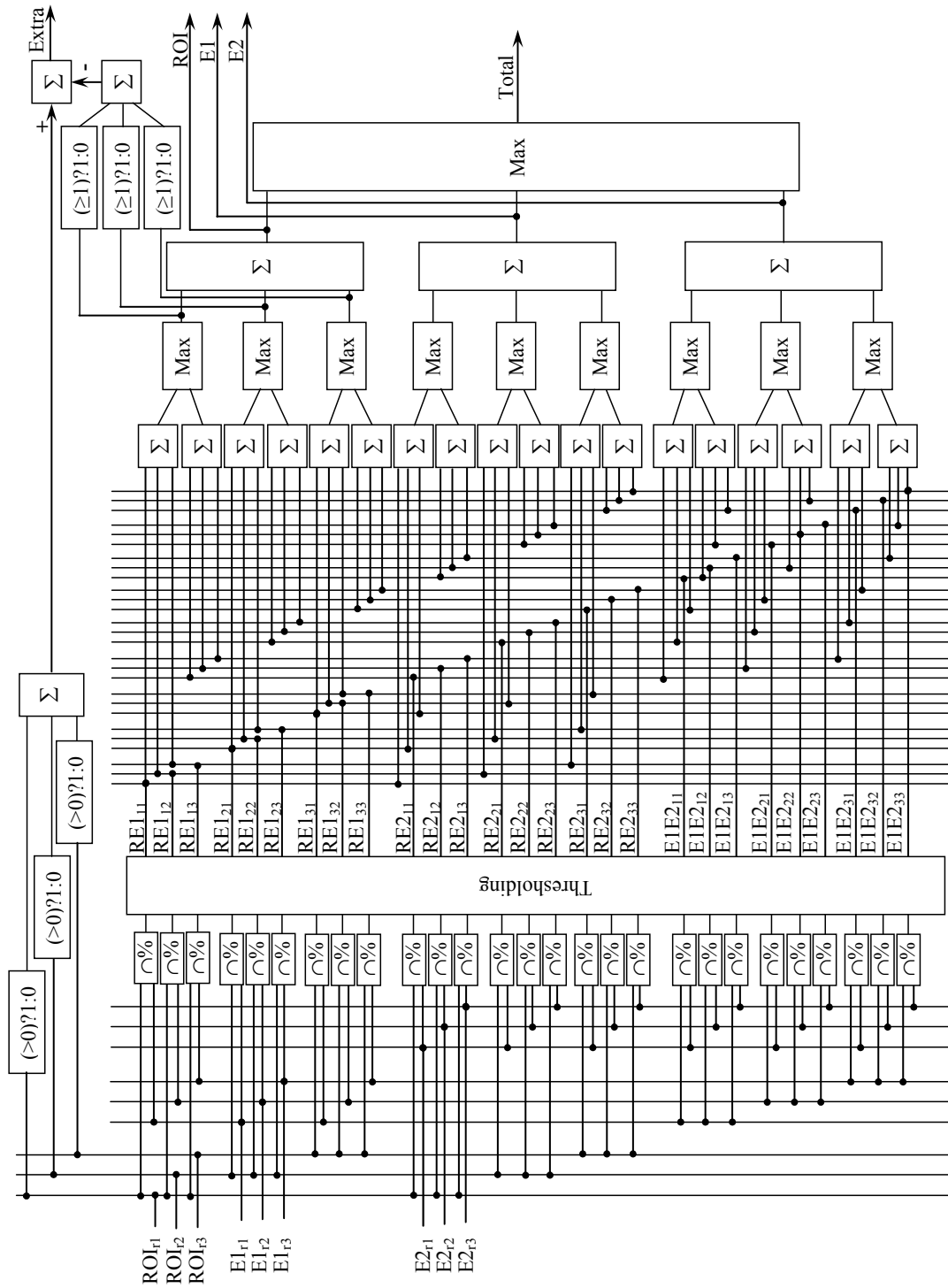


Figure 5.13: Regions counting block diagram

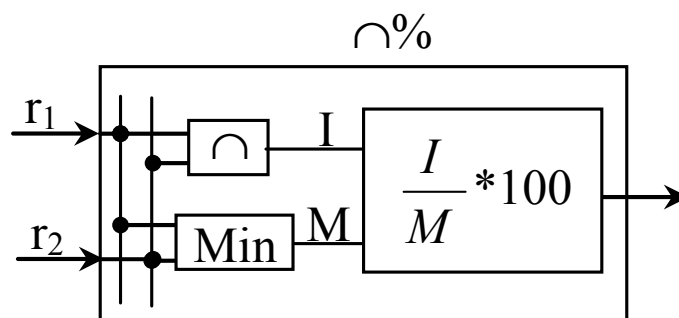


Figure 5.14: Percentage intersection block diagram

For region evaluation, two cases are studied.

1. By considering the extra regions as False Positive (*FP*) regions
2. By considering the extra regions as True Positive (*TP*) regions

The details of these two cases are discussed in the next two subsections.

Table 5.3: Number of marked regions

Image	Total Regions	E_1	E_2	ROI	$Extra$
1	2	2	2	2	0
2	2	2	2	2	0
3	2	2	2	2	0
4	3	2	3	3	0
5	2	2	2	2	0
6	1	1	1	1	0
7	3	1	3	3	0
8	2	2	2	2	0
9	2	2	2	2	0
10	2	1	1	2	0
11	4	3	3	4	0
12	1	1	1	1	0
13	1	1	1	1	0
14	1	1	1	1	1
15	2	2	2	2	0
16	1	1	1	1	0
17	2	2	2	2	0
18	2	2	2	2	0
19	2	1	2	2	0
20	2	1	2	2	0
21	1	1	1	1	0
22	2	1	2	2	0
23	2	1	2	2	0
24	1	1	1	1	0
25	3	1	3	3	0
26	1	1	1	1	0
Summation	49	38	47	49	1

5.6.1.1 Considering the Extra Regions as the FP Regions

In the first case, the extra regions, denoted by the algorithm are considered as false positive regions, because they have not been identified by either of the two experts. The region evaluation of the first expert E_1 , the second expert E_2 , the proposed *ROI* algorithm with respect to total marked regions are summarized in tables Table 5.4, Table 5.5, and Table 5.6, respectively. The evaluation is carried out by the accuracy, sensitivity, and specificity measures, described in 5.15 to 5.17.

Table 5.4: Region evaluation of the first expert (first case)

E_1	Total	
	Marked	Unmarked
Marked	38	0
Unmarked	11	27

The evaluation results for the first expert are as follow:

- $Accuracy_{E_1} = 85.53\%$
- $Sensitivity_{E_1} = 77.55\%$
- $Specificity_{E_1} = 100.00\%$

Table 5.5: Region evaluation of the second expert (first case)

E_2	Total	
	Marked	Unmarked
Marked	47	0
Unmarked	2	27

The evaluation results for the second expert are as follow:

- $Accuracy_{E_2} = 97.37\%$
- $Sensitivity_{E_2} = 95.92\%$
- $Specificity_{E_2} = 100.00\%$

Table 5.6: Region evaluation of the proposed algorithm (first case)

<i>ROI</i>	Total	
	Marked	Unmarked
Marked	49	1
Unmarked	0	26

The evaluation results for the proposed algorithm are as follow:

- $Accuracy_{ROI} = 98.68\%$
- $Sensitivity_{ROI} = 100.00\%$
- $Specificity_{ROI} = 96.30\%$

5.6.1.2 Considering the Extra Regions as the TP Regions

In the second situation, the extra regions marked by the algorithm are considered as true positive regions but are missed by both experts. The region evaluation of the first expert E_1 , the second expert E_2 , the proposed ROI algorithm, with respect to total marked regions, are shown in Table 5.7, Table 5.8, and Table 5.9, respectively. The evaluation is conducted by using the accuracy, sensitivity, and specificity measures, described in 5.15 to 5.17.

Table 5.7: Region evaluation of the first expert (second case)

E_1	Total	
	Marked	Unmarked
Marked	38	0
Unmarked	12	26

The evaluation results for the first expert are as follow:

- $Accuracy_{E_1} = 84.21\%$
- $Sensitivity_{E_1} = 76.00\%$
- $Specificity_{E_1} = 100.00\%$

Table 5.8: Region evaluation of the second expert (second case)

E_2	Total	
	Marked	Unmarked
Marked	47	0
Unmarked	3	26

The evaluation results for the second expert are as follow:

- $Accuracy_{E_2} = 96.05\%$
- $Sensitivity_{E_2} = 94.00\%$
- $Specificity_{E_2} = 100.00\%$

Table 5.9: Region evaluation of the proposed algorithm (second case)

<i>ROI</i>	Total	
	Marked	Unmarked
Marked	50	0
Unmarked	0	26

The evaluation results for the proposed algorithm are as follow:

- $Accuracy_{ROI} = 100.00\%$
- $Sensitivity_{ROI} = 100.00\%$
- $Specificity_{ROI} = 100.00\%$

A summary of the region evaluation results of both cases is shown in Table 5.10. Obviously, the algorithm yields very similar results when it is compared with those of the two experts.

Table 5.10: Summary of the region evaluation results of both cases

Measures	Case 1			Case 2		
	E_1	E_2	ROI	E_1	E_2	ROI
Accuracy	86.49	97.30	98.65	85.14	95.95	100.00
Sensitivity	78.72	95.74	100.00	77.08	93.75	100.00
Specificity	100.00	100.00	96.30	100.00	100.00	100.00

5.6.2 Pixel Evaluation

The region evaluation presented in the previous section provides a rough evaluation of the proposed algorithm. For a more precise evaluation, the novel algorithm results are pixel-wisely evaluated with respect to the manual marking of the first expert $A::E_1$, the

manual marking of the second expert $A::E_2$, agreed regions which have been marked by both experts $A::AND$, and total regions which have been marked by any of the experts $A::OR$. Moreover, the manual marking of each expert is pixel-wisely evaluated with respect to that of the other expert $E_1::E_2$, $E_2::E_1$. Then the maximum of the proposed algorithm evaluation is computed in the MAX_A column, whereas, the minimum and average of the experts evaluation is calculated in columns MIN_E and AVG_E , respectively. The accuracy, sensitivity, and specificity pixel evaluation are shown in Table 5.11, Table 5.12, and Table 5.13, respectively.

Table 5.11: Evaluation using accuracy measure (all values are a percentage)

Image	$A::E_1$	$A::E_2$	$A::And$	$A::Or$	$E_1::E_2$	$E_2::E_1$	MAX_A	MIN_E	AVG_E
1	92.5	86.0	92.2	86.3	88.8	88.8	92.5	88.8	88.8
2	82.3	84.3	86.7	79.9	89.1	89.1	86.7	89.1	89.1
3	74.1	86.5	79.0	81.6	77.4	77.4	86.5	77.4	77.4
4	61.8	76.9	67.3	71.4	66.9	66.9	76.9	66.9	66.9
5	86.8	88.2	88.3	86.7	95.0	95.0	88.3	95.0	95.0
6	92.7	89.6	94.1	88.2	93.8	93.8	94.1	93.8	93.8
7	60.3	78.4	64.8	73.8	51.7	51.7	78.4	51.7	51.7
8	85.3	79.3	88.3	76.4	75.5	75.5	88.3	75.5	75.5
9	86.8	84.8	88.7	83.0	83.3	83.3	88.7	83.3	83.3
10	64.8	78.3	72.2	70.9	50.3	50.3	78.3	50.3	50.3
11	74.3	75.5	78.1	71.7	60.6	60.6	78.1	60.6	60.6
12	73.9	85.9	79.3	80.5	74.4	74.4	85.9	74.4	74.4
13	89.0	83.5	91.0	81.5	82.6	82.6	91.0	82.6	82.6
14	61.4	66.2	62.8	64.8	78.5	78.5	66.2	78.5	78.5
15	73.2	80.5	83.4	70.4	84.9	84.9	83.4	84.9	84.9
16	78.4	82.8	82.6	78.6	85.4	85.4	82.8	85.4	85.4
17	79.4	79.8	82.2	77.0	76.2	76.2	82.2	76.2	76.2
18	63.2	74.3	74.5	63.0	81.5	81.5	74.5	81.5	81.5
19	64.0	85.9	68.5	81.4	59.0	59.0	85.9	59.0	59.0
20	71.9	80.0	73.1	78.8	73.6	73.6	80.0	73.6	73.6
21	73.0	85.6	85.8	72.8	85.6	85.6	85.8	85.6	85.6
22	58.1	78.9	60.4	76.6	57.2	57.2	78.9	57.2	57.2
23	83.1	73.4	83.9	72.7	69.2	69.2	83.9	69.2	69.2
24	88.2	89.6	89.2	88.6	88.7	88.7	89.6	88.7	88.7
25	81.0	87.7	80.7	87.9	81.1	81.1	87.9	81.1	81.1
26	47.8	93.3	93.1	48.0	47.8	47.8	93.3	47.8	47.8

Table 5.12: Evaluation using sensitivity measure (all values are a percentage)

Image	$A::E_1$	$A::E_2$	$A::And$	$A::Or$	$E_1::E_2$	$E_2::E_1$	MAX_A	MIN_E	AVG_E
1	80.0	62.8	81.6	62.7	71.0	92.9	81.6	71	81.95
2	49.8	52.8	58.0	46.6	80.3	85.8	58	80.3	83.05
3	71.8	79.0	82.0	72.0	68.6	86.2	82	68.6	77.4
4	23.4	55.0	32.0	48.8	34.9	73.0	55	34.9	53.95
5	55.0	58.5	59.3	54.5	92.5	86.6	59.3	86.6	89.55
6	37.1	28.9	42.1	26.7	68.7	85.3	42.1	68.7	77
7	50.8	65.9	67.1	61.1	24.5	75.6	67.1	24.5	50.05
8	79.0	66.6	87.8	62.6	65.8	86.1	87.8	65.8	75.95
9	79.3	73.7	86.4	69.5	76.5	86.5	86.4	76.5	81.5
10	30.3	60.0	-	48.8	0	0	60	0	0
11	52.5	53.2	75.8	48.5	26.2	43.9	75.8	26.2	35.05
12	67.0	75.2	81.1	67.0	57.8	81.0	81.1	57.8	69.4
13	49.3	39.3	57.3	36.8	43.9	84.1	57.3	43.9	64
14	45.6	55.8	51.1	53.5	35.5	89.0	55.8	35.5	62.25
15	38.5	46.2	50.6	36.1	90.9	72.2	50.6	72.2	81.55
16	59.7	63.5	66.9	58.0	78.7	87.7	66.9	78.7	83.2
17	56.1	54.0	63.6	50.6	50.6	86.6	63.6	50.6	68.6
18	50.3	63.1	65.1	50.1	88.7	73.8	65.1	73.8	81.25
19	64.6	76.8	83.0	70.6	30.7	77.1	83	30.7	53.9
20	72.9	70.7	79.6	68.2	41.6	87.7	79.6	41.6	64.65
21	37.2	52.9	53.3	37.1	99.3	66.8	53.3	66.8	83.05
22	63.5	73.1	73.7	70.1	25.8	86.0	73.7	25.8	55.9
23	45.5	36.8	48.0	36.4	29.5	88.0	48	29.5	58.75
24	9.8	36.9	11.5	34.7	37.1	85.3	36.9	37.1	61.2
25	71.4	70.0	72.6	69.8	25.4	88.0	72.6	25.4	56.7
26	29.2	84.9	88.0	30.0	90.6	29.3	88	29.3	59.95

Table 5.13: Evaluation using specificity measure (all values are a percentage)

Image	$A::E_1$	$A::E_2$	$A::And$	$A::Or$	$E_1::E_2$	$E_2::E_1$	MAX_A	MIN_E	AVG_E
1	96.6	97.1	95.4	98.6	97.4	87.5	98.6	87.5	92.45
2	96.9	100	97.1	99.9	93.4	90.5	99.9	90.5	91.95
3	75.8	95.0	77.2	95.5	87.5	71.0	95.5	71	79.25
4	71.6	93.0	73.4	92.3	90.5	65.4	93	65.4	77.95
5	97.1	97.1	96.1	98.2	95.8	97.7	98.2	95.8	96.75
6	100	99.8	99.8	100	98.0	94.9	100	94.9	96.45
7	62.4	95.6	64.4	95.1	89.1	46.1	95.6	46.1	67.6
8	89.9	94.5	88.6	97.3	87.3	68.0	97.3	68	77.65
9	92.2	94.7	89.9	98.0	89.4	81.1	98	81.1	85.25
10	72.7	86.6	72.2	92.9	72.8	61.9	92.9	61.9	67.35
11	80.4	88.5	78.4	93.9	80.6	65.3	93.9	65.3	72.95
12	77.3	95.0	78.6	95.3	88.5	71.1	95.3	71.1	79.8
13	95.6	99.8	95.5	100	96.9	82.4	100	82.4	89.65
14	63.7	70.9	64.2	70.3	98.0	77.0	70.9	77.0	87.5
15	99.4	98.3	98.3	99.5	81.8	94.5	99.5	81.8	88.15
16	91.2	98.8	91.3	99.4	90.9	83.8	99.4	83.8	87.35
17	86.9	98.2	87.2	98.5	94.4	72.8	98.5	72.8	83.6
18	77.2	82.8	80.4	80.1	75.9	89.8	82.8	75.9	82.85
19	63.8	95.9	65.7	95.8	90.0	54.2	95.9	54.2	72.1
20	71.7	86.5	71.8	86.9	96.0	70.2	86.9	70.2	83.1
21	99.7	98.8	98.8	99.7	80.1	99.7	99.7	80.1	89.9
22	57.1	85.9	58.2	85.1	95.0	51.6	85.9	51.6	73.3
23	89.2	99.2	88.8	100	97.2	66.2	100	66.2	81.7
24	94.2	99.8	94.2	99.8	98.8	89.0	99.8	89	93.9
25	81.7	93.3	81.3	93.9	98.9	80.6	93.9	80.6	89.75
26	93.0	95.8	94.4	96.9	35.0	92.6	96.9	35	63.8

From Table 5.11 to Table 5.13, it is evident that the algorithm yields similar results to those of the experts. In Table 5.11, the accuracy of the evaluation of the proposed algorithm exceeds 74.5%, except for image number 14 whose accuracy is 66.2%. This is due to the fact that the proposed algorithm indicates an extra region, not marked by either expert. Because of the uncertainty regarding whether the region is cancerous or not, it is considered to be false positive region. The minimum experts' accuracy in Table 5.11 is 47.8% for image number "26".

For the sensitivity evaluation Table 5.12, manual marking appears to include more pixels than those of the hypoechoic regions, rendering the novel algorithm's sensitivity somewhat low. The experts' sensitivity for image 10 is zero because each expert marks a different region and missed the other. The proposed algorithm sensitivity for image number 10 is 60%, because the proposed algorithm has marked both regions.

In Table 5.13 (the specificity evaluation) the proposed algorithm has a higher specificity than that of the experts' for all images except for image number 14, because the algorithm marks an extra region for this image, as mentioned in the accuracy evaluation. The pixels evaluation results of Table 5.11 to Table 5.13 are summarized in Table 5.14.

Table 5.14: Pixels evaluation summary

Measures	Experts				Proposed Algorithm			
	Min.	Max.	Average	Standard deviation	Min.	Max.	Average	Standard deviation
Accuracy	47.80	95.00	75.31	13.63	66.20	94.10	84.16	6.46
Sensitivity	0.00	86.60	50.07	23.16	36.90	88.00	66.56	14.65
Specificity	35.00	95.80	73.05	14.91	70.90	100.00	94.93	6.72

5.7 Summary

In this chapter, a ROI segmentation algorithm is developed to segment the hypoechoic regions which are more likely to exhibit cancer and should be considered for biopsies. The

proposed algorithm consists of five stages. In the first stage, the ROI knowledge-based rules are built by using the knowledge of two radiologists. In the second stage, the background of the prostate image is replaced by a bright colour such that the algorithm can select the hypoechoic regions. Then, the contrast of the prostate image is enhanced by using the proposed sequential sticks technique. In the third stage, the proposed algorithm draws an initial contour, which does not require any initial points to be entered by an operator. Then, this initial contour deforms under the inside and outside forces. A level set technique is chosen for this stage, because it is flexible enough to detect different topologies through the splitting and merging contours. Besides, the technique can detect the hypoechoic regions which have weak edges or no edges. Also, during this stage, the background colour of the prostate image is dynamically changed to prevent the contours from selecting the prostate, and focus only on the regions inside the prostate. In the last step in this stage, the different regions inside the final contours are marked if they have a positive level set function. In the fourth stage, the algorithm eliminates the regions which are less likely to be cancerous such as the small regions which represent the urethra and the clustered noise regions. Then, the proposed algorithm eliminates the central zone because it is less likely to have cancer as discussed in Section 2.2. In the last stage, the algorithm extracts the ROI, for consideration of biopsies.

The results show that the proposed algorithm can handle different topologies by splitting and merging contours quite well. Also, the newly developed ROI algorithm can detect the hypoechoic regions with weak or no edges. The results of the novel algorithm are compared with the manual marking of two experts. The results are also compared with the commonly regions, marked by both experts and with those marked by either expert. The proposed algorithm is evaluated by region-based and pixel-based strategies. The evaluation results show that the proposed algorithm produces very good results compared with those of the experts' manual marking. In addition, the proposed algorithm indicates some regions, missed by one expert but confirmed by the other. Therefore, the proposed algorithm can assist the experts in detecting the suspicious abnormal regions that should be considered for biopsy.

Chapter 6

Conclusions and Contributions

6.1 Conclusions

The primary goal of the research, described in this thesis, is to develop a diagnostic tool using ultrasound images for patients with possible prostate cancer. This tool assists radiologists to accurately identify the suspicious regions for biopsies. Radiologists extract the prostate image from the ultrasound image, and mark the abnormal regions that require further testing by conducting biopsies. To assist the radiologist to better identify the cancerous regions in the prostate, the research is divided into two main parts: prostate segmentation and Regions Of Interest (ROI) segmentation.

The manual segmentation of the prostate gland from the TransRectal UltraSound (TRUS) image is time consuming and prone to many drawbacks, including poor accuracy and operator-dependant results. Many algorithms have been developed for prostate segmentation, and most rely on deformable models. To overcome the limitations of the manual segmentation of the prostate from TRUS, two approaches are adopted by researchers namely the semiautomatic segmentation, and the automatic segmentation.

For the semiautomatic algorithms, the operator defines some initial points, usually on the boundary of prostate. There are rules and conditions for selecting these initial points. The semiautomatic algorithm uses these manual initial points to construct the initial contour. Afterward, the algorithm deforms the initial contour to find the boundary of the prostate gland. However, sometimes the contour is attracted to some false edges

instead of the prostate boundary due to the high noise of ultrasound images. Consequently, many researchers have suggested that the initial points should be very close to the prostate boundary. However, even with accurate initial points, some parts of the constructed initial contour are not close enough to prostate boundary. As a result, the contour is attracted to false edges near the prostate boundary. To overcome this problem, some researchers have used manual editing during the segmentation process by stopping the deformation of the contour if the contour is attracted to false edges. Then, the vertices are manually readjusted back to the prostate boundary. This process is labour-intensive since it is repeated as many times as required to find the correct boundary of the prostate. Due to the effort, time and operator-dependency, the semiautomatic segmentation approach is not adopted in this research.

The automatic approach of the prostate segmentation is superior to the previous approach. Constructing the initial contour is the key challenge of this approach. Most automatic algorithms for prostate segmentation depend on the use of manual segmented images as training data. However, such data is not suitable for prostate segmentation, because it is difficult to find a single mean shape that can capture all the variability of the prostate configurations. Consequently, if the mean shape is not close to the prostate boundary of the test image, the contour is attracted to false edges due to ultrasound image noise. Besides, it is difficult to create a large training-data-set in the medical field, especially, if it is created by an expert.

There are two main challenges in prostate segmentation. The first challenge is to find the initial contour of the prostate automatically without using manually segmented images for training purposes. The second challenge is to prevent the contour from being attracted to false edges. The proposed fully automated algorithm for prostate segmentation has overcome these challenges. Existing automatic algorithms are employed to capture the experts' knowledge by using manually segmented images to construct the initial contour. This is a lengthy and often, unsuccessful, process. In this research, experts' knowledge is collected from two radiologists to construct a set of abstract rules which are used during many stages of the proposed prostate segmentation algorithm. The proposed algorithm employs these knowledge-based rules to automatically find a seed point inside the prostate to construct the initial contour. Such rules are far more efficient and effective in handling

difficult images, where the prostate is not in the centre of the image, or the shape of the prostate is skewed and different from the typical shape.

To tackle the second challenge, the proposed automatic algorithm significantly enhances the images by the proposed sequential sticks technique. Besides, more false edges are eliminated by using the constructed knowledge-based rules and morphological operators. Moreover, the proposed prostate segmentation algorithm uses the Gradient Vector Flow (GVF) deformable contour which can segment the prostate gland even if the initial contour is not close to the prostate boundary. All these improvements confirm that the proposed algorithm is more robust against noise. The proposed automatic algorithm is evaluated with respect to the manual outlining by distance-based and area-based metrics. This proposed prostate segmentation algorithm is compared with two well-known semi-automatic algorithms to show its superiority. Hypothesis testing is conducted to prove, with statistical confidence, that the novel algorithm is more accurate and efficient than the other two algorithms. The proposed algorithm is operator-independent, and is capable of accurately segmenting a prostate gland that has any shape and orientation from the ultrasound image. Besides, the proposed prostate segmentation algorithm can be expanded to automatically segment the prostate in 3D ultrasound images.

The goal of the second part of this research is to find the regions of interest (ROI). These ROI are the regions in the prostate glands that can contain specious cancerous areas. A review of research papers on the ROI presents some challenges. The first challenge, some of ROI segmentation techniques, such as graph-theoretic and Gabor filters, generate concentric ring-shaped regions leading to classification confusion which degrades the performance. To overcome this problem, the proposed ROI algorithm generates separate regions; that is, there is no overlap between the generated regions. The second challenge is that the number of abnormal regions of the prostate gland is not known beforehand. Therefore, the problem is transferred into a 3D one by using level set approach. It is capable of segmenting multiple regions with any shapes, and can handle the topology changes by splitting and merging contours. The weak edges of some of the abnormal regions in the prostate gland represent the third challenge. Thus, the proposed ROI algorithm uses one of the most powerful geometric deformable contours called active contours without edges to segment the regions with weak edges or no edges. Fourthly, the limited data size is a problem. The

number of the images marked by radiologists is small, which make it very difficult to use it to train a reliable classifier. To overcome this problem, some researches attempt to adopt most of the data-set as a training data and a small amount of data for testing. However, this leads to overfitting or biasing problems. Therefore, the proposed algorithm depends on knowledge-based rules to avoid the need for any training data. The fifth challenge is notoriously low accuracy of radiologist's marking. Therefore, another radiologist is asked to mark the same set of images, marked by the first radiologist. If any region is missed by one radiologist, the second radiologist might detect it, reducing the false negative regions. The sixth challenge is the long processing time of some ROI algorithms that require to generate a large number of features. Therefore, extensive features generation and selection, which require an extremely long time, are avoided. The seventh challenge is the reliable evaluation of the ROI algorithm. To accurately evaluate the proposed ROI algorithm, a new region evaluation technique is developed.

ROI segmentation's results demonstrate that the proposed ROI algorithm can handle different topologies quite well by splitting and merging the contours. Beside, the proposed algorithm can extract the hypoechoic regions with weak or no edges. The proposed algorithm results have been compared with those of two experts' manual marking. Then, the results are compared with the common regions that are marked by both experts and with the total regions which are marked by either expert. The proposed algorithm is evaluated by applying region-based and pixel-based strategies. The evaluation results indicate that the proposed algorithm yields similar results, if it is compared with the experts' markings, but with the added advantages of being, fast and reliable.

The proposed algorithm also detects some regions, missed by one expert but confirmed by the other. Therefore, the proposed algorithm is proven to assist the experts in accurately selecting biopsy sites.

6.2 Contributions

In this research, a diagnostic tool is developed and applied to ultrasound images for patients with possible prostate cancer. This assistive tool leads to early detection, proper management and most likely reducing the mortality rate related to this disease. As dis-

cussed before, the diagnostic algorithm developed in this research consists of prostate segmentation and Regions Of Interest (ROI) segmentation.

The contributions of the proposed prostate segmentation algorithm are summarized.

- It is fully automatic.
 - It is by large operator-independent. It does not require any initial points to be defined manually or any further manual editing. This will speed up the segmentation process.
 - It does not require any training data.
 - It overcomes the difficulty of determine the single mean shape which represents the large variability of the prostate shape.
 - It uses all the available data for the testing phase. This will prevent the drawback of generating the biased results which are common when most of the data are used for training and few data are used for the testing.
 - It overcomes the scarcity of the training data sets in the medical field, especially, if it evolves experts input.
- It is accurate.
 - The proposed algorithm is compared with two other well-known semi-automatic algorithms (Ladak's, Pathak's algorithms), which were used in the thesis as benchmark. Also it is confirmed, with statistical confidence, that the novel prostate segmentation algorithm is superior to the other two algorithms (see Section 4.5.3, p. 76).
 - It prevents the contour from being attracted to false edges.
- It is capable of segmenting various prostate shapes (see Figures 4.8–4.10, pp. 70–72) because the algorithm does assume any preset prostate model to start from.
- It uses the proposed sequential sticks technique with variables length instead of sticks filter with a fixed length which enables the algorithm to generate a more accurate edge map by enhancing the small details of the prostate boundary and reducing the

noise. A comparison study indicates a significant improvement in the edge map by applying the proposed method (see Figure 4.4, p. 59).

The contributions of the proposed ROI segmentation algorithm are also summarized.

- The proposed ROI algorithm is based on knowledge-based rules to avoid the use of any training data.
- It is accurate because of the following.
 - It does not generate any overlapped regions.
 - It can eliminate the regions that are less likely to exhibit prostate cancer (see Section 5.4.4, p. 93).
 - It is capable of segmenting suspected regions that have weak edges or even no edges because the segmentation process depends on the region properties and not on the edges.
 - It can handle the topology changes through splitting and merging the contours (see Figure 5.7, p. 96).
- It does not require the identification of the number of regions beforehand.
- The initial contour is generated by the proposed algorithm without any manual initial points (see Section 5.4.3.1, p. 87).
- A new region evaluation technique is devised to accurately evaluate the proposed ROI algorithm (see Section 5.6.1, p. 105).
- It is fast because extensive features generation and selection, which require an extremely long time, are avoided.

6.3 Future Work

This thesis describes a diagnostic tool to automatically segment the prostate gland from ultrasound images and find the abnormal regions of the prostate that are suspected to have

prostate cancer. A number of research projects can be investigated to extend this research work:

- Incorporate clinical data such as Prostate Specific Antigen (PSA) blood level, PSA density, PSA Velocity, age Specific PSA, free to total PSA, prostate volume, patient age, digital rectal examination, and family history in the algorithms to further improve the diagnosing process. Moreover, it integrates the biopsy results with the radiologist's marking as a gold standard in order to better evaluate the proposed algorithms.
- Extend the work to MRI and other imaging modalities.
- Use data fusion of two or more imaging modalities to further improve the diagnosing of prostate cancer.
- Extend the work to other types of cancer such as breast and lung cancer.
- Obtain a large data set to be able to apply multi-classification techniques such as classifiers fusion and selection.

Appendix A

Ultrasound Characteristics

A.1 Introduction

Ultrasound is an acoustic wave like the infrasound, sound, and hypersound wave. Their differences are not in their characteristics but in their frequency ranges. The infrasound frequency range is between 0 to 20 Hz. The sound that can be detected by the human ear is (20 Hz – 20 KHz). Typically, the ultrasound frequency range is between 20 KHz and 30 MHz, whereas the hypersound frequency is above 1 GHz. Ultrasound is like any acoustic wave; it needs a medium to propagate in because it can not exist in a vacuum [146].

Since 1950, ultrasound diagnostic equipment has been available but its applications have been very limited. The transducers worked at low frequencies, the resolution was inadequate, and the format of the ultrasound images was black and white "bi-stable". In 1972, Kossoff developed grey scale displays. The transducers' capabilities were later improved, enabling operation at different high frequencies. Also, the transducers' shapes and volumes were improved. The small size of instrument facilitated its insertion into such areas as arteries, ureters. [147, 148]. The most noticeable advantages of ultrasound follow [149].

- is safe
- is cost effective
- can provides useful information about the velocity and flow of the blood

- enables working in real time
- controls resolution of the images by frequency
- is easy to handle

A.2 Fundamentals of Ultrasound

Piezoelectrical crystals transform electrical energy into acoustic energy, and vice versa. Consequently, piezoelectrical crystals play a principal role in producing ultrasound. Ultrasound behaves like radar and the transducer produces pulses that can penetrate the human body. After the organ reflects these pulses, the transducer detects the echoes. The time interval between emitting the pulse and receiving it is twice the time needed for the pulse to reach the organ. The distance between the transducer and the reflector is calculated by multiplying half of time interval between emitting and receiving the pulse, and the ultrasound velocity. Therefore, an anatomical image can be obtained by ultrasound [146, 150].

When ultrasound propagates in a medium, it produces disturbances in this medium such as pressure, temperature, density, medium velocity, and medium displacement. A sinusoidal acoustic wave is shown in Figure A.1 [149], where λ is the wavelength with a unit of m , and T is the time period in s .

A.2.1 Attenuation of Ultrasound

When ultrasound penetrates a medium such as tissue, its intensity is reduced due to [146].

1. Divergence
2. Reflection
3. Scattering
4. Absorption
5. Refraction

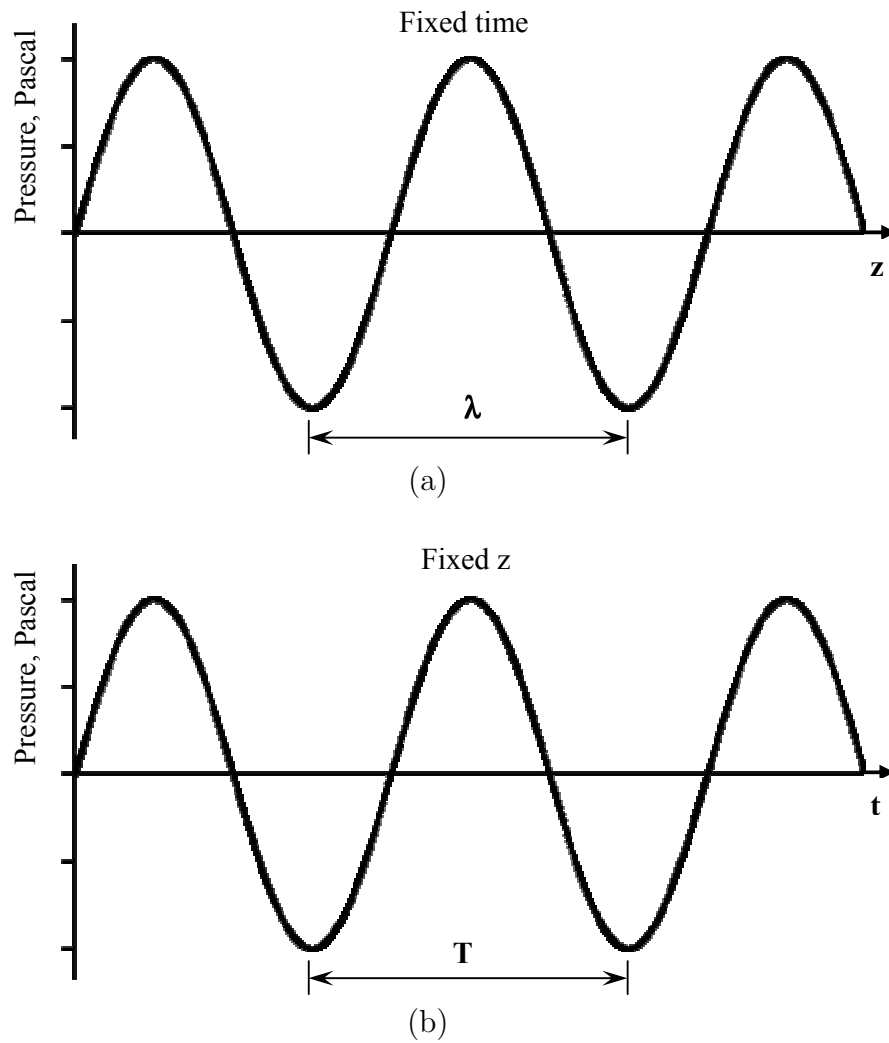


Figure A.1: Sinusoidal acoustic wave propagation as a function of (a) space at a fixed time and (b) time at a fixed distance z

A.2.1.1 Divergence

It occurs in a non-focused ultrasound beam. As a result, the beam becomes diverted in other directions [149].

A.2.1.2 Reflection

When the wave encounters a discontinuity in the acoustic, such as at the interface of two different media, part of the ultrasound beam is reflected back to the incident medium by the same velocity, as shown in Figure A.2 [146].

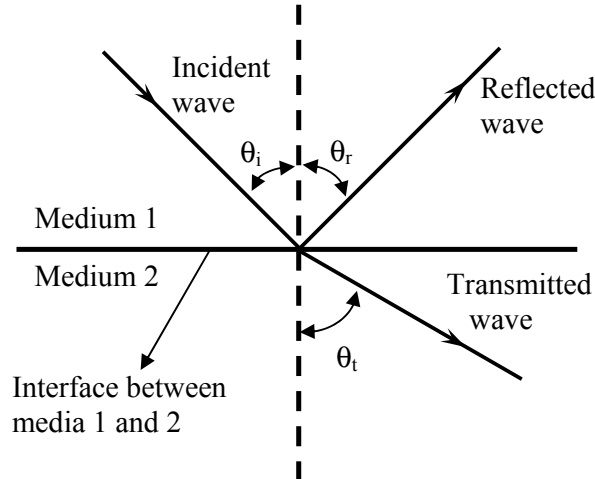


Figure A.2: Reflection and refraction of ultrasonic waves

A.2.1.3 Scattering

If the surface of the medium, which the ultrasound beam is incident on, is at least several wave lengths, the beam is reflected. On the contrary, if the surface dimensions are smaller, the incident beam is reflected in all directions and is scattered [146].

A.2.1.4 Absorption

When the ultrasonic beam penetrates a tissue, part of the ultrasonic energy is absorbed by the tissue and converted into heat [149].

A.2.1.5 Refraction

When an ultrasonic beam is incident on a medium, part of this beam is reflected, and the rest of it is transmitted or refracted into the medium with a velocity corresponding to that medium [146].

A.2.2 Doppler Effect

Ultrasound is relied on for measuring the flow velocity by using the means of Doppler effect. When the ultrasound beam is reflected by a moving target whose velocity has a component in the direction of the beam, the frequency of the reflected beam is higher, as the target moves away from it. The Doppler frequency shift is in the audible range for medical ultrasound frequencies. If extracted properly, it can be heard by a loud speaker. Figure A.3 illustrates a method of measuring blood flow velocity [149].

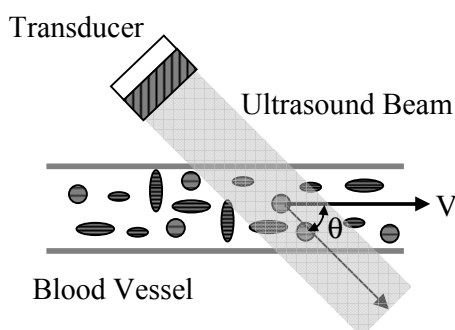


Figure A.3: Measuring blood flow velocity by ultrasound

A.3 Diagnostic Ultrasonic Imaging

There are various modes for displaying ultrasound images: A-, B-, C- and M- modes. A, B, C and M are referred to Amplitude, Brightness, Constant depth and Motion, respectively. The most common mode is the brightness mode, B. Figure A.4 depicts the A- and B- mode images [149].

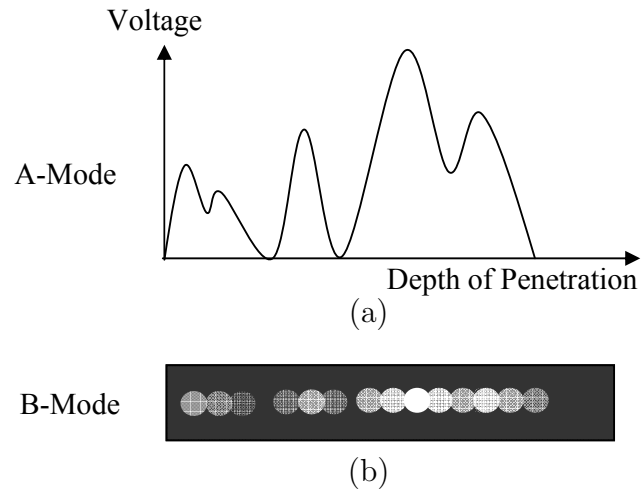


Figure A.4: (a) A-mode: echo amplitude is displayed as a function of the depth of penetration and (b) B-mode: the echo amplitude is represented by the grey or brightness level

A.3.1 Transducers

When certain crystals are placed under pressure or mechanical stress, an electrical potential appears on their surfaces. This is called the piezoelectric effect. Some substances have been developed which exhibit this effect. They include lead zirconate titanate, lead metaniobate, and barium titanate. The most satisfactory substance, at frequencies as high as 10MHz, is lead zirconate titanate [146]. A single element transducer consisting of a circular disc, two matching layers, a lens, and backing material is signified in Figure A.5 [149].

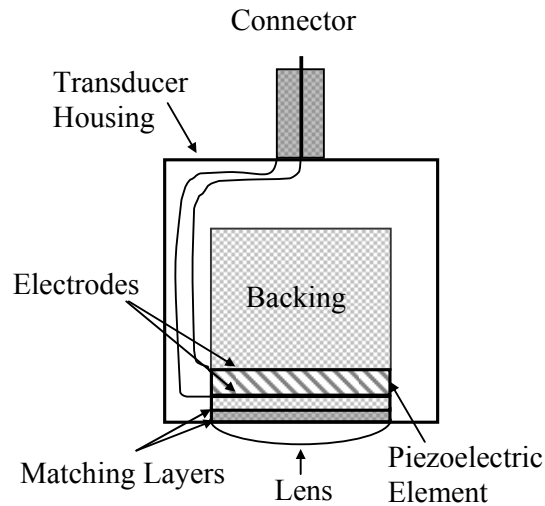


Figure A.5: Construction of a single-element ultrasonic transducer

A.3.2 A-Mode and B-Mode

Figure A.6 is a block diagram for an A-mode ultrasound instrument [149]. It contains a single transducer which transmits the ultrasound pulses and receives the echoes. Then, the echoes are displayed on an image to yield information about the distance and the strength of the signals [146].

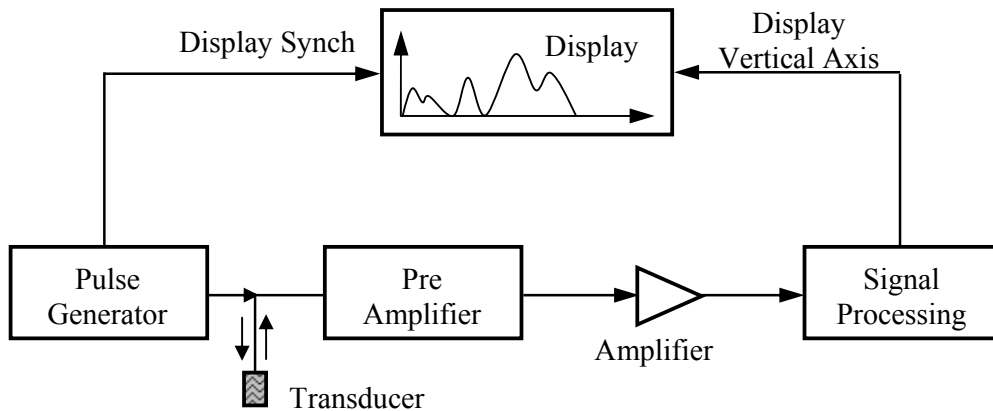


Figure A.6: Block diagram of an A-mode instrument

In brightness mode, the strength of the signals is converted into an intensity level of

grey colours [146]. The block diagram of the B-mode ultrasound instrument is shown in Figure A.7 [149].

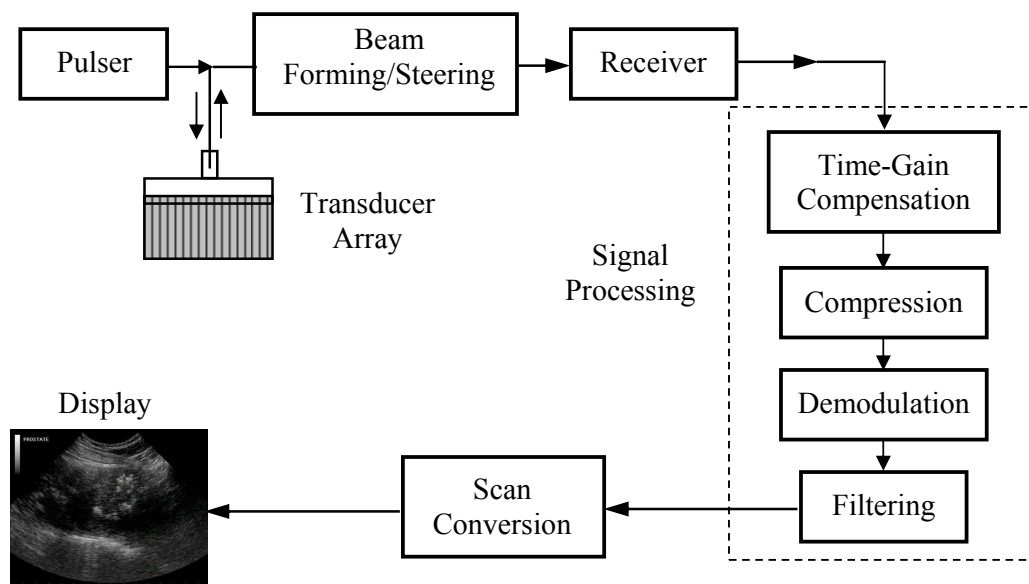


Figure A.7: Block diagram of a B-mode ultrasonic imaging system

A.3.3 M-Mode and C-Mode imaging

If an A- or B-mode signal is moving across the monitor as a function of time, the display is called the M-mode. It is used to display the motion of the organs inside the human body (e.g., heart). The C-mode imaging acts like radar. A second transducer is needed to detect the ultrasound waves after propagation in an object, and then displays a 2D map of the object [149].

A.3.4 Doppler Methods for Flow Measurement

There are two types of flow measuring. The first is the Continuous Wave (CW) Doppler as depicted in Figure A.8. The second is the Pulsed Wave (PW) Doppler in Figure A.9. The drawback of the CW is that it cannot differentiate between the origins of the Doppler signals, produced in the ultrasound beam. That is why, PW is preferable to CW [149].

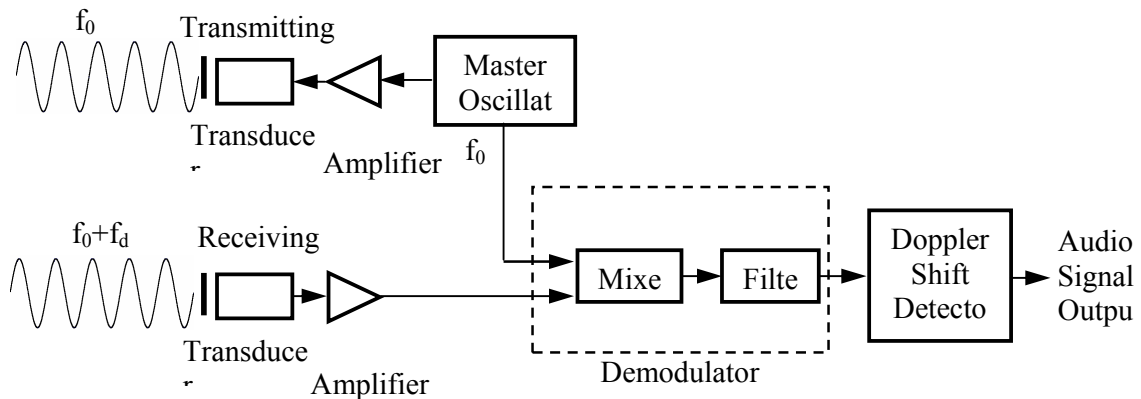


Figure A.8: Block diagram of a CW Doppler flow metre

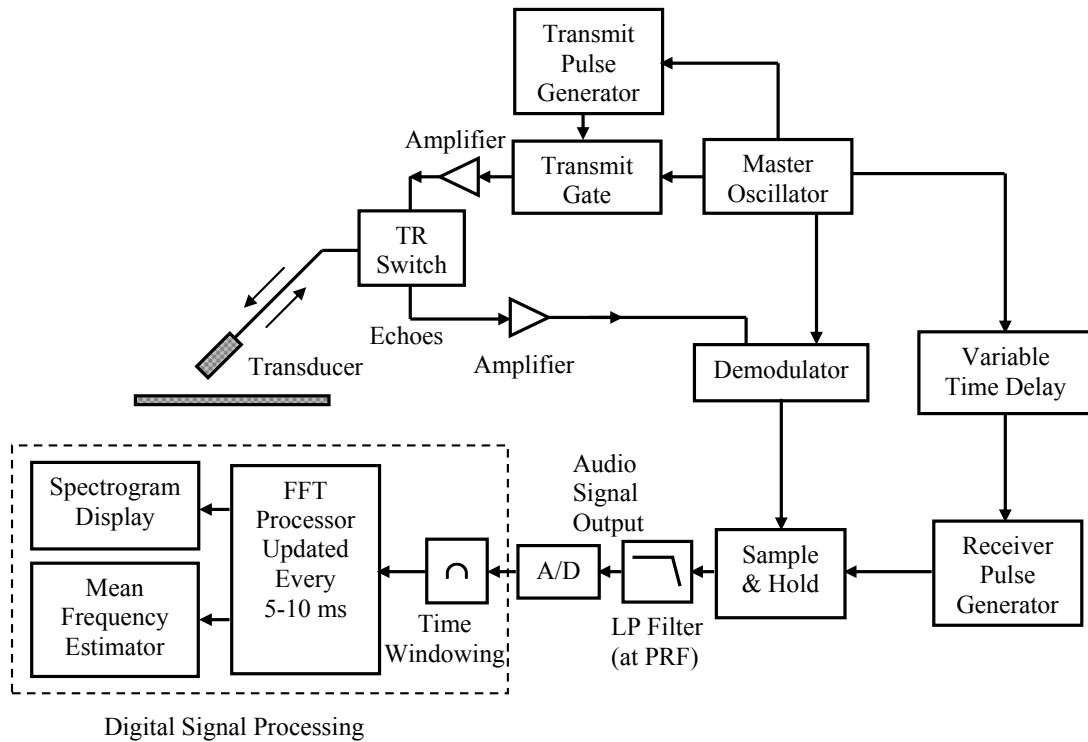


Figure A.9: The block diagram of a pulsed Doppler system

A.3.5 Colour Doppler Flow Imaging

This type of imaging displays the coloured Doppler flow image superimposed on the grey level B mode image in real time. This imaging technique is very useful because it gives

anatomical image and also the blood flow information in a clear and coloured presentation.

A.4 Summary

Ultrasound imaging has improved significantly over the years. It has evolved from the radar used by the Navy to detect submarines to a myriad of applications in industry, medicine and even in homes. It is the medical applications of ultrasound that is the driving force, not only for diagnoses, but also the treatment of diseases.

Appendix B

One Tailed Hypothesis Testing

The procedure of a one-tailed hypothesis testing about the means of two independent samples is summarized as follows [138]:

1. State the null and alternative hypotheses:

the null hypothesis $H_0 : \mu_1 - \mu_2 = 0$

and

the alternative hypothesis $H_1 : \mu_1 - \mu_2 > 0$,

where: μ_1 and μ_2 are the means of the first and the second populations, respectively.

2. Calculate the mean and the standard of each sample by using the following formulas:

$$\text{Mean of a sample} = \bar{x} = \frac{\sum x_i}{n} \quad (\text{B.1})$$

and

$$\text{Standard deviation of a sample} = s = \sqrt{\frac{\sum x_i^2 - \frac{(\sum x_i)^2}{n}}{n-1}}, \quad (\text{B.2})$$

where:

n is the number of observations in the sample

and

x is the i^{th} value of the variable x .

3. Calculate the standard error of the difference between the two means as follows:

$$s_{\bar{x}_1 - \bar{x}_2} = \sqrt{s_p^2 \left(\frac{1}{n_1} + \frac{1}{n_2} \right)} \quad (\text{B.3})$$

where

n_1 and n_2 are the number of observations in the first and second sample, respectively
 S_p is the pooled variance and is given by

$$s_p^2 = \frac{(n_1 - 1)s_1^2 + (n_2 - 1)s_2^2}{n_1 + n_2 - 2} \quad (\text{B.4})$$

where

s_1 and s_2 are the standard deviations of the first and second sample, respectively

4. Evaluate the observed value of the difference between the two means by using statistical t such that

$$t_{obs} = \frac{\bar{x}_1 - \bar{x}_2}{s_{\bar{x}_1 - \bar{x}_2}} \quad (\text{B.5})$$

5. Find the critical value of t (t_{cv}). This value can be found from one-tailed t-statistical tables by using the degree of freedom df and the level of significance α . The most common significance levels are 0.05 or 0.01 whereas df is calculated by

$$df = n_1 + n_2 - 2. \quad (\text{B.6})$$

6. Decide whether to reject H_0 . If the observed value of the t statistical test falls in the rejection region, as displayed in Figure B.1, the null hypothesis is rejected and the alternative hypothesis is supported. Otherwise, there is not enough evidence to reject the null hypothesis or to support the alternative hypothesis.

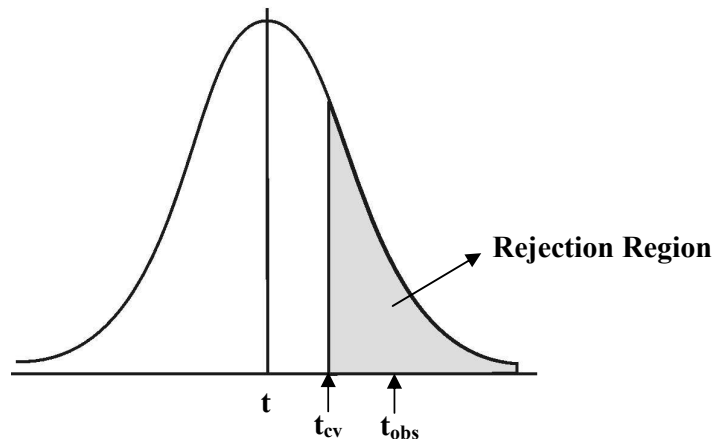


Figure B.1: t statistic test

Appendix C

ROI Algorithm Results

Figure C.1 – Figure C.8 show some results of the ROI proposed algorithm developed in Chapter 5. In these figures, the results of the proposed ROI algorithm are displayed in row (a). Rows (b) and (c) show the manual marking of the two experts. The common regions of the two experts "AND" are displayed in row (d), and the total marked regions by the two experts "OR" are shown in row (e).

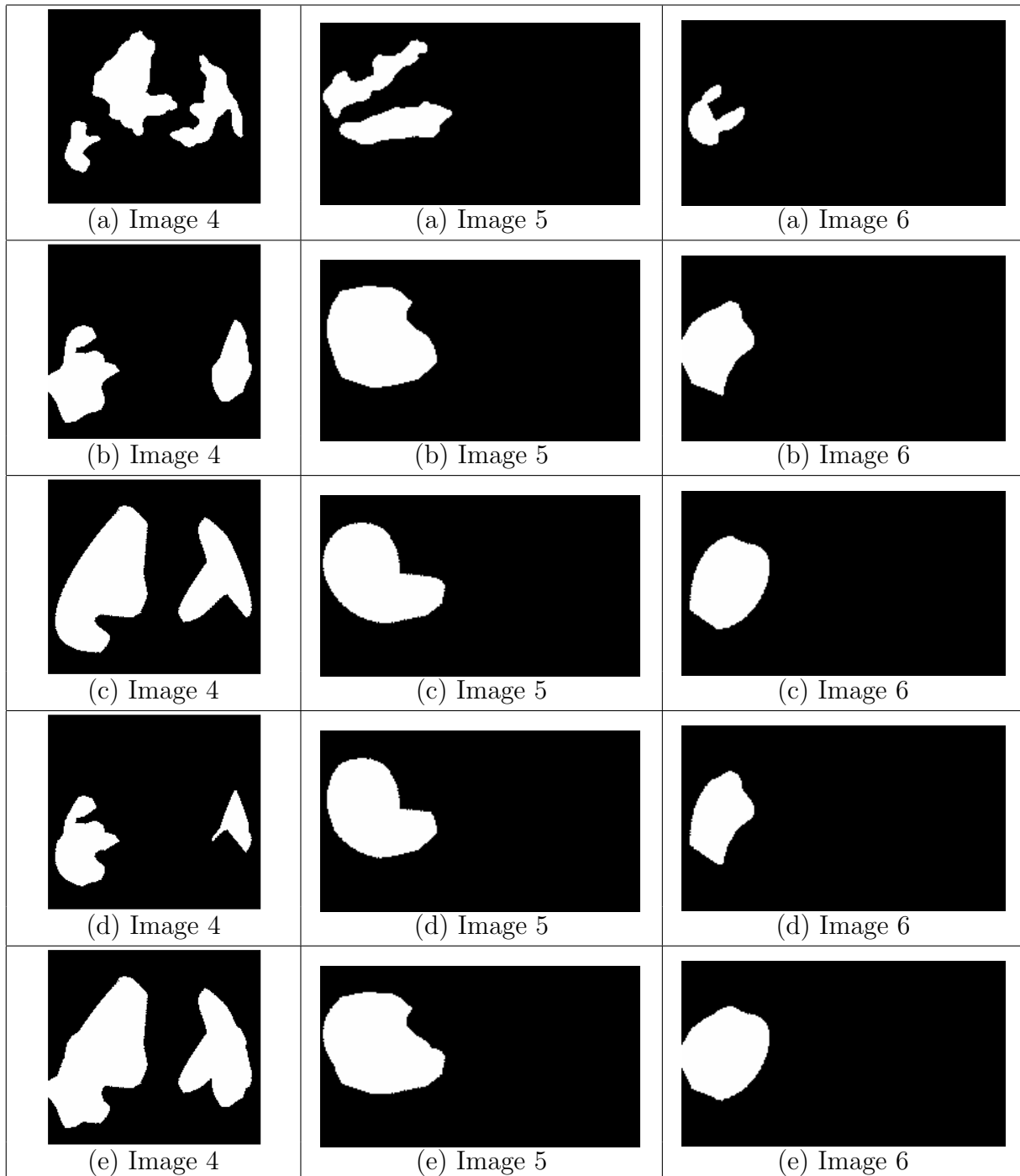


Figure C.1: (a) ROI algorithm results, (b) manual marking of the first expert (c) manual marking of the second expert, (d) shared regions marked by both experts (AND), and (e) the total regions marked by both experts (OR)

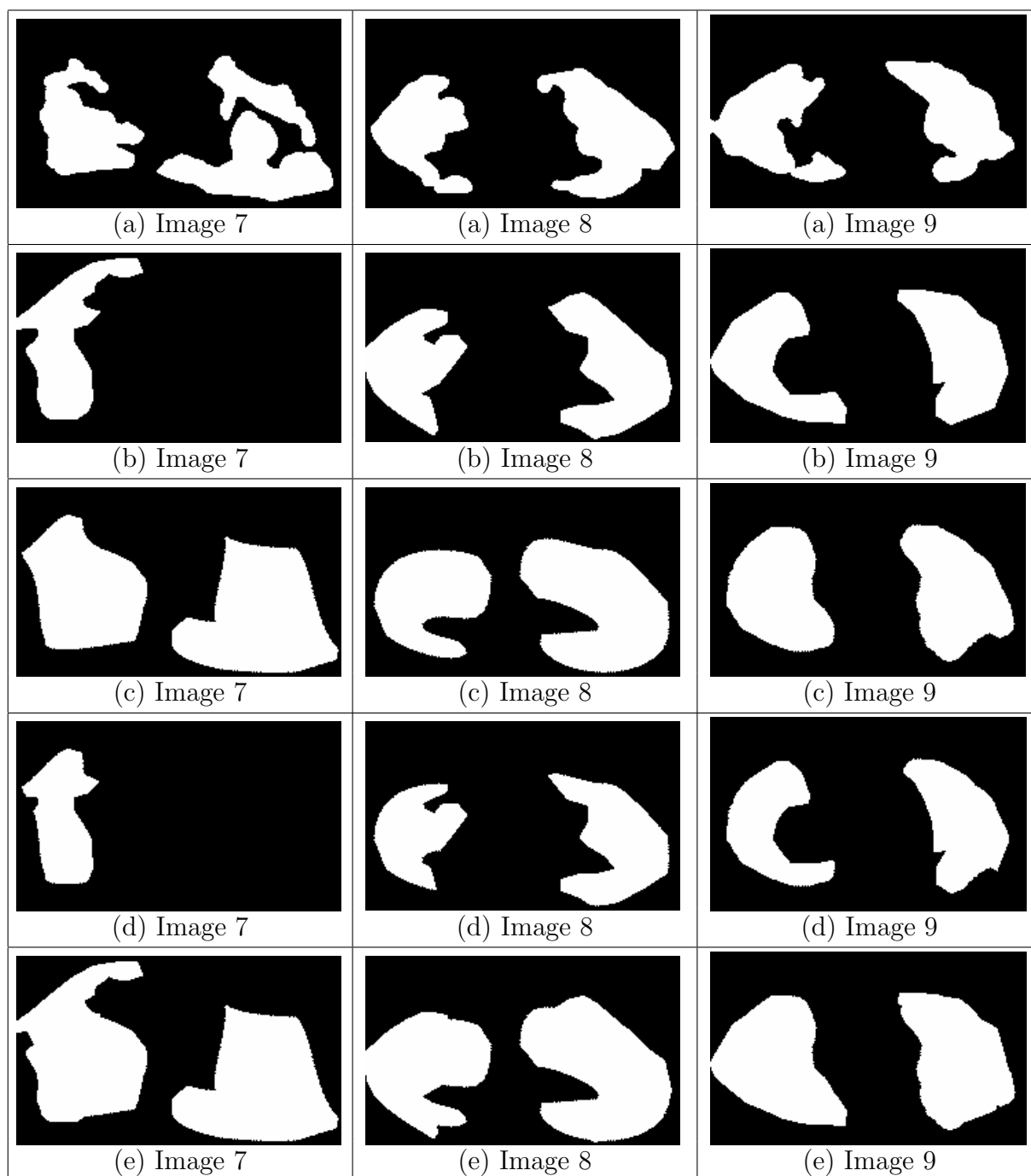


Figure C.2: (a) ROI algorithm results, (b) manual marking of the first expert (c) manual marking of the second expert, (d) shared regions marked by both experts (AND), and (e) the total regions marked by both experts (OR)

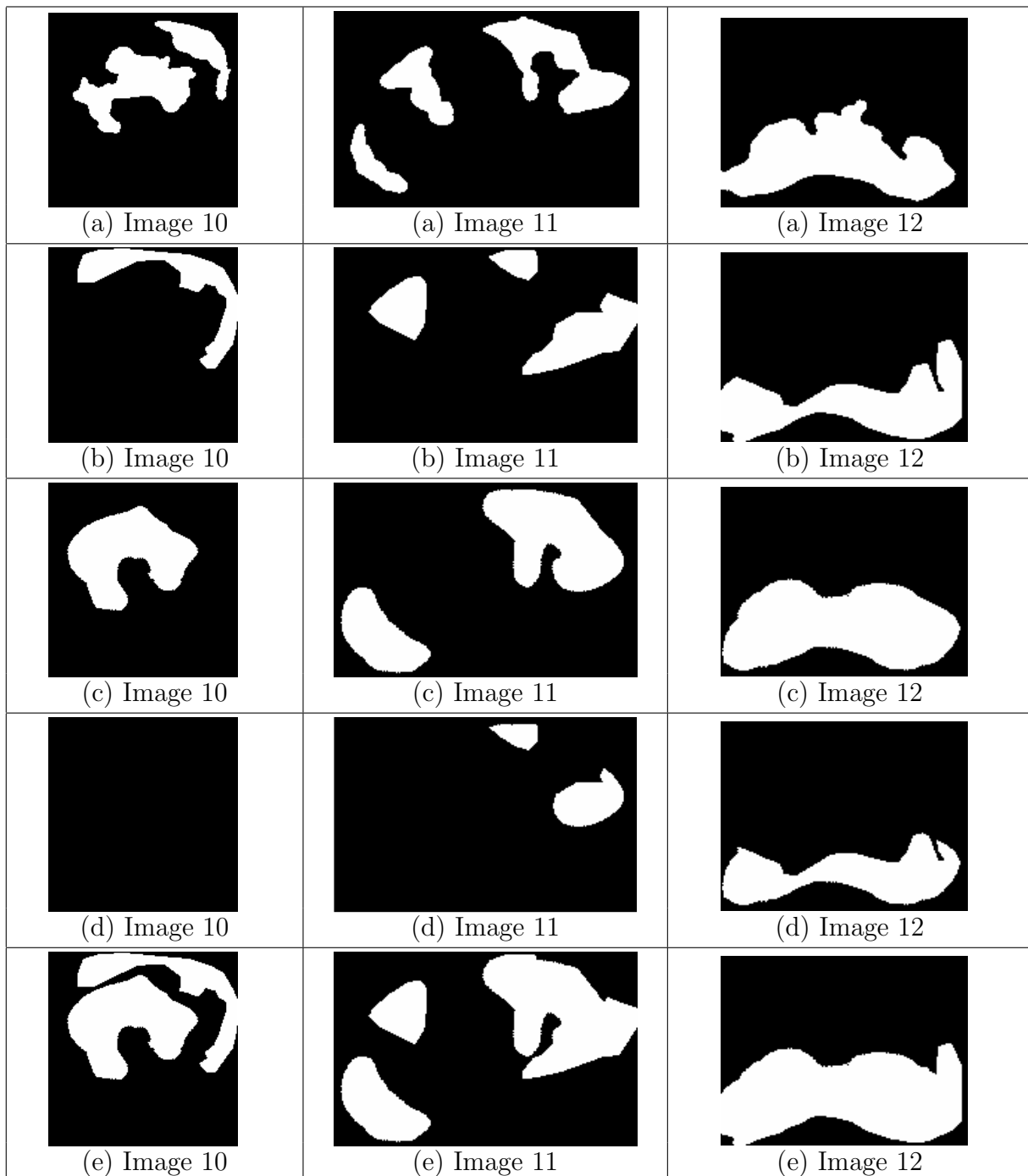


Figure C.3: (a) ROI algorithm results, (b) manual marking of the first expert (c) manual marking of the second expert, (d) shared regions marked by both experts (AND), and (e) the total regions marked by both experts (OR)

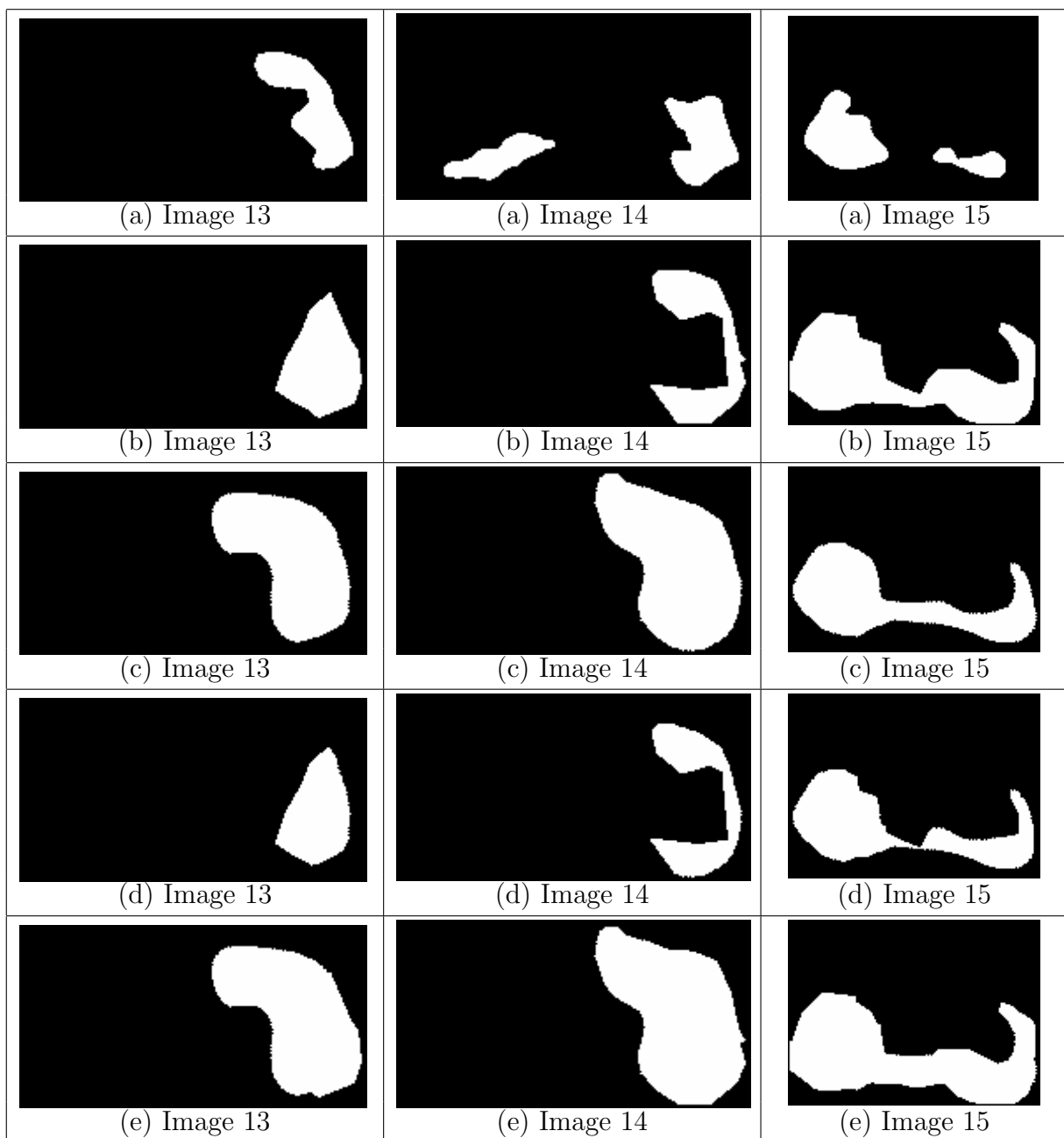


Figure C.4: (a) ROI algorithm results, (b) manual marking of the first expert (c) manual marking of the second expert, (d) shared regions marked by both experts (AND), and (e) the total regions marked by both experts (OR)

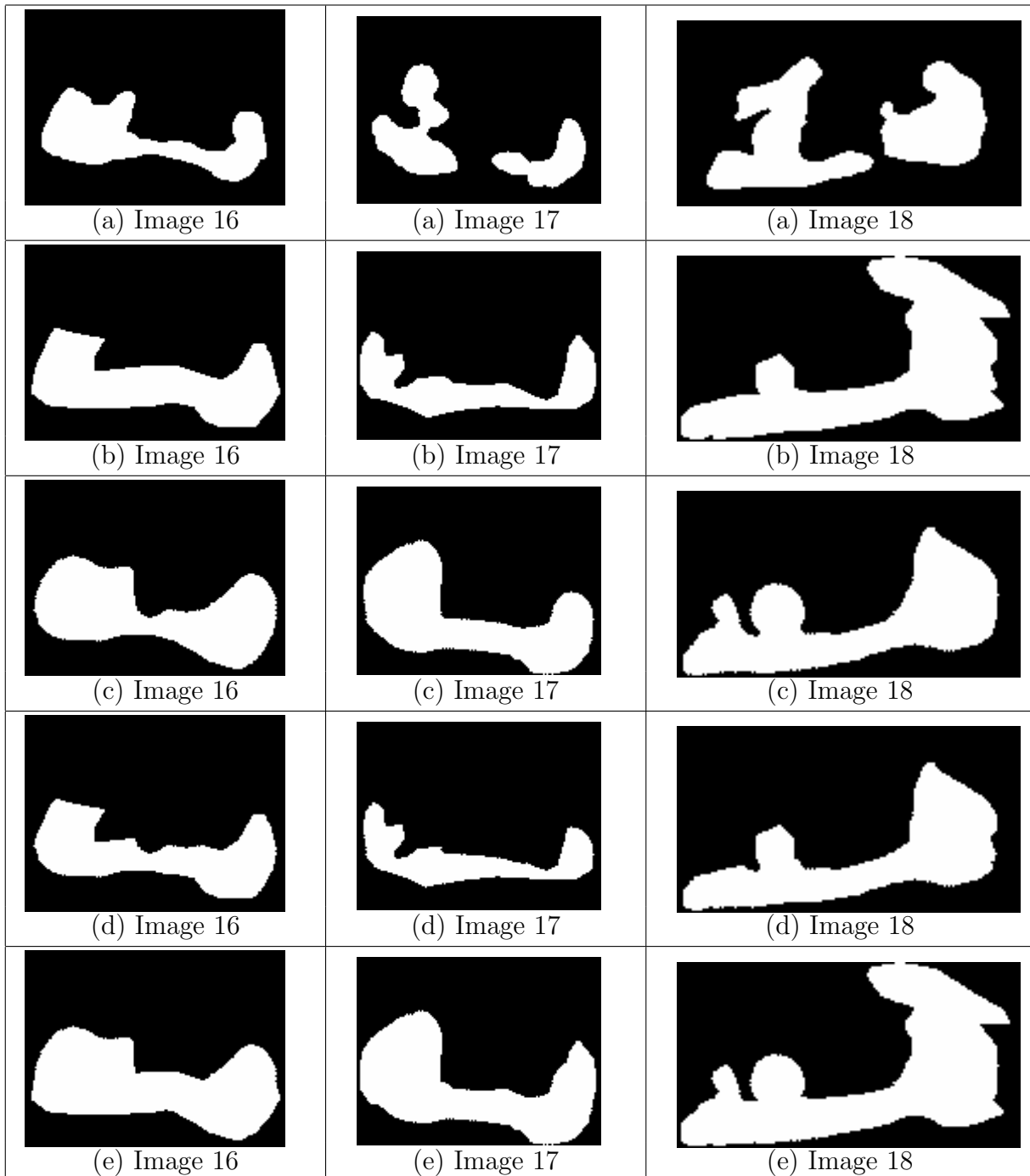


Figure C.5: (a) ROI algorithm results, (b) manual marking of the first expert (c) manual marking of the second expert, (d) shared regions marked by both experts (AND), and (e) the total regions marked by both experts (OR)

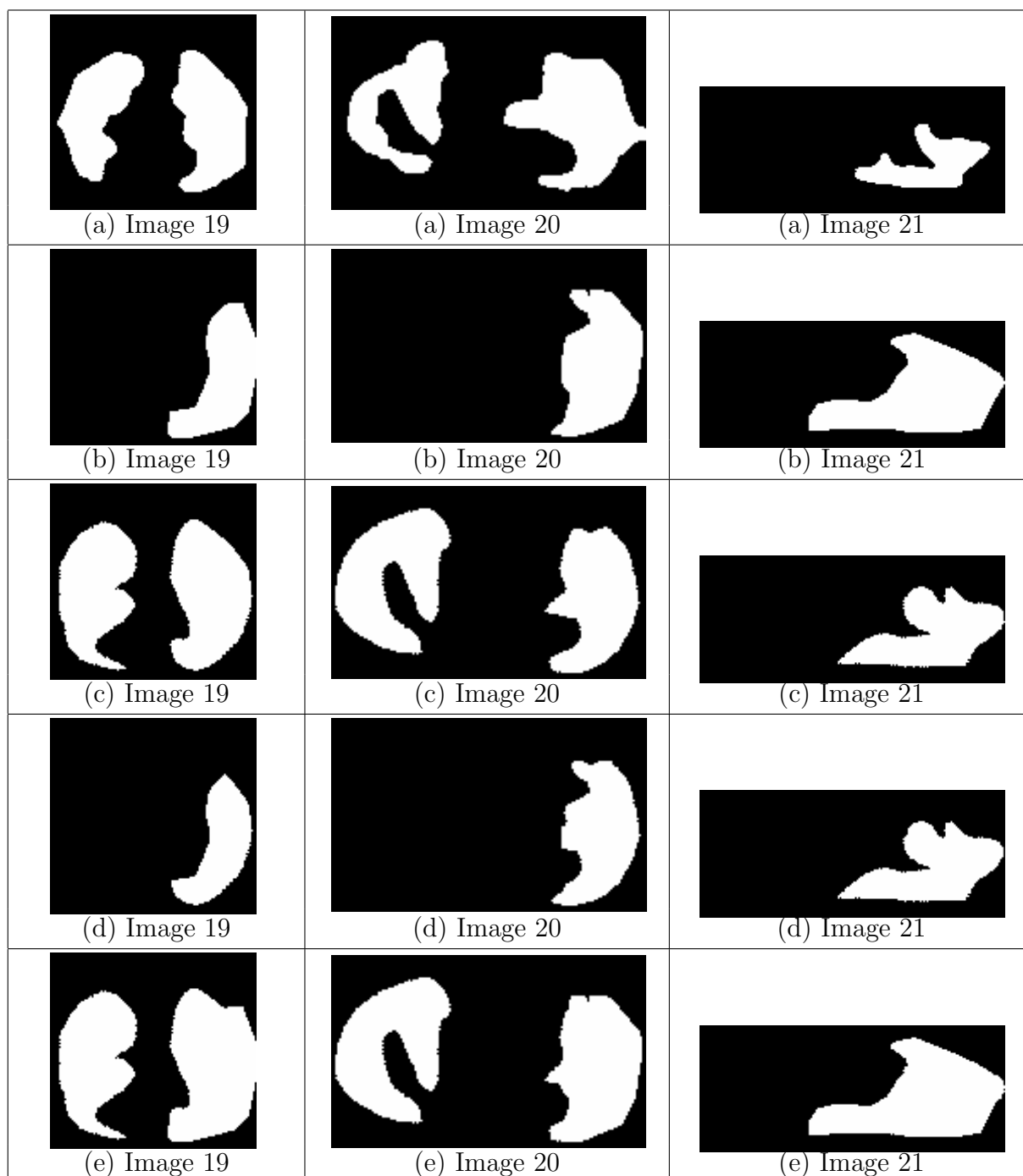


Figure C.6: (a) ROI algorithm results, (b) manual marking of the first expert (c) manual marking of the second expert, (d) shared regions marked by both experts (AND), and (e) the total regions marked by both experts (OR)

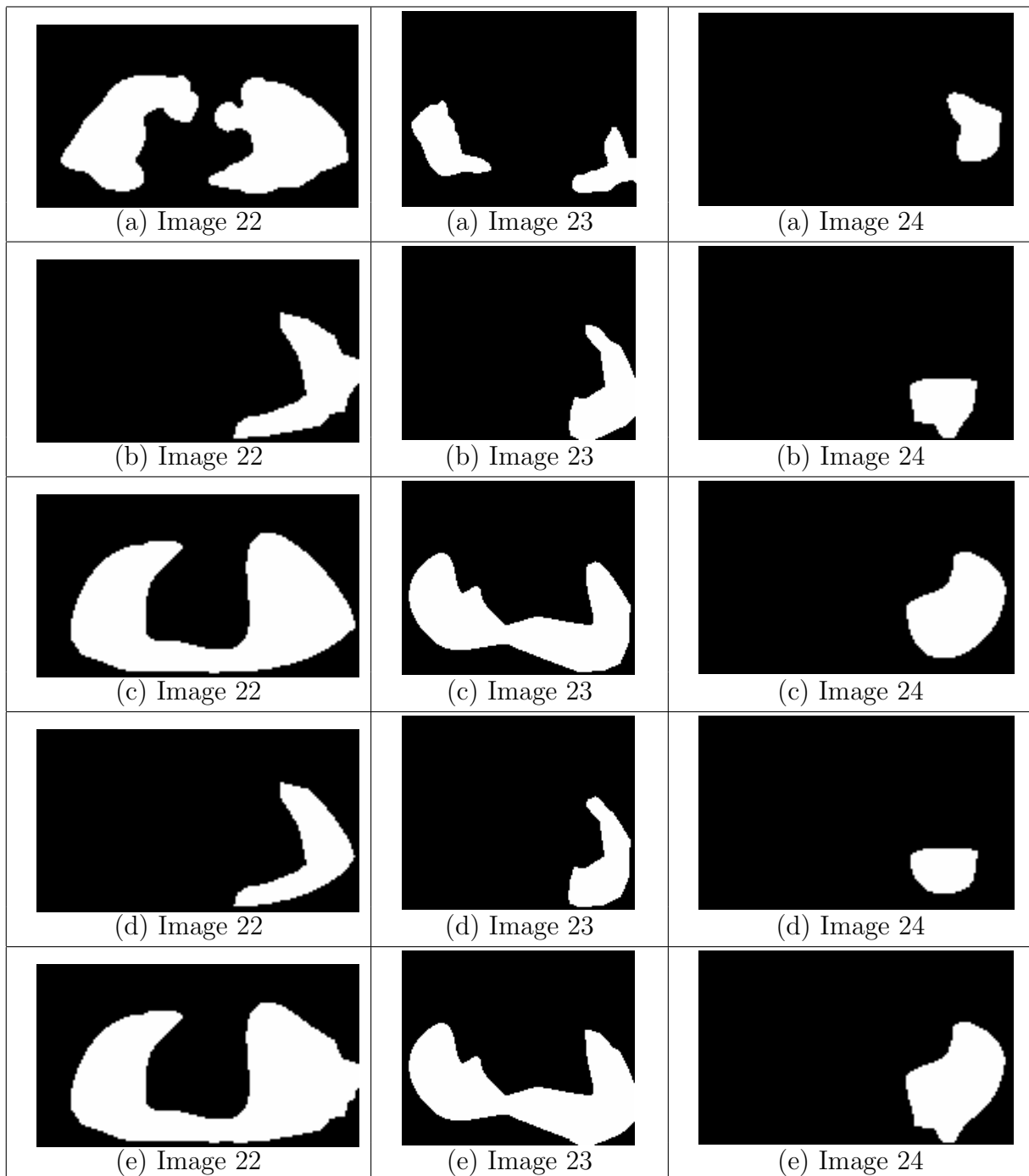


Figure C.7: (a) ROI algorithm results, (b) manual marking of the first expert (c) manual marking of the second expert, (d) shared regions marked by both experts (AND), and (e) the total regions marked by both experts (OR)

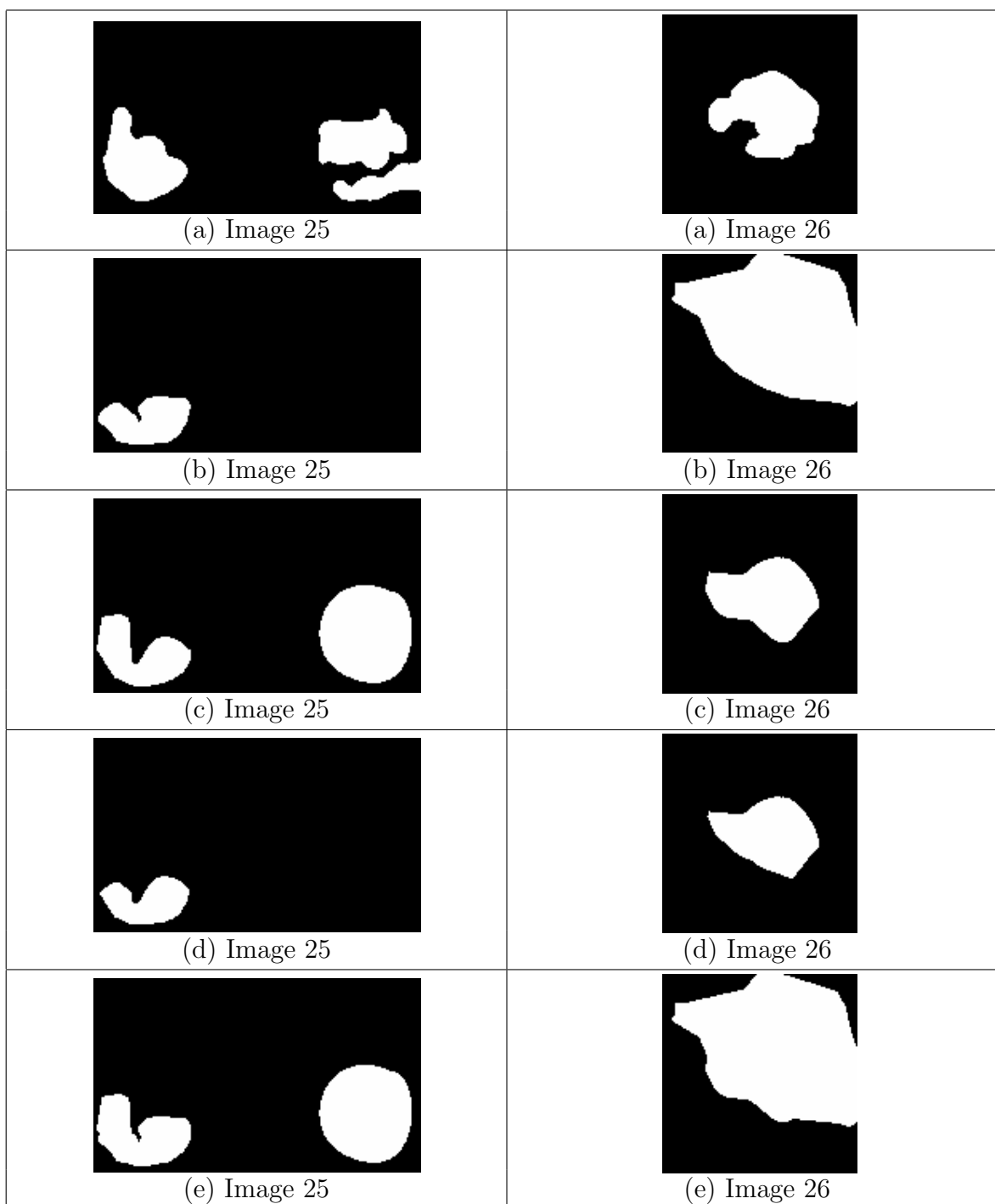


Figure C.8: (a) ROI algorithm results, (b) manual marking of the first expert (c) manual marking of the second expert, (d) shared regions marked by both experts (AND), and (e) the total regions marked by both experts (OR)

Bibliography

- [1] Canadian Cancer Society, "National Cancer Institute of Canada: Canadian Cancer Statistics 2006," February 2007; <http://www.cancer.ca>.
- [2] M. D. A. Tewari, *Prostate Cancer: A Step-by-Step Interactive Monogram*, CD-ROM, Macromedia Interactivity and Medical Illustration, 1998.
- [3] M. Garraway, *Epidemiology of Prostate Disease*, New York: Springer-Verlag, 1995.
- [4] J. B. Mason and G. Nitenberg, *Cancer & Nutrition: Prevention and Treatment*, Vevey: Nestlé Nutrition, 2000.
- [5] J. F. Holland, E. Frei, R. C. Bast, D. W. Kufe, D. L. Morton, and R. R. Weichselbaum, *Cancer Medicine*, 3rd ed., Vol. 2, Philadelphia: Lea & Febiger, 1993.
- [6] L. A. Eskew, R. L. Bare, and D. L. Mccullough, "Systematic 5 Region Prostate Biopsy is Superior to Sextant Method for Diagnosing Carcinoma of the Prostate," *Journal of Urology*, vol. 157, January 1997, pp. 199-203.
- [7] R. H. Young, J. R. Srigley, M. B. Amin, T. M. Ulbright, and A. L. Cubilla, *Atlas of Tumor Pathology: Tumors of the Prostate Gland, Seminal Vesicles, Male Urethra, and Penis*, Washington, D.C.: Armed Forces Institute of Pathology, 2000.
- [8] D. L. Pham, C. Xu, and J. L. Prince, "Current Methods in Medical Image Segmentation," *Annual Review of Biomedical Engineering*, vol. 2, August 2000, pp. 315-338.

- [9] A. C. Bovik, "On Detecting Edges in Speckle Imagery," *IEEE Transactions on Acoustics, Speech, and Signal Processing*, vol. 36, no. 10, October 1988, pp.1618-1627.
- [10] P. K. Sahoo, A. A. Farag, and Y. P. Yeap, "Threshold Selection Based on Histogram Modeling," *IEEE International Conference on Systems, Man and Cybernetics*, vol.1, October 1992, pp. 351-356.
- [11] M. Sezgin and B. Sankur, "Survey over Image Thresholding Techniques and Quantitative Performance Evaluation," *Journal of Electronic Imaging*, vol.13, no.1, January 2004, pp. 146-165.
- [12] S. U. Le, S. Y. Chung, and R. H. Park, "A Comparative Performance Study of Several Global Thresholding Techniques for Segmentation," *Graphical Models and Image Processing*, vol. 52, no.2, November 1990, pp.171-190.
- [13] P. K. Sahoo, S. Soltani, A. K. C. Wong, and Y. Chen, "A Survey of Thresholding Techniques," *Computer Vision, Graphics and Image Processing*, vol. 41, no.2, February 1988, pp. 233-260.
- [14] C. A. Glasbey, "An Analysis of Histogram-Based Thresholding Algorithms," *Graphical Models and Image Processing*, vol. 55, no. 6, November 1993, pp. 532-537.
- [15] J. S. Weszka and A. Rosenfeld, "Threshold Evaluation Techniques," *IEEE Transactions on Systems, Man and Cybernetics*, vol. 8, August 1978, pp. 622-629.
- [16] P. W. Palumbo, P. Swaminathan, and S. N. Srihari, "Document Image Binarization: Evaluation of Algorithms," *Proceedings SPIE, Applications of Digital Image Processing IX*, vol. 697, August 1986, pp. 278-285.
- [17] O. D. Trier and A. K. Jain, "Goal-Directed Evaluation of Binarization Methods," *IEEE Transaction on Pattern Analysis and Machine Intelligence*, vol. 17, no. 12, December 1995, pp. 1191-1201.

- [18] Y. Zimmer, R. Tepper, and S. Akselrod, "Two Dimensional Extension of Minimum Cross Entropy Thresholding for the Segmentation of Ultrasound Images," *Ultrasound in Medicine and Biology*, vol. 22, no. 9, 1996, pp.1183-1190.
- [19] A. K. C. Wong and P. K. Sahoo, "A Gray-Level Threshold Selection Method Based on Maximum Entropy Principle," *IEEE International Conference on Systems, Man and Cybernetics*, vol. 19, no. 4, July-August 1989, pp. 866-871.
- [20] S. D. Pathak, P. D. Grimm, V. Chalana, and Y. Kim, "Pubic Arch Detection in Transrectal Ultrasound Guided Prostate Cancer Therapy," *IEEE Transactions on Medical Imaging*, vol. 17, no. 5, October 1998, pp. 762-771.
- [21] B. Potocnik and D. Zazula, "Automated Analysis of a Sequence of Ovarian Ultrasound Images, Part I: Segmentation of Single 2D Images," *Image and Vision Computing*, vol. 20, no. 3, March 2002, pp. 217-225.
- [22] H. R. Singleton "Automatic Image Segmentation Using Edge Detection by Tissue Classification in Local Neighborhoods," *IEEE Proceedings Southeastcon '92*, vol. 1, April 1992, pp. 286-290.
- [23] B. Potocnik, D. Zazula, and F. Solina, "Classical Image Processing vs. Computer Vision Techniques in Automated Computer-Assisted Detection of Follicles in Ultrasound Images of Ovary," *6th International Conference on Image Processing and its Applications*, vol. 2, July 1997, pp. 551-555.
- [24] C. Lee, S. Huh, T. A. Ketter, and M. Unser, "Unsupervised Connectivity-Based Thresholding Segmentation of Midsagittal Brain MR Images," *Computers in Biology and Medicine*, vol. 28, no. 3, May 1998, pp. 309-338.
- [25] M. D. G. Montoya, C. Gil, and I. García, "The Load Unbalancing Problem for Region Growing Image Segmentation Algorithms," *Journal of Parallel and Distributed Computing*, vol. 63, no. 4, April 2003, pp. 387-395.
- [26] J. C. Tilton, "Image Segmentation by Iterative Parallel Region Growing and Splitting," *12th Canadian Symposium on Remote Sensing, Geoscience and Remote Sensing Symposium (IGARSS'89)*, vol. 4, July 1989, pp. 2420-2423.

- [27] N. Coptý, S. Ranka, G. Fox, and R. V. Shankar, "A Data Parallel Algorithm for Solving the Region Growing Problem on the Connection Machine," *Journal of Parallel and Distributed Computing*, vol. 21, no. 1, April 1994, pp. 160-168.
- [28] I. N. Manousakas, P. E. Undrill, G. G. Cameron, and T. W. Redpath, "Split-and-Merge Segmentation of Magnetic Resonance Medical Images: Performance Evaluation and Extension to Three Dimensions," *Computers and Biomedical Research*, vol. 31, no. 6, December 1998, pp. 393-412.
- [29] D. A. Bader, J. Jájá, D. Hardwood, and L. S. Davis, "Parallel Algorithms for Image Enhancement and Segmentation by Region Growing, with an Experimental Study," *The Journal of Supercomputing*, vol. 10, no. 2, June 1996, pp. 141-168.
- [30] J. K. Udupa, and S. Samarasekera, "Fuzzy Connectedness and Object Definition: Theory, Algorithms, and Applications in Image Segmentation," *Graphical Models and Image Processing*, vol. 58, no. 3, May 1996, pp. 246-261.
- [31] D. Crivianu-Gaita, F. Miclea, A. Gaspar, D. Margineatu, and S. Holban, "3D Reconstruction of Prostate from Ultrasound Images," *International Journal of Medical Informatics*, vol. 45, no. 1, June 1997, pp. 43-51.
- [32] W. Xu, W. Yu, J. Guo, and W. Di, "Handwritten Legal Amounts Segmentation for Cheque Reader Based on Simple Bayesian Classifier," *International Conference on Machine Learning and Cybernetics*, vol. 2, November 2002, pp. 1054-1057.
- [33] F. Ma, W. Wang, W. W. Tsang, Z. Tang, S. Xia, and X. Tong, "Probabilistic Segmentation of Volume Data for Visualization Using SOM-PNN Classifier," *IEEE Symposium on Volume Visualization*, vol. 169, October 1998, pp. 71-78.
- [34] H. Yan "Color Map Image Segmentation Using Optimized Nearest Neighbor Classifiers," *2nd International Conference on Document Analysis and Recognition*, October 1993, pp. 111-114.
- [35] H. Yan, J. Mao, Y. Zhu, and B. Chen, "Magnetic Resonance Image Segmentation Using Optimized Nearest Neighbor Classifiers," *IEEE International Conference on Image Processing (ICIP-94)*, vol. 3, November 1994, pp. 49-52.

- [36] W. E. Blanz and S. L. Gish, "A Connectionist Classifier Architecture Applied to Image Segmentation," *10th International Conference on Pattern Recognition*, vol.2, June 1990, pp. 272-277.
- [37] C. F. Nielsen and P. J. Passmore, "Achieving Accurate Colour Image Segmentation in 2D and 3D with LVQ Classifiers and Partial Adaptable Class-Specific Representation," *5th IEEE Workshop on Applications of Computer Vision*, December 2000, pp. 72-78.
- [38] J. You and H. A. Cohen, "An Orientation and Resolution Independent Texture Classifier in Segmentation of Images of Unknown Rotation and Scale," *11th International Conference on Pattern Recognition, Conference C: Image, Speech and Signal Analysis*, vol. 3, August-September 1992, pp. 49-52.
- [39] C. A. Murthy, N. Chatterjee, B. U. Shankar, and D. D. Majumder, "IRS Image Segmentation: Minimum Distance Classifier Approach," *11th International Conference on Pattern Recognition, Conference A: Computer Vision and Applications*, vol.1, August-September 1992, pp. 781-784.
- [40] B. W. Ng and A. Bouzerdoum, "Supervised Texture Segmentation Using DWT and a Modified K-NN Classifier," *15th International Conference on Pattern Recognition*, vol. 2, September 2000, pp. 545-548.
- [41] M. Kazuhiro and K. Yukio, "Image Segmentation by Neural-Net Classifiers with Genetic Selection of Feature Indices," *International Conference on Image Processing (ICIP 99)*, vol. 1, 1999, pp. 524-528.
- [42] W. Lee, N. Mohankrishnan, and M. J. Paulik, "Improved Segmentation through Dynamic Time Warping for Signature Verification Using a Neural Network Classifier," *International Conference on Image Processing (ICIP 98)*, vol. 2, October 1998, pp. 929-933.
- [43] T. Stathaki, "Segmentation of Textured Surfaces Using Mixed Order Statistics and Neural Network Classifiers," *Electronics Letters*, vol. 31, no. 23, November 1995, pp. 1990-1991.

- [44] A. Pitiot, A. W. Toga, N. Ayache, and P. Thompson, "Texture Based MRI Segmentation with a Two-Stage Hybrid Neural Classifier," *International Joint Conference on Neural Networks (IJCNN '02)*, vol. 3, May 2002, pp. 2053-2058.
- [45] Y. Zhu, Z. Chi, and H. Yan, "Brain Image Segmentation Using Fuzzy Classifiers," *Second Australian and New Zealand Conference on Intelligent Information Systems*, November-December 1994, pp. 244-247.
- [46] M. Singh, P. Patel, D. Khosla, and T. Kim, "Segmentation of Functional MRI by K-Means Clustering," *IEEE Transactions on Nuclear Science*, vol. 43, no. 3, June 1996, pp. 2030-2036.
- [47] M. X. H. Yan and J. S. Karp, "Segmentation of 3D Brain MR Using an Adaptive K-Means Clustering Algorithm," *IEEE Conference on Nuclear Science Symposium and Medical Imaging*, vol. 4, October-November 1994, pp. 1529-1533.
- [48] C. W. Chen, J. Luo, and K. J. Parker, "Image Segmentation via Adaptive K-Mean Clustering and Knowledge-Based Morphological Operations with Biomedical Applications," *IEEE Transactions on Image Processing*, vol. 7, no. 12, December 1998, pp. 1673-1683.
- [49] J. C. Dunn, "A Fuzzy Relative of the ISODATA Process and Its Use in Detecting Compact Well-Separated Clusters", *Journal of Cybernetics*, vol. 3, 1973, pp.32-57.
- [50] J. C. Bezdek, *Pattern Recognition with Fuzzy Objective Function Algorithms*, New York: Plenum Press, 1981.
- [51] Y. X. Qing, H. Z. Hua, and X. Qiang, "Histogram Based Fuzzy C-Mean Algorithm for Image Segmentation," *11th International Conference on Pattern Recognition, Conference C: Image, Speech and Signal Analysis*, vol.3, August-September 1992, pp. 704-707.
- [52] Y. Zhao and M. Li, "A Modified Fuzzy C-Means Algorithm for Segmentation of MRI," *5th International Conference on Computational Intelligence and Multimedia Applications (ICCIMA 2003)*, September 2003, pp. 391-395.

- [53] J. Lin, K. Cheng, and C. Mao, "A Modified Hopfield Neural Network with Fuzzy C-Means Technique for Multispectral MR Image Segmentation," *International Conference on Image Processing*, vol. 1, September 1996, pp. 327-330.
- [54] C. Banga, F. Ghorbel, and W. Pieczynski, "Unsupervised Bayesian Classifier Applied to the Segmentation of Retina Image," *Proceedings of the Annual International Conference of the IEEE Engineering in Medicine and Biology Society*, vol. 5, October-November 1992, pp. 1847-1848.
- [55] N. Grammalidis, L. Bleris, and M. G. Strintzis, "Using the Expectation-Maximization Algorithm for Depth Estimation and Segmentation of Multi-View Images," *1st International Symposium on 3D Data Processing Visualization and Transmission*, June 2002, pp. 686-689.
- [56] Y. Zhang, M. Brady, and S. Smith, "Segmentation of Brain MR Images through a Hidden Markov Random Field Model and the Expectation-Maximization Algorithm," *IEEE Transactions on Medical Imaging*, vol. 20, no. 1, January 2001, pp. 45-57.
- [57] E. Çesmeli and D. Wang, "Texture Segmentation Using Gaussian-Markov Random Fields and Neural Oscillator Networks," *IEEE Transactions on Neural Networks*, vol. 12, no. 2, March 2001, pp. 394-404.
- [58] M. Kass, A. Witkin, and D. Terzopoulos, "Snakes: Active Contour Models," *International Journal of Computer Vision*, vol. 1, 1987, pp. 321-331.
- [59] H. M. Ladak, F. Mao, Y. Wang, D. B. Downey, D. A. Steinman, and A. Fenster, "Prostate Boundary Segmentation from 2D Ultrasound Images," *Medical Physics*, vol. 27, no. 8, August 2000, pp. 1777-1788.
- [60] S. Lobregt and M. A. Viergever, "A Discrete Dynamic Contour Model," *IEEE Transactions on Medical Imaging*, vol. 14, no. 1, March 1995, pp. 12-24.
- [61] T. F. Chan and L. A. Vese, "Active Contours without Edges," *IEEE Transactions on Image Processing*, vol. 10, no.2, February 2001, pp. 266-277.

- [62] C. Xu and J. L. Prince, "Snakes, Shapes, and Gradient Vector Flow," *IEEE Transactions on Image Processing*, vol. 7, no. 3, March 1998, pp. 359-369.
- [63] Y. Hu, W. J. Rogers, D. A. Coast, C. M. Kramer, and N. Reichek, "Vessel Boundary Extraction Based on a Global and Local Deformable Physical Model with Variable Stiffness," *Magnetic Resonance Imaging*, vol. 16, no.8, October 1998, pp. 943-951.
- [64] M. Kisworo, S. Venkatesh, and G. A. W. West, "Detection of Curved Edges at Subpixel Accuracy Using Deformable Models," *IEE Proceedings of Vision, Image and Signal Processing*, vol. 142, no. 5, October 1995, pp. 304-312.
- [65] F. H. Y. Chan, F. K. Lam, P. W. F. Poon, H. Zhu, and K. H. Chan, "Object Boundary Location by Region and Contour Deformation," *IEE Proceedings of Vision, Image and Signal Processing*, vol. 143, no. 6, December 1996, pp. 353-360.
- [66] P. Brigger, J. Hoeg, and M. Unser, "B-Spline Snakes: A Flexible Tool for Parametric Contour Detection," *IEEE Transactions on Image Processing*, vol. 9, no. 9, September 2000, pp. 1484-1496.
- [67] M. A. T. Figueiredo, J. M. N. Letão, and A. K. Jain, "Unsupervised Contour Representation and Estimation Using B-Splines and a Minimum Description Length Criterion," *IEEE Transactions on Image Processing*, vol. 9, no. 6, June 2000, pp. 1075-1087.
- [68] K. Siddiqi, Y. B. Lauzière, A. Tannenbaum, and S. W. Zucker, "Area and Length Minimizing Flows for Shape Segmentation," *IEEE Transactions on Image Processing*, vol. 7, no. 3, March 1998, pp. 433-443.
- [69] A. Tsai, J. A. Yezzi, and A. S. Willsky, "Curve Evolution Implementation of the Mumford-Shah Functional for Image Segmentation, Denoising, Interpolation, and Magnification," *IEEE Transactions on Image Processing*, vol. 10, no. 8, August 2001, pp. 1169-1186.
- [70] M. Wang, J. Evans, L. Hassebrook, and C. Knapp, "A Multistage, Optimal Active Contour Model," *IEEE Transactions on Image Processing*, vol. 5, no. 11, November 1996, pp. 1586-1591.

- [71] G. I. Chiou and J. Hwang, "A Neural Network-Based Stochastic Active Contour Model (NNS-SNAKE) for Contour Finding of Distinct Features," *IEEE Transactions on Image Processing*, vol. 4, no. 10, October 1995, pp. 1407-1416.
- [72] F. Höwing, L. S. Dooley, and D. Wermser, "Fuzzy Active Contour Model," *IEE Proceedings of Vision, Image and Signal Processing*, vol. 147, no. 4, August 2000, pp. 323-330.
- [73] C. Knoll, M. Alcañiz, V. Grau, C. Monserrat, and M. C. Juan, "Outlining of the Prostate Using Snakes with Shape Restrictions Based on the Wavelet Transform," *Pattern Recognition*, vol. 32, no. 10, October 1999, pp. 1767-1781.
- [74] H. Wu, J. Liu, and C. Chui, "A wavelet-Frame Based Image Force Model for Active Contouring Algorithms," *IEEE Transaction on Image Processing*, vol. 9, no. 11, November 2000, pp. 1983-1988.
- [75] Y. Fu, A. T. Erdem, and A. M. Tekalp, "Tracking Visible Boundary of Objects Using Occlusion Adaptive Motion Snake," *IEEE Transactions on Image Processing*, vol. 9, no. 12, December 2000, pp. 2051-2060.
- [76] U. Montanari, "On the Optimal Detection of Curves in Noisy Pictures," *Communications of the ACM*, vol.14, no.5, May 1971, pp. 335-345.
- [77] A. Martelli, "An Application of Heuristic Search Methods to Edge and Contour Detection," *Communications of the ACM*, vol.19, no.2, February 1976, pp. 73-83.
- [78] D. B. Cooper, "Maximum Likelihood Estimation of Markov-Process Blob Boundaries in Noisy Images," *IEEE Transactions Pattern Analysis and Machine Intelligence*, vol. PAMI-1, no. 4, October 1979, pp. 372-384.
- [79] D. B. Cooper, H. Elliott, F. Cohen, L. Reiss, and P. Symosek, *Stochastic Boundary Estimation and Object Recognition*, Image Modeling, A. Rosenfeld, Ed. New York: Academic Press, 1981, pp. 63-94.

- [80] C. W. K. Gritton and E. A. Parrish, "Boundary Location from an Initial Plan: The Bead Chain Algorithm," *IEEE Transactions on Pattern Analysis and Machine Intelligence*, vol. 5, no. 1, January 1983, pp. 8-13.
- [81] G. Stovik, "A Bayesian Approach to Dynamic Contours through Stochastic Sampling and Simulated Annealing," *IEEE Transactions on Pattern Analysis and Machine Intelligence*, vol. 16, no. 10, October 1994, pp.976-986.
- [82] A. A. Amini, T.E. Weymouth, and A. K. Jain, "Using Dynamic Programming for Solving Variational Problems in Vision," *IEEE Transactions on Pattern Analysis and Machine Intelligence*, vol. 12, no. 9, September 1990, pp. 855-867.
- [83] L. H. Staib and J. S. Duncan, "Boundary Finding with Parametrically Deformable Models," *IEEE Transactions on Pattern Analysis and Machine Intelligence*, vol. 14, no. 11, November 1992, pp. 1061-1075.
- [84] L. D. Cohen, "On Active Contour Models and Balloons," *Computer Vision, Graphics and Image Processing: Image Understanding*, vol. 53, no. 2, March 1991, pp. 211-218.
- [85] L. D. Cohen and I. Cohen, "Finite-Element Methods for Active Contour Models and Balloons for 2-D and 3-D Images," *IEEE Transactions on Pattern Analysis and Machine Intelligence*, vol. 15, no. 11, November 1993, pp. 1131-1147.
- [86] F. Leymarie and M.D. Levine, "Tracking Deformable Objects in the Plane Using an Active Contour Mode," *IEEE Transactions on Pattern Analysis and Machine Intelligence*, vol. 15, no. 6, June 1993, pp. 617-634.
- [87] D. J. Williams and M. Shah, "A Fast Algorithm for Active Contours and Curvature Estimation," *Computer Vision, Graphics and Image Processing: Image Understanding*, vol. 55, no. 1, January 1992, pp. 14-26.
- [88] F. O'Sullivan and M. Qian, "A Regularized Contrast Statistical for Object Boundary Estimation – Implementation and Statistical Evaluation," *IEEE Transactions on Pattern Analysis and Machine Intelligence*, vol. 16, no. 6, June 1994, pp. 561-570.

- [89] R. Ronfard, "Region-Based Strategies for Active Contour Models," *International Journal of Computer Vision*, vol. 13, no. 2, October 1994, pp. 229-251.
- [90] J. Ivins and J. Porrill, "Active Region Models for Segmenting Medical Images," *Proceedings of the IEEE International Conference on Image Processing*, vol. 2, November 1994, pp. 227-231.
- [91] J. Ivins and J. Porrill, "A Semiautomatic Tool for 3D Medical Image Analysis Using Active Contour Models," *Medical Informatics*, vol. 19, no. 1, January-March 1994, pp. 81-90.
- [92] T. Pavlidis and Y. T. Liow, "Integrating Region Growing and Edge Detection," *IEEE Transactions on Pattern Analysis and Machine Intelligence*, vol. 12, no. 3, March 1990, pp. 225-233.
- [93] J. M. Gauch, H. H. Pien, and J. Shah, "Hybrid Boundary-Based and Region-Based Deformable Models for Biomedical Image Segmentation," *Proceedings of SPIE Mathematical Methods in Medical Imaging III*, vol. 2299, July 1994, pp. 72-83.
- [94] I. L. Herlin, C. Nguyen, and C. Graffigne, "A Deformable Region Model Using Stochastic Processes Applied to Echocardiographic Images," *Proceedings of IEEE Conference on Computing Vision and Pattern Recognition*, June 1992, pp. 534-537.
- [95] I. L. Herlin, C. Nguyen, and C. Graffigne, "Stochastic Segmentation of Ultrasound Images," *11th IEEE International Conference on Pattern Recognition*, vol.1, August-September 1992, pp. 289-292.
- [96] C. Xu, "Deformable Models with Application to Human Cerebral Cortex Reconstruction from Magnetic Resonance Image," doctoral dissertation, Department of Electrical and Computer Engineering, Johns Hopkins University, USA, January 1999.
- [97] E.D. Angelini, Y. Jin, and A.F. Laine, *State-of-the-Art of Level Set Methods in Segmentation and Registration of Medical Imaging Modalities*, Handbook of Medical Image Analysis: Advanced Segmentation and Registration Models, Jasjit Suri, David

- L. Wilson and Swamy Laximinarayan, Ed. New York: Kluwer Academic Publishers, 2004.
- [98] J. A. Sethian, "Level Set Methods: An Act of Violence," *American Scientist*, vol. 85, no. 3, May-June 1997, pp. 1-23.
- [99] S. Osher and J. A. Sethian, "Fronts Propagating with Curvature-Dependent Speed: Algorithms Based on Hamilton-Jacobi Formulations," *Journal of Computational Physics*, vol. 79, no. 1, November 1988, pp. 12-49.
- [100] J.A. Sethian, *Level Set Methods and Fast Marching Methods: Evolving Interfaces in Computational Geometry, Fluid Mechanics, Computer Vision and Materials Science*. Cambridge University Press, 1999.
- [101] R. Malladi, and J. A. Sethian, *A Unified Approach for Shape Segmentation, Representation, and Recognition*, technical report 14, Center for Pure and Applied Mathematics, Berkeley, University of California, 1994.
- [102] R. Malladi, and J. A. Sethian, "Level Set Methods for Curvature Flow, Image Enhancement, and Shape Recovery in Medical Images," *Proceedings of Conference on Visualization and Mathematics: Experiments, Simulations and Environments*, 1997, pp. 329-345.
- [103] R. Malladi, J. A. Sethian, and B. C. Vemuri, "A Fast Level Set Based Algorithm for Topology-Independent Shape Modeling," *Journal of Mathematical Imaging and Vision*, vol. 6, no. 2, June 1996, pp. 269-289.
- [104] R. Malladi, J. A. Sethian, and B. C. Vemuri, "Shape Modeling with Front Propagation: A Level Set Approach," *IEEE Transactions on Pattern Analysis and Machine Intelligence*, vol. 17, no. 2, February 1995, pp. 158-175.
- [105] R. Malladi and J. A. Sethian, "Image Processing via Level Set Curvature Flow," *Proceedings of the National Academy of Sciences*, vol. 92, no. 15, July 1995, pp. 7046-7050.

- [106] R. Malladi and J. A. Sethian, "Image Processing: Flows Under Min/Max Curvature and Mean Curvature," *Graphical Models and Image Processing*, vol. 58, no. 2, March 1996, pp. 127-141.
- [107] R. Kimmel and J. A. Sethian, *Fast Marching Methods for Robotic Navigation with Constraints*, technical report, Center for Pure and Applied Mathematics, Berkeley, Berkeley, University of California, May 1996.
- [108] D. Adalsteinsson and J. A. Sethian, "A Level Set Approach to a Unified Model for Etching, Deposition, and Lithography, I: Two-Dimensional Simulations," *Journal Computational Physics*, vol. 120, no. 1, August 1995, pp. 128-144.
- [109] D. Adalsteinsson and J. A. Sethian, "A Level Set Approach to a Unified Model for Etching, Deposition, and Lithography, II: Three-Dimensional Simulations," *Journal Computational Physics*, vol. 122, no. 2, December 1995, pp. 348-366.
- [110] D. Adalsteinsson and J. A. Sethian, "A Level Set Approach to a Unified Model for Etching, Deposition, and Lithography, III: Re-Deposition, Re-Emission, Surface Diffusion, and Complex Simulations," *Journal Computational Physics*, vol. 138, no. 1, November 1997, pp. 193-223.
- [111] J. A. Sethian and A. Wiegmann, "Structural Boundary Design via Level Set and Immersed Interface Methods," *Journal Computational Physics*, vol. 163, no. 2, September 2000, pp. 489-528.
- [112] J. A. Sethian, "A Review of Recent Numerical Algorithms for Hypersurfaces Moving with Curvature-Dependent Speed," *Journal of Differential Geometry*, vol. 31, 1989, pp. 131-161.
- [113] V. Caselles, F. Catté, T. Coll, and F. Dibos, "A Geometric Model For Active Contours in Image Processing," *Numerische Mathematik*, vol. 66, no. 1, October 1993, pp. 1-31.
- [114] R. Malladi, J. A. Sethian, and B. C. Vemuri, "A Topology Independent Shape Modeling Scheme," *Proceedings of SPIE Conference on Geometric Methods in Computer Vision II*, vol. 2031, July 1993, pp. 246-258.

- [115] J. Awad, T. K. Abdel-Galil, M. M. A. Salama, A. Fenster, K. Rizkalla, D. B. Downey, and H. Tizhoosh, "Prostate's Boundary Detection in Transrectal Ultrasound Images Using Scanning Technique," *IEEE Canadian Conference on Electrical and Computer Engineering*, vol. 2, May 2003, pp. 1199-1202.
- [116] J. Ton, J. Sticklen, and A. K. Jain, "Knowledge-Based Segmentation of Landsat Images," *IEEE Transactions on Geoscience and Remote Sensing*, vol. 29, no. 2, March 1991, pp. 222-232.
- [117] Z. Zhang and M. Simaan, "A Knowledge-Based System Controlled by an Iterative Quadtree Splitting Scheme for Segmentation of Seismic Sections," *IEEE Transactions on Geoscience and Remote Sensing*, vol. 26, no. 5, September 1988, pp. 518-524.
- [118] N. Hu, D.B. Downey, A. Fenster, and H.M. Ladak, "Prostate Surface Segmentation from 3D Ultrasound Images," *Proceedings of IEEE International Symposium on Biomedical Imaging*, July 2002, pp. 613-616.
- [119] N. Hu, D.B. Downey, A. Fenster, and H.M. Ladak, "Prostate Boundary Segmentation from 3D Ultrasound Images," *Medical Physics*, vol. 30, no. 7, July 2003, pp.1648-1659.
- [120] A. Ghanei, H. Soltanian-Zadeh, A. Ratkesicz, and F. Yin, "A Three-Dimensional Deformable Model for Segmentation of Human Prostate from Ultrasound Image," *Medical Physics*, vol. 28, no. 10, October 2001, pp. 2147-2153.
- [121] Y. Wang, H. N. Cardinal, D. B. Downey, and A. Fenster, "Semiautomatic Three-Dimensional Segmentation of the Prostate Using Two Dimensional Ultrasound Images," *Medical Physics*, vol. 30, no.5, May 2003, pp. 887-897.
- [122] H.M. Ladak, F. Mao, Y. Wang, D.B. Downey, D.A. Steinman, and A. Fenster, "Prostate Segmentation from 2D Ultrasound Images," *Medical Physics*, vol. 27, no. 8, August 2000, pp. 1777-1788.

- [123] B. C. Y. Chiu, G. H. Freeman and M. M. A. Salama, A. Fenster, K. Rizkalla, and D. B. Downey, "A Segmentation Algorithm Using Dyadic Wavelet Transform and Discrete Dynamic Contour," *Proceedings of CCECE 2003*, May 2003, pp. 1481-1484.
- [124] B. Chiu, G. H. Freeman, M. M. A. Salama, and A. Fenster, "Prostate Segmentation Algorithm Using Dyadic Wavelet Transform and Discrete Dynamic Contour," *Physics in Medicine and Biology*, vol. 49, no. 21, November 2004, pp. 4943-4960.
- [125] A Jendoubi, J. Zeng, and M. F. Chouikha, "Top-Down Approach to Segmentation of Prostate Boundaries in Ultrasound Images," *33rd Applied Imagery Pattern Recognition Workshop (AIPR'04)*, April 2004, pp. 145-149.
- [126] L. Gong, S. D. Pathak, D. R. Haynor, P. S. Cho, and Y. Kim, "Parametric Shape Modeling Using Deformable Superellipses for Prostate Segmentation," *IEEE Transactions on Medical Imaging*, vol. 23, no. 3, March 2004, pp. 340-349.
- [127] S. D. Pathak, V. Chalana, D. R. Haynor, Y. Kim, "Edge-Guided Boundary Delineation in Prostate Ultrasound Images," *IEEE Transactions on Medical Imaging*, vol. 19, no. 12, December 2000, pp. 1211-1219.
- [128] R. Abolmaesumi and M.R. Sirouspour, "Segmentation of Prostate Contours from Ultrasound Images," *IEEE International Conference on Acoustics, Speech, and Signal Processing*, vol. 3, May 2004, pp. 517-520.
- [129] F. Sahba, H. R Tizhoosh, and M. M Salama, "A Coarse-to-Fine Approach to Prostate Boundary Segmentation in Ultrasound Images," *BioMedical Engineering OnLine*, vol. 4, no. 1, October 2005, pp. 58-70.
- [130] D. Shen, Y. Zhan and C. Davatzikos, "Segmentation of Prostate Boundaries from Ultrasound Images Using Statistical Shape Model," *IEEE Transactions on Medical Imaging*, vol. 22, no. 4, April 2003, pp. 539-551.
- [131] N. Betrouni, M. Vermandel, J. Rousseau, and S. Mouche, "Automatic Segmentation of Prostate Boundaries from Abdominal Ultrasound Images Using Prior Knowledge," *Proceedings of the IEEE International Symposium on Biomedical Imaging*, April 2004, pp. 496-499.

- [132] N. Betrouni, M. Vermandel, D. Pasquier, S. Maouche, and J. Roussea, "Segmentation of Abdominal Ultrasound Images of the Prostate Using Prior Information and an Adapted Noise Filter," *Computerized Medical Imaging and Graphics*, vol. 29, no.1, January 2005, pp. 43-51.
- [133] K. D. Nanayakkara and J. Samarabandu, "Unsupervised Model Based Image Segmentation Using Domain Knowledge Based Fuzzy Logic and Edge Enhancement," *IEEE International Conference on Multimedia and Expo (ICME)*, July 2003, pp. 577-580.
- [134] W. D. Richard and C. G. Keen, "Automated Texture-Based Segmentation of Ultrasound Images of the Prostate," *Computerized Medical Imaging and Graphics*, vol. 20, no. 3, May-June 1996, pp. 131-140.
- [135] B. Chiu, "A New Segmentation Algorithm for Prostate Boundary Detection in 2D Ultrasound Images," master's thesis, Department of Electrical and Computer Engineering, University of Waterloo, Waterloo, Ontario, Canada, 2003.
- [136] R. N. Czerwinski, D. L. Jones, and W. D. O'Brien, "Line and Boundary Detection in Speckle Images," *IEEE Transactions on Image Processing*, vol. 7, no. 12, December 1998, pp. 1700-1713.
- [137] R. N. Czerwinski, D. L. Jones, and W. D. O'Brien, "Detection of Lines and Boundaries in Speckle Images – Application to Medical Ultrasound," *IEEE Transactions on Medical Imaging*, vol. 18, no. 2, February 1999, pp. 126-136.
- [138] R. T. Hurlburt, *Comprehending Behavioral Statistics*, Pacific Grove, California: Brooks/Cole Publishing Company, 1994.
- [139] P. F. Felzenszwalb and D. P. Huttenlocher, "Image Segmentation Using Local Variation," *Proceedings of IEEE Conference on Computer Vision and Pattern Recognition*, June 1998, pp 98-104.
- [140] E. K. T. Hui, "Region-Based Feature Extraction of Prostate Ultrasound Images: A Knowledge-Based Approach Using Fuzzy Inference," master's thesis, Department of

Electrical and Computer Engineering, University of Waterloo, Waterloo, Ontario, Canada, 2003.

- [141] S. Mohamed, T. K. Abdel-galil, M. M. A. Salama, A. Fenster, , K. Rizkalla and D. B. Downey "Prostate Cancer Diagnosis Based on Gabor Filter Texture Segmentation of Ultrasound Image," *IEEE Canadian Conference on Electrical and Computer Engineering*, vol. 3, May 2003, pp. 1485-1488.
- [142] S.S. Mohamed, M.M.A. Salama, M. Kamel, and K. Rizkalla, "Region of Interest Based Prostate Tissue Characterization Using Least Square Support Vector Machine LS-VSM", *Lecture Notes in Computer Science*, vol. 3212, September 2004, pp. 51-58.
- [143] B. PotoEnik and D. Zazula, "Automated Ovarian Follicle Segmentation Using Region Growing," *The First International Workshop on Image and Signal Processing and Analysis*, June 2000, pp.157-162.
- [144] M. Fukushima, K. Ogawa, T. Kubota, and N. Hisa, "Quantitative Tissue Characterization of Diffuse Liver Diseases from Ultrasound Images by Neural Network," *IEEE Nuclear Science Symposium*, vol. 2, November 1997, pp.1233-1236.
- [145] N. M. Zayed, A. M. Badwi, A. Elsayad, M. S. Elsherif, and A.-B. M. Youssef, "Wavelet Segmentation for Fetal Ultrasound Images," *44th IEEE Circuits and Systems*, vol. 1, August 2001, pp.501-504.
- [146] M. H. Repacholi, *Ultrasound Characteristics and Biological Action*, National Research Council of Canada, MRC Associate Committee on Scientific Criteria for Environmental Quality, 1981.
- [147] J. McCaffrey, "Role of Ultrasound in Surgery: Introduction," *World Journal of Surgery*, vol. 24, no. 2, February 2000, p. 133.
- [148] P. N. T. Wells, *Biomedical Ultrasonics*, New York: Academic Press, 1977.
- [149] J. Enderle, S. Blanchard, and J. Bronzino, *Introduction to Biomedical Engineering*, London: Academic Press, 2000.

- [150] J. H. V. Bommel and M. A. Musen, *Handbook of Medical Informatics*, Germany: Springer Verlag, 1997.